

**DYNAMIC RESOURCE ALLOCATION FOR HIGH SPECTRAL
AND ENERGY EFFICIENCY IN CLOUD RADIO ACCESS
NETWORKS**

by

ABOLFAZL HAJISAMI

A dissertation submitted to the

School of Graduate Studies

Rutgers, The State University of New Jersey

in partial fulfillment of the requirements

for the degree of

Doctor of Philosophy

Graduate Program in Electrical and Computer Engineering

Written under the direction of

Dario Pompili

and approved by

New Brunswick, New Jersey

May, 2018

ABSTRACT OF THE DISSERTATION

Dynamic Resource Allocation for High Spectral and Energy Efficiency in Cloud Radio Access Networks

By ABOLFAZL HAJISAMI

Dissertation Director:

Dario Pompili

Over the last few years, the proliferation of personal mobile computing devices like tablets and smartphones along with a plethora of data-intensive mobile applications has resulted in a tremendous increase in demand for ubiquitous and high data rate wireless communications. However, the system capacity is limited by the radio interference, which makes it difficult to improve the spectral efficiency and consequently the data rate. Current practice to enhance spectral efficiency and data rate is to increase the number of Base Stations (BSs) and go for smaller cells so as to increase the band reuse factor. However, performing additional deployment and maintenance of a large number of cellular BSs is highly inefficient due to excessive capital and operational expenditures. Moreover, with smaller cells the interference problem becomes even more challenging. It is also studied that increasing the BS density or the number of transmit antennas will decrease the energy efficiency due to the dynamic traffic variation. This is because the current cellular architecture is over 40 years old and was not originally designed for high spectral and energy efficiency performance but for coverage and mobility considerations.

Cloud Radio Access Network (C-RAN) is a new paradigmatic architecture for wireless cellular networks that allows for dynamic reconfiguration of computing and spectrum resources while keeping the cost of delivering services to the users low. C-RAN consists of three main parts: 1) Remote Radio Heads (RRHs) plus antennae, which are located at the remote site and are controlled by Virtual Base Stations (VBSs) housed in a centralized processing pool, 2) the Base Band Unit (BBU)

(known as VBS pool) composed of high-speed programmable processors and real-time virtualization technology to carry out the digital processing tasks, and 3) low-latency high-bandwidth optical fibers, which connect the RRHs to the VBS pool. In a centralized VBS pool, since all the information from the BSs resides in a common place, the VBSs can exchange control data at Gbps. This centralized characteristic along with virtualization technology and low-cost relay-like RRHs provides a higher degree of freedom in order to make optimized decisions; all these features combined have made C-RAN a promising technology candidate to be incorporated into the 5G wireless network standard.

The overarching goal of the research presented in this thesis is to design new techniques for increasing the spectral and energy efficiency of the next generation wireless cellular networks. In order to increase the spectral efficiency and energy efficiency, we leverage the C-RAN architecture and propose four solutions, namely 1) Cloud-BSS, 2) DJP, 3) Cloud-CFFR, and 4) Elastic-Net. In Cloud-BSS, we study the performance of Blind Source Separation (BSS) in order to separate the interference from the desired signal and explore how the performance changes in different topologies. Since Cloud-BSS does not take any action to mitigate the inter-cluster interference, we propose DJP to decrease both the intra- and inter-cluster interference. Moreover, in order to improve the performance of Fractional Frequency Reuse (FFR), we propose Cloud-CFFR, which is able to reject the intra-cluster interference and decrease the inter-cluster interference. Finally, in order to increase the energy efficiency, we propose Elastic-Net, where the network parameters are optimized and adapted based on the traffic fluctuation so that the power consumption is minimized while the resource utilization is maximized.

Acknowledgements

I would like to express my deepest thanks to my advisor, Dr. Dario Pompili, who expertly guided me through my PhD journey. I am extremely indebted to him for his faith in my abilities. His continuous encouragement, creative advice, and approachability kept me constantly engaged with my research. During our many discussions, besides guiding me in my research, he also advised me on discipline and how to do quality work, and also provided detailed feedback on my work.

I would also like to thank CPS Lab members, Hariharasudhan Viswanathan, Eun Kyung Lee, Parul Pandey, Mehdi Rahmati, Parsa Hosseini, Vidyasagar Sadhu, Harry Tran, Xueyuan Zhao, and Ayman Younis with whom I have brainstormed on several different occasions, which has helped me immensely.

I would like to extend my gratitude to Drs. Zoran Gajic, Sophocles Orfanidis, Ali Masoomzadeh, Mohammad Ali Maddah-Ali, and Emina Soljanin for accepting to be the committee members in my proposal and dissertation defense.

Last, but not least, I would like to thank my family for all the support and encouragement throughout these years of study.

Dedication

To

My Parents

Table of Contents

Abstract	ii
Acknowledgements	iv
Dedication	v
List of Tables	ix
List of Figures	x
1. Introduction	1
1.1. Distributed Radio Access Network (D-RAN)	1
1.1.1. Shortcomings of D-RAN	1
1.2. Cloud Radio Access Network (C-RAN)	3
1.2.1. Advantages of C-RAN	5
1.3. Contribution	6
1.3.1. Blind Source Separation for Cooperative Cellular Communication in C-RAN	6
1.3.2. Dynamic Joint Processing for Interference Cancellation in C-RAN	7
1.3.3. Coordinated Fractional Frequency Reuse in C-RAN	7
1.3.4. Demand-Aware Resource Allocation for High Energy Efficiency and Resource Utilization in C-RAN	8
1.4. Dissertation Organization	8
2. Background and Related Works	10
2.1. Software Defined Virtual Base Station Pool	10
2.2. Technical Challenges of C-RAN Deployment	11
2.3. Research Challenges of Future Wireless Cellular Network	11
2.4. State of the Art in C-RAN	12

3. Blind Source Separation for Cooperative Cellular Communication in C-RAN	17
3.1. Overview	17
3.2. Blind Source Separation (BSS)	19
3.3. Blind Source Separation for Cooperative Communication in Cloud (Cloud-BSS) . .	19
3.3.1. System Performance for Different Topologies	21
3.3.2. Proposed Strategy for Operation under Non Idealities	23
3.3.3. Cluster Size and Computational Complexity	25
3.4. Other Benefits of our Proposed Cloud-BSS	27
3.4.1. Fewer Handovers	28
3.4.2. Increased Reliability	30
3.4.3. Interference Cancellation	31
3.4.4. No Additional Overhead Compared to CoMP	33
3.5. Discussion	33
4. Dynamic Joint Processing for Interference Cancellation in C-RAN	34
4.1. Overview	34
4.2. System Model and Challenges	36
4.2.1. System Description	36
4.2.2. Problem Statement	38
4.2.3. Case Study	38
4.3. Proposed Solution	41
4.3.1. Virtual Base Station Cluster	42
4.3.2. Low-mobility Approach (DJP-LM)	43
4.3.3. High-mobility Approach (DJP-HM)	46
4.3.4. Dynamic Joint Processing (Joint DJP-LM and DJP-HM)	48
4.4. Performance Evaluation	50
4.4.1. Propagation Model	52
4.4.2. Simulation Results	52
4.5. Discussion	60

5. Coordinated Fractional Frequency Reuse in C-RAN	62
5.1. Overview	62
5.2. Challenges of Fractional Frequency Reuse	63
5.3. Coordinated Fractional Frequency Reuse in the Cloud (Cloud-CFFR)	65
5.4. Performance Evaluation	71
5.4.1. Setting	71
5.4.2. Simulation Results	74
5.5. Discussion	79
6. Demand-Aware Resource Allocation for High Energy Efficiency and Resource Utilization in C-RAN	81
6.1. Overview	81
6.2. System Model	82
6.2.1. RRH and Transport Network Power Consumption Model	83
6.2.2. VBS Pool Power Consumption Model	85
6.2.3. Clustering the VBSs and RRHs	85
6.3. Elastic-Net: Demand-Aware Provisioning	86
6.4. Optimal Active RRH Density and Transmission Power	89
6.5. Computational Characteristics of a Virtual Base Station and Optimal VM Size	91
6.5.1. Emulation Platform and Testbed Architecture	91
6.5.2. Monitoring the OAI eNB and the UE	93
6.5.3. Processing Time of LTE Subframes	94
6.5.4. CPU Utilization	94
6.5.5. Optimal Size of VM	96
6.6. Performance Evaluation	98
6.6.1. Simulation Results	98
6.6.2. Impact of Traffic Variation in Power Consumption	101
6.6.3. Testbed Experiment Results	105
6.7. Discussion	106

7. Conclusions and Future Research Directions	107
References	109

List of Tables

3.1. Computational Complexity, Run Time (RT), and Performance Index (PI) of three competing ICA methods for five parameters: N = no. of sources, M = no. of mixtures, T = no. of data samples, Q = no. of iterations, and I = no. of executed sweep; in the simulations, we considered $N = M = 5$	27
3.2. Reduction of handovers by clustering the cells using our BSS-based solution; cell radius = 1 km, simulation area = 30×30 km ² , $s_{min} = 0$, $s_{max} = 30$ m/s, simulation time = 1 hr, no. of MSs = 1000, $\bar{d} = \pi$, $\bar{s} = 15$ m/s, $d_{x_{n-1}} \sim \mathcal{N}(\pi, 1)$, $s_{x_{n-1}} \sim \mathcal{N}(15, 3)$, no. of simulations = 100.	28
3.3. Comparison of uplink Spectral Efficiency (SE) and Throughput (R) between non-cooperative traditional systems and <i>Cloud-BSS</i> (cell radius = 1 km).	32
4.1. Simulation Parameters.	50
4.2. Re-clustering procedures per subcarrier per cell for different cell radii, velocities, and methods.	58
5.1. Simulation parameters.	72
6.1. Testbed Configuration Parameters	93
6.2. Values of parameters α_{PRB} and β_{MCS}	94
6.3. Simulation Parameters.	98
6.4. Power usage, CPU utilization, and resource utilization for static (D-RAN) and dynamic provisioning (C-RAN).	106

List of Figures

1.1.	Power consumption of (a) the Radio Access Network (RAN) and (b) the Base Stations (BSs).	2
1.2.	Distributed Cloud Radio Access Network (D-RAN) vs. two Cloud Radio Access Network (C-RAN). (a) D-RAN architecture; (b) Partially-centralized architecture: only MAC processing is centralized in Virtual Base Station (VBS) pool; (c) Fully-centralized architecture: VBS pool takes care of PHY and MAC processing.	4
3.1.	Four network topologies in which the RRHs receive different combinations ('mixtures') of the MS signals. From Topology 1 to 4 (worst to best), the distance between a MS in a cell and the RRHs in the other cells becomes higher.	18
3.2.	Increase in Bit Error Rate (BER) with increase in non-diagonal dominance of mixing matrix \mathbf{A} (the closer $D(\mathbf{A})$ to 1, the more \mathbf{A} is non-diagonal dominant); note that in this simulation we considered $N = M$	22
3.3.	Decrease in BER with Signal-to-Noise Ratio (SNR) and topology order for each of the four different topologies considered in Fig. 3.1.	23
3.4.	Example for allocating frequency channels to the MS's.	24
3.5.	<i>Channel-Select</i> vs. optimal solution (by exhaustive search) for small problem sizes (cluster size $M = 3$).	25
3.6.	Increase in Run Time (RT) and Performance Index (PI) of the three ICA algorithms with increase in the no. of sources and mixtures (here $T=8000$). The left y-axis reports the RT in seconds, while the right y-axis reports the PI as in (3.6).	28
3.7.	Four cases of mobile network in which all the MS's are using the same frequency channel.	30
3.8.	Increase of BER by moving the MS's towards a common cell.	31

3.9. Increase in the Net Channel Capacity with increase in N , with $M = 7$, for different $SNR = 5, 10, 15, 20$ dB and $D(\mathbf{A}) = 0.3$	31
3.10. Trading off capacity for improved BER: decrease of BER with SNR when removing MS # 2 or MS # 3 from Fig. 3.1(b).	32
4.1. Data exchange within a cluster in Coordinated Multi-Point (CoMP) transmission and reception.	35
4.2. Intra- and inter-cluster uplink interference (we name the MS (BS) inside the cluster as <i>internal</i> and outside the cluster as <i>external</i> MS (BS)).	35
4.3. Case study to show the issues with traditional CoMP: (a) Network of 4 cells where each cell has 2 MSs to serve; (b) and (c) Horizontal and vertical omni-subband clustering for the first scenario of spectrum allocation; (d) and (e) Horizontal and vertical omni-subband clustering for the second scenario of spectrum allocation; (f) Uni-subband clustering for the second scenario of spectrum allocation; (g) Virtual uni-subband clusters for subband #1; (h) Virtual uni-subband clusters for subband #2.	39
4.4. Virtual Base Station Cluster (VBS-Cluster): VBSs associated with a cluster are merged together in the VBS-Cluster and RRHs antennae in each cluster act as a single coherent antenna array distributed over the cluster region.	42
4.5. Message exchanges among a MS, serving VBS, and virtual clusters during re-clustering.	46
4.6. (a) Each cell consists of three sectors (S1, S2, and S3) and neighboring sectors from different cells form hybrid cells; (b) Each VBS consists of 3 Sector-VBSs each of which serves the corresponding sector in the cell (each VBS-Cluster is formed of 3 Sector-VBSs from different neighboring cells); (c) To avoid inter-cluster interference we use different portion of frequency band in different hybrid cells; we also change the boundaries of frequency sub-bands to address the unanticipated fluctuations in the number of users and per-user capacity demands.	48
4.7. Soft-FFR deployment with a cell-edge reuse factor of 1/3.	51
4.8. Equally-sized hexagonal cell structure with two tiers of interfering cells, where R is the Cell Radius, $D = \sqrt{3}R$ the Inter-site Distance, and $A = \frac{3\sqrt{3}}{2}R^2$ the Cell Area.	51

4.9. Signal-to-Interference-plus-Noise Ratio (SINR) for different Normalized Distances.	53
4.10. Spectral Efficiency (SE) in terms of Normalized Distance.	53
4.11. Outage probability for different thresholds.	54
4.12. Cumulative Distribution Function (CDF) as a function of SINR.	55
4.13. Average Throughput for different path loss exponents.	56
4.14. Average System Spectral Efficiency (ASSE) as a function of SNR.	56
4.15. BER for different Normalized Distances.	57
4.16. Comparison of Average BER in terms of channel uncertainty.	58
4.17. Performance of Energy Efficiency (EE) of different methods in different environ- ments vs. varying path loss exponents.	59
4.18. Comparison of Blocking Probability between traditional cellular system and DJP- HM for different number of MSs.	60
5.1. (a) Strict-FFR and (b) Soft-FFR deployments with cell-edge reuse factor of 1/3.	63
5.2. The Interference Region (IR) associated with cell #3 (gray region) includes the cell itself as well as the neighboring Cell-Edge Regions (CERs).	65
5.3. Intersections of serving cell's Interference Region (IR) with its neighboring cells' IRs.	66
5.4. The average distance between the MSs using the same subcarrier and located in the different clusters are 3 times of cell radius.	69
5.5. Equally sized hexagonal cell structures where r is the cell radius, $D = \sqrt{3}r$ is the inter-site distance, R_i is the IR radius, and $A = \frac{3\sqrt{3}}{2}r^2$ is the cell area.	73
5.6. SINR for different Normalized Distances (d/r).	75
5.7. Average Throughput for different Pass Loss Exponent λ	76
5.8. Outage Probability for different thresholds in dB.	76
5.9. CDF as a function of SINR.	77
5.10. BER for different Normalized Distances.	77
5.11. Comparison of Average BER in terms of channel uncertainty.	78
5.12. Performance of Energy Efficiency (EE) of different methods in different environ- ments (different path loss exponents).	78
5.13. Comparison of Blocking Probability for different number of MSs.	79

6.1. The use of virtualization in C-RAN allows dynamic re-provisioning of spectrum and computing resources (visualized here using different sizes) to the VBSs based on demand fluctuation; (a) and (b) illustrate the movement of mobile network load from the downtown office area to the residential and recreational areas over the course of a day and the corresponding changes in active RRH density and VBS size (we have used different icons for active RRH and inactive RRH).	87
6.2. Evolved Packet Core (EPC) network topology diagram.	92
6.3. Logical illustration of C-RAN testbed architecture.	92
6.4. C-RAN testbed implementation utilizing OAI.	93
6.5. Processing time of LTE subframes against CPU frequency with MCS = 27 and various PRB allocations.	95
6.6. CPU utilization of the VBS at different values of MCS and PRB.	96
6.7. Percentage of CPU usage versus the downlink throughput.	97
6.8. Minimum transmission power as a function of active RRH density ($\gamma = 10$ dB and $\sigma^2 = \lambda_r^a \times 10^{-4}$).	99
6.9. Minimum transmission power as a function of user density.	100
6.10. Coverage probability as a function of SINR threshold.	100
6.11. Area power consumption as a function of active RRH density.	101
6.12. RRH activity factor as a function of user density.	102
6.13. Minimum number of CPU cores for different number of PRBs ($\gamma = 10$ dB, and $\sigma^2 = \lambda_r^a \times 10^{-4}$).	102
6.14. Traffic fluctuation on a typical operational day for three different clusters.	103
6.15. Fluctuation of active RRH density to meet the user fluctuation for different times of the day.	103
6.16. Fluctuation of minimum transmission power to reduce the power consumption while guaranteeing a predefined Quality of Service (QoS).	104
6.17. Power consumption of different VBS-Clusters (CPU speed = 3.3 GHz).	104
6.18. Comparison of power consumption between Elastic-Net (in C-RAN) and Static-Net (in D-RAN) for (a) Cluster #1, (b) Cluster #2, and (c) Cluster #3.	105

Chapter 1

Introduction

1.1 Distributed Radio Access Network (D-RAN)

The most important part of a cellular wireless network is the Radio Access Network (RAN) that provides wide-area wireless connectivity for Mobile Stations (MSs). In general, up to 80% of the Capital Expenditure (CAPEX) of a mobile operator is spent on the RAN [1]. In conventional Distributed Radio Access Network (D-RAN) architectures, each Base Station (BS) only connects to a fixed number of sector antennae that cover a small area and only send/receive signals to/from the MSs in its coverage area. The hardware and processing equipment of each BS is located close to its antenna tower and there are no communication links connecting the BSs. Physical links only exist between BSs and their corresponding access network gateway. Hence, control messages between the BSs have to travel through costly backhaul links, and often even over a one-level higher layer in the aggregation hierarchy. The latency and scarce interconnect capacity among BSs have resulted in limited BS cooperation in practice. However, emerging wireless technologies such as *cooperative Multiple-Input Multiple-Output (MIMO)* or *coordinated scheduling and beamforming* require close cooperation among BSs.

1.1.1 Shortcomings of D-RAN

This section briefly presents the shortcomings that today's cellular networks are facing. In the next one we will introduce a new centralized architecture and emphasize its potentials to solve many – if not all – of these shortcomings.

High Power Consumption: To offer broadband wireless network and increase the coverage, operators continually increase the number of BSs. This leads to a dramatic rise in power consumption and consequently translates into higher Operational Expenditure (OPEX). Figures 1.1(a) and

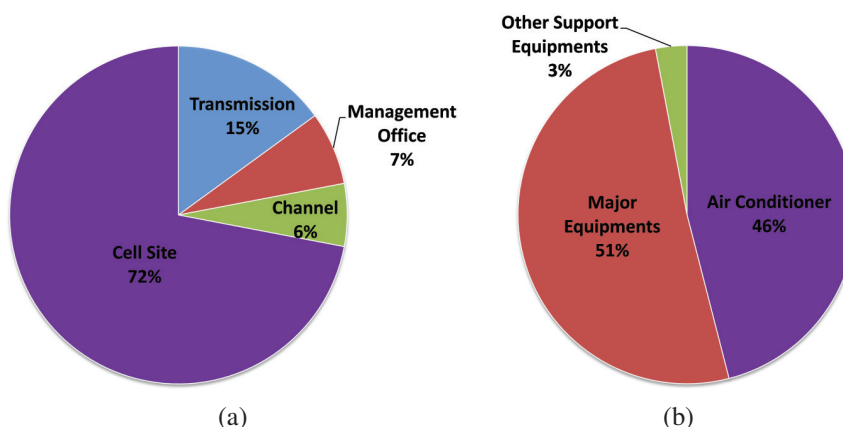


Figure 1.1: Power consumption of (a) the Radio Access Network (RAN) and (b) the Base Stations (BSs).

(b) show the components of power consumption reported by China Mobile [1]; here, the majority of power is consumed at BSs of the RAN. In each BS, the RAN equipments only consume half of the power, while the other half is used by air conditioning and by other equipment.

Rapidly Increasing CAPEX and OPEX: The proliferation of personal mobile computing devices along with a plethora of data-intensive mobile applications has resulted in a tremendous increase in demand for ubiquitous and high-data-rate wireless communications over the last few years. To satisfy such shift in consumer data-rate usage, mobile operators need to increase their network capacity. However, additional deployment and maintenance of a large number of stand-alone cellular BSs to meet the growing capacity demand are highly inefficient due to excessive capital and operating expenditures. Practically, up to 80% CAPEX of a mobile operator is spent on the RAN, which means that most of the CAPEX is spent on building up BSs. On the other hand, OPEX includes the costs for site and transmission network rentals, operation/maintenance, and bills from the power suppliers.

Multi-standard Environment: Today, BSs in wireless access networks make use of proprietary hardware designs and support specific standards. When the wireless network is upgraded, almost all of the network equipment must be replaced. Furthermore, during the transition, in order to satisfy the coexistence of new standards (such as WCDMA in 3G) and old standards (such as GSM in 2G), mobile operators must keep the old network and create another one for the new standard. Therefore, wireless network upgrades require huge financial investments and have often limited adoption of the emerging wireless technologies and algorithms.

Limited Inter-BS Cooperation: Traditional cellular wireless systems are suffering from limited inter-BS data exchange and do not allow to fully exploit the potential of cooperative communication schemes like macro-diversity and collaborative spatial multiplexing. In general, message between the BSs need to be exchanged through the expensive backhaul links, and perhaps even over one-level higher in the aggregation hierarchy. Currently, to perform cooperative communication schemes, it is proposed to divide a set of neighboring cells into clusters and connect the BSs via the Backhaul Processing Unit (BPU). However, even in this case, exchanging data between BSs in different clusters requires traveling over backhaul links. Hence, the cost, latency, and scarce interconnect capacity among BSs have limited BS cooperation schemes in practice.

Explosive Network Capacity Need: Global mobile traffic has been increased 66-fold with a Compound Annual Growth Rate (CAGR) of 131% between 2008 and 2013 [2]. On the other hand, the peak data rate has been only increased with a CAGR of 55% from UMTS to LTE-A, leading to a large gap between the CAGR of new air interface and the CAGR of customers' need. To fill this gap, new network architecture and infrastructure technologies need to be developed to further improve cellular-system performance.

Dynamic Network Load and Low BS Utilization: The number of active users at different locations varies depending on the time of the day. For example, during the day, the BSs in downtown office areas are the busiest, while at night, or in general during non-working hours, the BSs in residential or entertainment areas are the busiest. This movement of mobile network load based on the time of the day and the week is referred to as the "tidal effect". Today, each BS's processing capability is only used by the active users in its cell range, causing idle BSs in some areas/times and oversubscribed BSs in other areas. Static resource provisioning for the peak (worst case) at each cell site leads to grossly underutilized BSs in some areas/times while provisioning for the average leads to oversubscribed BSs in some areas/times.

1.2 Cloud Radio Access Network (C-RAN)

Cloud Radio Access Network (C-RAN) [1, 3] is introduced recently as a new architecture for the wireless cellular network to address the shortcomings of traditional D-RANs. In C-RAN, all the

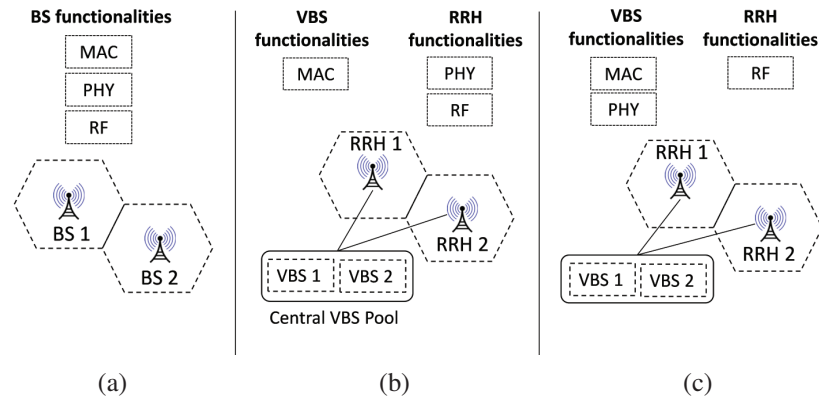


Figure 1.2: Distributed Cloud Radio Access Network (D-RAN) vs. two Cloud Radio Access Network (C-RAN). (a) D-RAN architecture; (b) Partially-centralized architecture: only MAC processing is centralized in Virtual Base Station (VBS) pool; (c) Fully-centralized architecture: VBS pool takes care of PHY and MAC processing.

BSs' computational resources are pooled in a central location, e.g., a set of physical servers in a datacenter, enabling communication among BSs with low latencies and exchange data at Gbps speeds. The main characteristics of C-RAN are: i) centralized management of computing resources, ii) re-configurability of spectrum resources, iii) collaborative communications, and iv) real-time cloud computing on generic platforms. C-RAN consists of three main parts: 1) Remote Radio Heads (RRHs) plus antennae, which are located at the remote site and are controlled by remote Virtual Base Stations (VBSs) housed in centralized BS pools, 2) the Base Band Unit (BBU) (VBS pool) composed of high-speed programmable processors and real-time virtualization technology to carry out the digital processing tasks, 3) low-latency high bandwidth optical fibers, which connect the RRHs to the VBS pool. As a precautionary measure and to be on the safe side, the optical fiber transmission latency is limited to less than 1% of the PHY processing latency [4]. Hence, the range of VBS pool is limited by latency constraints of wireless system and services.

Based on the functionality of the RRH and VBS pool, two architecture have been suggested for C-RAN: partially- and fully-centralized architectures (see Fig. 1.2). In the “partially-centralized” (Fig. 1.2 (b)) architecture, the PHY processing is integrated into the RRH, while a VBS only takes care of MAC processing. This leads to the advantage of a lower volume of data to be exchanged between RRH and BBU ($1/20 \sim 1/50$ of the original baseband I/Q sample data [1]) and also the wireless resources can be scheduled on a global level. However, the capability of PHY cooperative techniques becomes lower and we still require remote equipment rooms in cell sites. In the

“fully-centralized” (Fig. 1.2 (c)), a RRH only takes care of Radio Frequency (RF) functionalities, while a BBU (VBS pool) takes care of both PHY and MAC processing. With a fully-centralized architecture, we are more capable to do cooperative techniques; however, such architecture requires a higher bandwidth to exchange data between RRH and BBU.

1.2.1 Advantages of C-RAN

Lower Power Consumption: Since in C-RAN a group of BSs are centralized in a common place, the number of cell sites can be reduced several folds. Hence, the air conditioning and power consumption of other site support equipments can be dramatically reduced. In addition, since the cooperative interference reduction techniques can be applied among the RRHs, a higher density of RRHs is allowed. Hence, smaller cells with lower transmission power can be deployed, thus aiming for higher frequency reuse and capacity, while the network coverage is not affected.

Lower CAPEX and OPEX: Since in C-RAN all the BBUs and site support equipments of a large region are co-located in a common datacenter, it is much easier and cost efficient for centralized management, operation, and maintenance compared to traditional RAN. In addition, the functionalities of the RRHs in the C-RAN architecture are much simpler, leading both their size and power consumption to be reduced so that they can be installed on top of buildings with minimum site support and management. Thus, operators can get large cost savings on site rental, operation, and maintenance, leading to lower OPEX and CAPEX.

Flexibility to Add New Standards: In C-RAN, the large scale BBU pool with high-speed low-latency interconnection, the common platform of Digital Signal Processor (DSP)/General Purpose Processors (GPP), and open Software Defined Radio (SDR) solution enable a cost-effective realization of VBSs. Therefore, in order to add/support new standards, there is no need to replace the equipment; conversely, it would suffice assigning new VBSs in the platform. As a result, CAPEX and OPEX costs associated with the wireless network upgrading can be eliminated altogether.

High Speed Inter-BS Coordination: With the consolidation of BSs in a centralized VBS pool, such consolidated/co-located BSs can talk to each other at Gbps speeds and can communicate at low latencies, quasi real time. High-speed communication between the BSs can bring an extra degree of freedom to make optimal decisions and fully exploit the potentials of cooperative techniques. As an example, a few approaches where cooperation among BSs can be beneficial are: i) joint flow

scheduling and load balancing, ii) interference management, iii) cooperative spatial multiplexing and macro-diversity, and iv) mobility management.

Capacity Improvement: In C-RAN, VBSs are able to exchange the signaling, traffic data, and Channel State Information (CSI) of active MSs in the system with low latency. This way, it becomes much easier to implement joint processing & scheduling algorithms so to mitigate Inter-Cell Interference (ICI) and improve spectral efficiency. For example, CoMP schemes can efficiently be implemented under the C-RAN architecture.

High BS Utilization Rate: C-RAN is also suitable to handle non-uniformly distributed traffic due to its intrinsic load-balancing capability in the centralized BBU pool. Although the serving RRH changes dynamically according to the movement of the MSs, the serving BBU is still in the same BBU pool. As the coverage of a BBU pool is larger than in traditional BS, non-uniformly distributed traffic generated from MSs can be distributed in a VBS as this sits in the same BBU pool.

1.3 Contribution

In order to address the research challenges associated with increasing the spectral and energy efficiency in the next generation of wireless cellular network, we make the following contributions in this dissertation.

1.3.1 Blind Source Separation for Cooperative Cellular Communication in C-RAN

We proposed an uplink *cooperative joint PHY and MAC* solution for next-generation cellular communications that exploits synergistically the advantages of C-RAN and Blind Source Separation (BSS) [5]. BSS is a well-known technique in signal processing to recover the underlying source signals from a set of mixtures, where the mixing system is unknown. C-RAN's characteristics are well suited for BSS-based cooperative cellular communications as the source separation problem relies on inter-BS cooperation. In our solution, named *Cloud-BSS*, we divide a set of neighboring cells into *clusters* and allow them to use all of the frequency channels in the system band. In each cluster, the RRHs receive a mixture of the MS signals. Then, the MS signals are separated from the mixtures through BSS. *Cloud-BSS* provides the following benefits: i) enhancement of the

cluster spectral efficiency, ii) decrease in the number of handovers, iii) elimination of the need for bandwidth-consuming channel estimation, and iv) interference mitigation. We study our solution under different network topologies and introduce a strategy, named *Channel-Select*, to increase the Signal-to-Noise Ratio (SNR) of the estimated signals. In other words, *Cloud-BSS* separates the intra-cluster mixtures and *Channel-Select* mitigates the defective impact of background noise (including inter-cluster interference) during the separation process.

1.3.2 Dynamic Joint Processing for Interference Cancellation in C-RAN

We leveraged the C-RAN architecture to exploit fully the potential of CoMP so to suppress the ICI and increase system spectral efficiency. Specifically, we proposed a novel uplink clustering scheme, called *Dynamic Joint Processing (DJP)*, which decreases *both* the intra- and inter-cluster interference without increasing the size of clusters [6, 7]. Firstly, we introduce the idea of “*VBS-Cluster*”, in which we merge VBSs serving a cluster into a unit VBS-Cluster while the RRHs’ antennae in each cluster act as a single coherent antenna array distributed over the cluster region. Then, in the proposed solution, we divide the MSs into two categories based on their average velocity: 1) low-mobility and 2) high-mobility MSs. Based on the mobility level of the MSs, we present two different coexisting clustering approaches and propose to exploit their complementary advantages simultaneously.

1.3.3 Coordinated Fractional Frequency Reuse in C-RAN

we leveraged the advantages of FFR, CoMP and C-RAN, and proposed a *joint clustering and spectrum sharing scheme* for uplink interference-cancellation so as to increase the system spectral efficiency and also decrease *both* the intra- and inter-cluster interference [8–10]. In the proposed solution, called *Cloud-CFFR*, for each cell we defined an Interference Region (IR); based on the IR of its neighboring cells, we then determined the Cell-Center Region (CCR). Since the cell-center MSs experience a high SINR, we proposed to apply CoMP processing *only* to cell-edge MSs, leading to a decrease in the total complexity and latency. This way, unlike in traditional OFDMA systems, the performance of the system in *all* the cell-edge regions relies on the cooperation of different VBSs. Moreover, in order to deal with inter-cluster interference, which is not addressed in traditional CoMP, we proposed a joint region-based clustering and spectrum allocation. We defined

the clusters of size 2 and 3 depending on the IR intersection of neighboring cells; we partitioned the frequency band into 13 non-overlapping bands, and allocated the frequency subbands to the MSs based on their position. In our solution, we also dynamically changed the boundaries of subbands and optimized their widths in order to address the unanticipated fluctuations in the number of active users and per-user capacity demands.

1.3.4 Demand-Aware Resource Allocation for High Energy Efficiency and Resource Utilization in C-RAN

We focused on optimizing the power consumption and resource utilization by leveraging the full potential of C-RAN architecture. We proposed a novel elastic resource provisioning framework, called *Elastic-Net*, to minimize the power consumption while addressing the fluctuations in per-user capacity demand [11–14]. In our solution, we divide the covered region into clusters based on the traffic model and, within each cluster, we dynamically adapt the active RRH density, transmission power, and size of the VM based on the traffic fluctuations. We also provide a comprehensive model for the power consumption of the C-RAN system including: (i) RRH and transport network power consumption and (ii) VBS pool power consumption. Then, we optimize the power consumption and resource utilization through a demand-aware resource provisioning approach. In order to minimize the power consumption in the cell sites while ensuring a certain minimum coverage and data rate, we propose to dynamically optimize and adapt the RRH density and transmission power based on the traffic demand and user density. Likewise, in order to minimize the power consumption in the cloud we dynamically optimize and adapt the size of the VMs while ensuring that the frame-processing time is less than the frame deadline.

1.4 Dissertation Organization

This rest of this dissertation is organized as follows.

Chapter 2 reviews related and prior work in the fields of C-RAN. The proposed approaches are discussed along with their pros and cons.

Chapter 3 details our interference separation algorithm proposed for uplink C-RAN. We explore the performance of the BSS under different network topologies and introduce a strategy,

named *Channel-Select*, to increase the SNR of the estimated signals. We introduce a metric to measure how much a $M \times N$ mixing matrix is diagonal dominant and use it in the simulation analysis to show the performance associated with different topologies.

Chapter 4 explains our dynamic joint processing framework for interference cancellation in C-RAN. Two coexisting clustering approaches are presented based on the level of mobility of MSs. We also explain how the proposed solution increase the spectral and energy efficiency and Monte Carlo simulations show the potential of our solution towards next-generation green communications.

Chapter 5 explains our joint clustering and spectrum sharing scheme for uplink interference cancellation in C-RAN. For each cell an interference region is defined based on the interference region of its neighboring cells. Then, cell-center and cell-edge regions are determined based on the intersections of interference regions. Moreover, a dynamic spectrum allocation scheme is proposed to address the unanticipated fluctuations in the number of active users and per-user capacity demands.

Chapter 6 studies the elastic resource provisioning solution. We explain how to dynamically adapt the active RRH density, transmission power, and size of the VM based on the traffic fluctuations so that the power consumption is minimized while the resource utilization is maximized. We also provide an extensive range of simulations and emulations results to validate our statements and show the benefits of the proposed solution compared to static provisioning.

Chapter 7 summarizes our contributions as well as our observations and provides suggestions for future research directions that will push the state of the art in spectral and energy efficiency of C-RANs.

Chapter 2

Background and Related Works

In this chapter we explain the technical challenges of C-RAN architecture, research challenges of existing RAN, and the works that have been done so far to address those challenges.

2.1 Software Defined Virtual Base Station Pool

Today's BSs are equipped with a set of heterogeneous processing devices, each of which executes a specific task as defined at the design time. At the time of upgrading the network, almost all of the network equipment must be replaced. With DSP, GPP, and emerging SDR frameworks, we are now able to reconfigure the radio equipment. Large-scale BBUs endowed with high-speed, low-latency interconnection, plus the programmable DSP/GPP and open SDR solutions set the base for a VBS. In the C-RAN architecture a bunch of VBSs are pooled in a common BBU where a large amount of computing resources is available. Hence, VBS pool contains all the required processing resources of traditional BSs including entire digital signal processing at the PHY layer and packet processing at the MAC layer.

With virtualization technology we can dynamically allocate processing resources within a BBU to different VBSs. Whenever a user requests a service, computing resources need to be allocated for the corresponding service. This leads to a greater utilization of the processing resources and the ability to adjust in response to the tidal effects in different areas so to accommodate fluctuating demands. However, in general we are not able to pool all the VBSs together as there are some constraints to take into account. The range of VBS pool is limited and depends on the latency constraints of the wireless networks. In C-RAN, the optical fiber transmission latency is suggested to be less than 1% of the PHY processing latency [4]. Assuming a PHY processing latency of 10 ms, the fiber transmission latency should be less than 0.1 ms. Since the signal speed through the fiber is $\approx 2 \times 10^8$ m/s, a signal path of 20 km has a latency of ≈ 0.1 ms. Consequently, a region with

radius of 10 km is able to cover 314 km^2 of a metropolitan area, which may serve millions of users.

2.2 Technical Challenges of C-RAN Deployment

BSs have strict real-time, low-latency, and high-performance requirements, to meet which the traditional virtualization technique is challenged. Specifically, to deploy real-time VBS pool the following requirements need to be met [1]:

- Advanced processing algorithms for real-time signals.
- High-performance, low-power processing for wireless signals.
- High-bandwidth, low-latency, low-cost BBU interconnection topology among physical processing resources in the baseband pool. These include the interconnection among the chips in a BBU, among the BBUs in a physical rack, and across multiple racks in datacenter.
- Efficient and flexible real-time operating systems to achieve virtualization of hardware processing resources management and dynamic allocation of physical processing resources to each VBS so to ensure processing latency and jitter control hardware-level support on virtualization.

2.3 Research Challenges of Future Wireless Cellular Network

Over the last few years, proliferation of personal mobile computing devices like tablets and smartphones along with a plethora of data-intensive mobile applications has resulted in a tremendous increase in demand for ubiquitous and high data rate wireless communications. However, the system capacity is limited by the interference, which makes it difficult to improve the spectral efficiency and consequently data rate. To solve this problem, the Fourth Generation (4G) cellular communication system with peak downlink data rate of 1 Gbps has been envisioned. Long Term Evolution (LTE) systems based on Orthogonal Frequency Division Multiple Access (OFDMA) represent a major breakthrough in terms of achieving downlink peak data rates of 300 Mbps [15]. However, cooperative schemes used in LTE to increase the spectral efficiency cannot be fully deployed due to the scarce inter-BS connectivity. Hence, LTE systems do not match yet the International Mobile

Telecommunications Advanced (IMT-Advanced) “True 4G” requirements. Hence, a significant effort is being made towards the development of Fifth Generation (5G) of wireless cellular network. An estimated area capacity of 25 Gbps/km² is forecast for 5G wireless cellular networks, which corresponds to a 100× boost over what the current 4G wireless standard is able to provide in terms of spectral efficiency. Additionally, to reduce energy consumption, a 1000× improvement in energy efficiency is expected by 2020.

The current practice to enhance spectral efficiency and data rate is to increase the number of BSs and go for smaller cells so to increase the band reuse factor. However, additional deployment and maintenance of a large number of cellular BSs are highly inefficient due to excessive capital and operational expenditures. Moreover, with small cells the MSs experience a higher number of handovers and the ICI problem becomes more challenging. The economic impact of power consumption is particularly dire in emerging markets and the 5G network must be not only spectral efficient but also energy efficient. Currently, RANs consume more than 70% of total power consumption (each BS consumes an average of 25 MWh per year) [16]. *It is also studied that increasing the BS density or the number of transmit antennas will decrease the energy efficiency due to the dynamic traffic variation* [17].

Although several recent efforts have been made to reduce the power consumption of existing small cell networks [18, 19], limited attention has been given to optimize the overall network deployment. Therefore, a novel design and architecture is necessary to increase the spectral and energy efficiency of the next generation of wireless cellular network.

2.4 State of the Art in C-RAN

There are only a few works that have started to address some of the aforementioned challenges. In [3] and [20], the authors introduce the centralized-BS idea and study its advantages, challenges, and requirements. The authors in [4] refer to C-RAN as SDR cloud and suggest hierarchical resource management where computing clusters are defined and assigned to different radio operators, cells, or services. The authors of [21] introduce a reconfigurable backhaul scheme to allow for a flexible mapping between the BBUs and Radio Access Units (RAUs); by real-world experiments, they show that their proposed solution improves the RAN performance and decreases the energy

consumption. In [22], the authors propose a cross-layer resource allocation model in which they optimize the set of selected RRHs and the beamforming strategies at the active RRHs in order to minimize the overall system power consumption.

In [3], the authors recommend that timing and synchronization system should have two parts: the first, namely, master time server, provides the accurate timing reference, while the second distributes the precise timing signal throughout the VBS pool and RRHs. The authors also suggest to use standardized interface technologies widely used in IT infrastructure (GbE, 10-GbE, Infini-Band, and PCIe) to interconnect BBUs. For hardware efficiency and flexible collaboration, the same authors also propose to separate the PHY and MAC layers into different platforms. In [4], a hierarchical management is suggested, where computing resources are assigned on demand and in real time to different radio operators, cells, or services. The authors of [4] also discuss the complexity of some resource-management algorithms and introduce different management schemes in simulated VBS pool. In [23], the constraints of PHY and MAC layers are analyzed and the VBS performance is optimized to meet the stringent real-time requirements of jitter and latency. The authors of [23] also present the first working prototype of a VBS pool on a multi-core IT platform; specifically, they show that their VBS pool prototype for WiMax can meet system requirements including synchronization, latency, and jitter. The authors of [24] propose some low-complexity algorithms to minimize the network power consumption of C-RAN, including the transport network and radio access network power consumption. They formulate the network power consumption and propose an algorithm to switch off one RRH at each step. Then, to reduce the complexity, they propose a three-stage group sparse beamforming framework. In [25], the impact of end-user behavior on user/network association in a HetNet with multiple service providers (SPs) has been studied. Specifically, the uncertainty in the service guarantees offered by SPs in a HetNet has been modeled using Prospect Theory (PT), a noble prize-winning theory, which explain real life decision making problem to investigate the end-user decision making behavior.

In [26], a partitioning and scheduling framework is proposed which is able to reduce the compute resources by 19%. In [27], the authors present a flexible framework for small cells, called Fluidnet, which dynamically reconfigures the front-haul based on network feedback to maximize the amount of traffic demand and optimize the compute resource usage in the BBU pool. The authors of [28] consider the coordinated transmission problem to minimize the downlink power in

C-RAN. In order to serve each MS, they determine a set of RRHs and the precoding vectors for the RRHs to minimize the total transmission power subject to the constraints on fronthaul capacity. In [29], the authors consider the C-RAN with finite-capacity backhaul links and propose a hybrid compression and message sharing strategy for downlink transmission to optimize the backhaul capacity utilization. In [24], the authors propose low-complexity, three-stage group-sparse beamforming algorithms to minimize the network power consumption in C-RAN. In [26], a partitioning and scheduling framework is proposed that is able to reduce the computing resources by 19%. The authors of [30], propose a user scheduling, user-centric BS clustering and beamforming design for the downlink C-RAN. They numerically show that with explicit per-BS backhaul constraints, their proposed algorithm is able to utilize the backhaul resources more efficiently, as well as to offer more flexibility in choosing the cluster size. In [31, 32], the authors have proposed a competitive spectrum allocation scheme to serve the maximum number of users by strategically allocating limited spectrum resources.

The authors in [33] introduce Heterogeneous Cloud Radio Access Networks (H-CRAN) architecture and propose a framework to decrease the circuit power consumption of fronthaul links. In [34], the authors present a joint spectral and energy efficient framework with user-centric design in C-RAN for greener 5G networks. In [35], the authors propose a joint downlink and uplink beamforming design to coordinate interference in the C-RAN for energy minimization. In [10, 36, 37], the authors envisage a real-time, context-aware collaboration framework that lies at the edge of the RAN, comprising Mobile Edge Computing (MEC) servers and mobile devices, and that amalgamates the heterogeneous resources at the edge. The authors introduce and study three representative use-cases ranging from mobile-edge orchestration, collaborative caching and processing, and multi-layer interference cancellation. The authors in [38, 39] propose a collaborative joint caching and processing strategy for on-demand video streaming in MEC networks. Their design aims at enhancing the widely used Adaptive BitRate (ABR) streaming technology, where multiple bitrate versions of a video can be delivered so as to adapt to the heterogeneity of user capabilities and the varying of network condition. In [40, 41], the authors introduce a new layer of caching in the C-RAN network, named *cloud cache* which bridges the latency/capacity gap between the traditional edge-based and core-based caching schemes. A coded caching strategy taking into account the user mobility pattern in a C-RAN was studied in [42].

In [43], the authors have studied the feasibility of using interference alignment in underwater acoustic communication to increase the data rate and spectral efficiency for ocean explorations. In [44], using the features available in the 5G design such as Mobile Edge Computing (MEC), caching and CRAN, a dynamic processing location management platform is proposed to minimize latency and avoid bottlenecks. The authors also proposed a centralized algorithm for dynamic orchestration of processing functionalities locations. In [45], authors investigate the capacity using uncoded caching and categorization based on coded caching scheme. In their cache placement strategy, file groups are created with similar popularity levels and then the files are randomly coded in each file group to reduce the average traffic of backend. An experimental study in a C-RAN testbed was carried out in [46] to characterize the computational requirement of the BBU pool running on virtualized environment. In [47, 48], the authors proposed a dynamic joint user-centric clustering and beamforming to maximize the weighted-sum rate performance in a downlink C-RAN.

In [49, 50], a new incentive model for Information-Centric Networks, which is a promised solution for next generation networks, has been proposed. To determine caching and pricing strategies, a theoretical game model is presented in a hierarchical architecture of one content provider, one transit ICN and K access ICN with different type of content which are requested with Zipf-like distribution. The authors have shown that this game has a unique Nash equilibrium. They have provided a monetary incentive model to collaborate in caching and distributing content where the caching costs vary with respect to content popularity, while the content provider cost per unit data is fixed for all content types. The authors in [51] formulate the computation resource allocation problem in C-RANs as a bin packing problem and propose a heuristic simulated annealing algorithm to reduce power consumption of the VBS pool. In [52], an energy efficient optimization problem with the resource assignment and power allocation is solved to reduce the energy cost of RRHs. In [29], the authors consider the C-RAN with finite-capacity backhaul links and propose a hybrid compression strategy for downlink transmission to optimize the backhaul capacity utilization. In [53], a queue-aware robust (QuaRo) coordinated transmission strategy is proposed for C-RANs which is adaptive to both user-traffic urgency via Queue State Information (QSI) and wireless channel opportunity via the observed (yet imperfect) Channel State Information (CSI).

In summary, prior works on C-RAN focused on the overall system architecture, on the feasibility of virtual software BS stacks, on energy optimization as well as on the performance gains. In

contrast to existing works, we propose novel dynamic solutions to increase the spectral and energy efficiency. We leverage the centralized characteristics of C-RAN and propose different algorithms to exploit fully the potential of coordinated interference cancellation techniques so that to decrease the ICI. We also plan to study a *demand-aware resource provisioning* solution in which the network parameters will be optimized and adapted based on the traffic fluctuation so that the power consumption is minimized.

Chapter 3

Blind Source Separation for Cooperative Cellular Communication in C-RAN

3.1 Overview

Generally, in cellular networks, neighboring cells avoid to reuse the same set of frequencies (or channels) so to keep the interference below a certain threshold and to ensure user Quality of Service (QoS). As a drawback, however, the whole cellular band cannot be used by the cells, which leads to low data rates. In this chapter, we present *Cloud-BSS*, our BSS-based solution, which increases the user capacity – thus achieving high data rates – by exploiting the characteristics of the C-RAN architecture; specifically, *Cloud-BSS* is able 1) to grant multiple users access to the same OFDMA channels simultaneously and 2) to assign multiple channels to the same user [5]. These features, together, lead to a higher per-user capacity and hence, data rate, given a fixed cellular band. We also explain how the proposed solution mitigates the interference problem and decreases the number of handovers, regardless of the handover procedure used by the system. In fact, a handover will only be needed when a MS moves from one cluster to another (as opposed to from one cell to another). In other words, as long as a MS remains in a certain cluster, no handover is needed, which provides the following advantages: an increase in user QoS and a decrease in overall system computation and communication overhead.

In *Cloud-BSS*, we divide a set of contiguous cells into a *cluster* and allow them to use all of the frequency channels in the system band, *thus achieving a frequency-reuse factor of 1*. Hence, in each cluster, the RRHs receive a mixture of the MS signals. Figure 3.1(a) shows our clustering idea: here the cluster size is 3 and a_{ij} is the channel coefficient between MS # j and RRH # i . The relationship between the *received RRH* and the *transmitted MS signals* at different time instants can

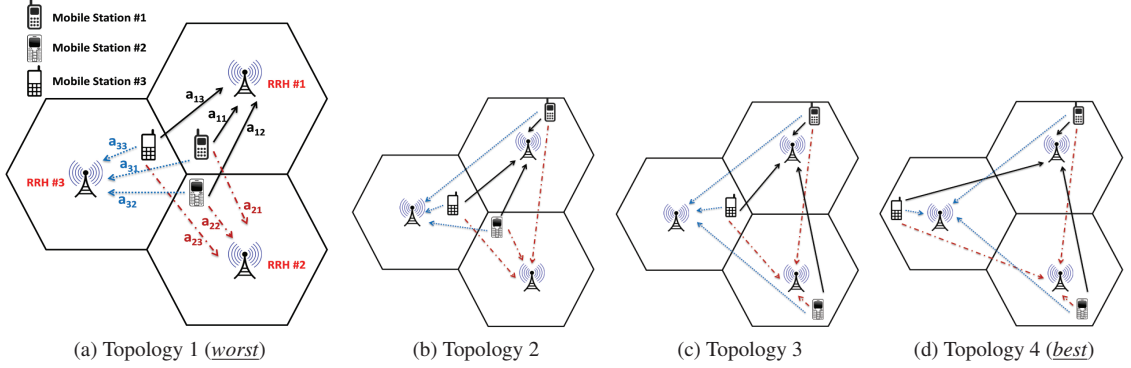


Figure 3.1: Four network topologies in which the RRHs receive different combinations (‘mixtures’) of the MS signals. From Topology 1 to 4 (worst to best), the distance between a MS in a cell and the RRHs in the other cells becomes higher.

be expressed through the following linear noisy model (for clarity time is omitted),

$$\mathbf{x} = \sum_{i=1}^N s_i \mathbf{a}_i + \mathbf{n} = \mathbf{A}\mathbf{s} + \mathbf{n}. \quad (3.1)$$

Here, $\mathbf{s} = [s_1, \dots, s_N]^T$ is the $N \times 1$ vector of complex-valued MS signals (sources), $\mathbf{x} = [x_1, \dots, x_M]^T$ is the $M \times 1$ vector of signals (mixtures) received by the RRHs, \mathbf{A} is the $M \times N$ complex-valued channel coefficient (mixing) matrix with linearly independent columns (\mathbf{a}_i being its i^{th} column), and $\mathbf{n} = [n_1, \dots, n_M]^T$ is the $M \times 1$ Gaussian noise vector with independent and identically-distributed (i.i.d.) components. Note that, in (3.1), the inter-cluster interference is part of the background noise, and that the MS signals are assumed to be *statistically independent*; such assumption is almost always met in practice for physically-separated transmitters. Now, to extract the MS data in the VBS pool we need to separate the MS signals (sources) from the received RRH signals (mixtures); *in a cluster, this is in fact a BSS problem.*

First, we provide some preliminary background on BSS and Independent Component Analysis (ICA). Then, we argue that the topology configuration of the MSs affects the system performance and show that *diagonal dominant topologies* lead to better performance, i.e., to a lower Bit Error Rate (BER). We introduce a metric to measure how much a $M \times N$ mixing matrix is diagonal dominant and use it in the simulation analysis to show the performance associated with different topologies. Finally, we introduce a strategy, named *Channel-Select*, to ‘group’ the best set of active MSs (i.e., assign them to the same OFDMA channel) based on their locations so to induce diagonal dominance in the mixing matrices.

3.2 Blind Source Separation (BSS)

In BSS, a set of mixtures of different source signals is available and the goal is to separate the source signals when we have no information about the mixing system or the source signals (hence the name *blind*) [54]. The mixing and separating systems can be represented mathematically as,

$$\mathbf{x}(t) = \mathbf{A}\mathbf{s}(t), \quad \mathbf{y}(t) = \mathbf{B}\mathbf{x}(t), \quad (3.2)$$

where $\mathbf{s}(t) = [s_1(t), \dots, s_N(t)]^T$ is the vector of sources that are mixed by the mixing matrix \mathbf{A} and $\mathbf{x}(t) = [x_1(t), \dots, x_M(t)]^T$ is the vector of available observations. Let \mathbf{A} be a $M \times N$ matrix of full-column rank, which means that the observations are linearly independent; the goal is to design a separating matrix \mathbf{B} such that $\mathbf{y}(t) = [y_1(t), \dots, y_N(t)]^T$ is an estimate of the sources. A method to solve BSS is ICA, which exploits the assumption of *source independence* and estimates \mathbf{B} such that the outputs $y_i(t)$ s are statistically independent. For this assumption to hold, however, the number of observations must be equal or greater than the number of sources (i.e., $M \geq N$). The essence of ICA can be understood better by considering the “*cocktail party problem*,” in which many people are talking simultaneously: if several microphones at different positions are available, then different mixtures of the voices can be recorded. Given such mixtures and the assumption that the original voice signals are independent from each other, ICA can recover the original voices from the mixtures. However, most of the ICA algorithms are only applicable to real signals, whereas in digital communication systems we deal with complex-valued signals. To solve this problem, some ICA algorithms have been proposed (such as the ones in [55–57]) to deal with complex-valued signals.

3.3 Blind Source Separation for Cooperative Communication in Cloud (Cloud-BSS)

In cellular networks the interfering signals from other cells decrease the performance of the system. To overcome this problem, BSs avoid reuse of the same set of frequencies. However, in the case of C-RAN, as we have access to all of the BSs’ received signals in a cluster, the MS signals can be separated by the use of ICA algorithms. Hence, with reference to the model in (3.1), since we have access to all the x_i s ($1 \leq i \leq M$), we can separate the MS signals (sources) from the RRH

signals (mixtures) through ICA. Note that it was studied in [55] that the case of multiple paths, where several coherent wireless signals from a single transmitter are mixed in the received signal, does not affect the ICA problem.

Without considering the noise – and as long as the sources are independent and the mixing channel coefficient matrix is full rank – ICA methods can extract the source signals simply by estimating the inverse of the mixing matrix. However, in the presence of noise, when the ICA algorithms estimate \mathbf{B} as $\widehat{\mathbf{A}}^{-1}$ and multiply it by the observation so to extract the source signals, from (3.1) we obtain,

$$\mathbf{B}\mathbf{x}(t) = \hat{\mathbf{s}}(t) + \mathbf{B}\mathbf{n}(t), \quad (3.3)$$

where each estimated source signal is associated with a combination of the additive noises at all the receivers. If we assume that the noises at all the receivers have the same variance σ_n^2 , then the noise in the i^{th} estimated source has a variance of $(b_{i1}^2 + \dots + b_{iM}^2) \cdot \sigma_n^2$, where b_{ij} is the $(i, j)^{th}$ component of the separation matrix \mathbf{B} . As the b_{ij} s are dependent on the *determinant* of the mixing matrix \mathbf{A} , the noise level of the estimated sources is highly dependent on the mixing matrix. The determinant of a matrix is the volume of the parallelepiped composed of its rows/columns. It is straightforward to prove that if a diagonal dominant¹ and a non-diagonal dominant matrix have the same row/column norm, then the former has the greater determinant and, hence, lower component values in its inverse matrix [58].

Theorem 1. *Let us assume that a $N \times N$ matrix \mathbf{C} is diagonally dominant by rows, and let us set $\beta = \min_i (|c_{ii}| - \sum_{j \neq i} |c_{ij}|)$. It follows that $\|\mathbf{C}^{-1}\|_\infty < 1/\beta$.*

Proof. Since $\|\mathbf{C}^{-1}\|_\infty^{-1} = \inf_x \frac{\|\mathbf{C}\mathbf{x}\|_\infty}{\|\mathbf{x}\|_\infty}$, we only need to show that $\alpha\|\mathbf{x}\|_\infty \leq \|\mathbf{C}\mathbf{x}\|_\infty$ for all \mathbf{x} . Take some vector \mathbf{x} and let $\|\mathbf{x}\|_\infty = |x_i|$; then, it follows that $0 < \alpha \leq |c_{ii}| - \sum_{j \neq i} |c_{ij}|$. With some manipulation, we have,

$$0 < \alpha |x_i| \leq |c_{ii}x_i| - \sum_{j \neq i} |c_{ij}x_j| \leq |c_{ii}x_i| - \left| \sum_{j \neq i} c_{ij}x_j \right| \leq \left| \sum_j c_{ij}x_j \right| \leq \max_i \left| \sum_j c_{ij}x_j \right| = \|\mathbf{C}\mathbf{x}\|_\infty. \quad \square$$

From Theorem 1, we infer that when β is low the upper bound of $\|\mathbf{C}^{-1}\|_\infty$, which is the

¹A matrix is said to be diagonally dominant if, for every row/column, the magnitude of the diagonal entry in a row/column is larger than the sum of the magnitudes of all the other entries in that row/column.

maximum absolute row sum of the matrix \mathbf{C}^{-1} , becomes high. Hence, considering \mathbf{A} to be a $N \times N$, when the non-diagonal components of the mixing channel coefficient matrix \mathbf{A} in each row are close to the diagonal component, β becomes lower and, as a drawback, the maximum absolute row sum of the separation matrix \mathbf{B} becomes higher, leading to low SNR in the estimated sources in (3.3). Hence, in order to have a high SNR in the estimated source signals, the absolute value of the diagonal dominant component of \mathbf{A} should be as high as possible, and the absolute value of non-diagonal components of \mathbf{A} should be as low as possible. *This translates into the following observation: in a certain frequency channel, the i^{th} MS needs to be as close as possible and the j^{th} MS needs to be as far as possible to the i^{th} RRH (with $j \neq i$).*

3.3.1 System Performance for Different Topologies

In our solution, where the mixing channel coefficient matrix depends on the topology of the network, we expect that for different network topologies the performance would vary. Depending on the topology, the mixing channel coefficient matrix \mathbf{A} and thus the variance of the noise in the estimated sources are different. As we discussed earlier, we expect that for topologies with a diagonally dominant mixing (channel coefficient) matrix the performance would be better than for topologies with a non-diagonally dominant mixing matrix; in the diagonally dominant case, in fact, the variance of the noise associated with each estimated transmitted signal is lower than in the non-diagonally dominant case. *Hence, the more diagonal dominant the mixing matrix, the better the performance.* Based on the formulation we described for Fig. 3.1(a), we introduce metric $D(\mathbf{A})$ to define how much a $M \times N$ mixing matrix \mathbf{A} is row diagonally dominant as,

$$D(\mathbf{A}) = \frac{1}{N(N-1)} \sum_{j=1}^N \left(\frac{\sum_{k=1}^N |a_{ik}|}{\max_i |a_{ij}|} - 1 \right), \quad (3.4)$$

where a_{ij} is the $(i, j)^{\text{th}}$ component of matrix \mathbf{A} and $\max_i |a_{ij}|$ is the maximum absolute value in the j^{th} column of the matrix. In (3.4), we find the maximum components in each column of matrix \mathbf{A} , then perform a normalized sum only over those rows where the maximum components exist. In fact, in the mixing matrix \mathbf{A} , the components of each column/row correspond to a certain MS/RRH, respectively. In the case where $N < M$, (3.4) eliminates $(M - N)$ rows corresponding to the RRHs for which there is no MS in their cells. With this definition, $D(\mathbf{A})$ always ranges in $[0, 1]$, being

equal to 0 when \mathbf{A} is diagonal. For the topologies in which $D(\mathbf{A})$ is high, the maximum absolute row sum of the separation matrix \mathbf{B} becomes higher than for the topologies with lower $D(\mathbf{A})$. An increase in $D(\mathbf{A})$ causes a decrease in SNR and consequently an increase in the BER. Figure 3.2 shows the increase of the BER as $D(\mathbf{A})$ approaches 1, for the cases of $N = M = 3, 4, 5$ and SNR= 15 dB.

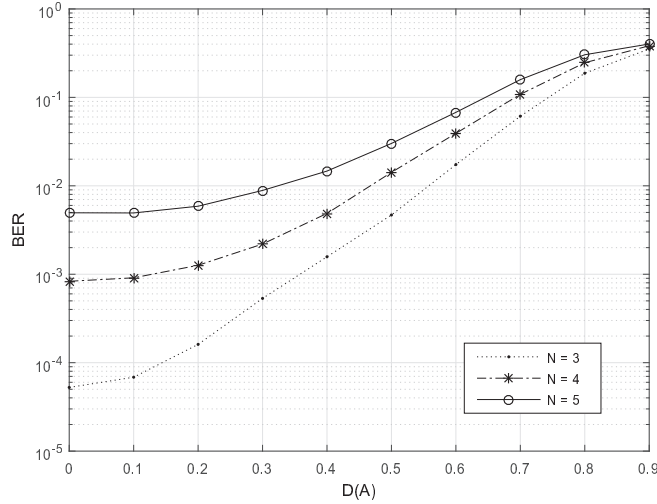


Figure 3.2: Increase in Bit Error Rate (BER) with increase in non-diagonal dominance of mixing matrix \mathbf{A} (the closer $D(\mathbf{A})$ to 1, the more \mathbf{A} is non-diagonal dominant); note that in this simulation we considered $N = M$.

To verify that the system performance depends on the topology – as inferred from the above mathematical analysis – we analyzed four topologies, as shown in Fig. 3.1, and considered a cluster of three cells. We implemented the JADE algorithm [55] for separating the MS signals from their mixtures. JADE uses the whole fourth-order statistics of the received data, from which very good separation results can be achieved. In Topology 1 (worst), the channel coefficient matrix \mathbf{A} is not diagonally dominant at all, whereas in Topology 4 (best) all of the columns of the matrix are diagonally dominant. In between, we have Topology 2 and 3, in which only one and two columns, respectively, are diagonally dominant. If we consider $D_l(\mathbf{A})$ as the diagonal dominance metric of the l^{th} topology, then we have $D_4(\mathbf{A}) < D_3(\mathbf{A}) < D_2(\mathbf{A}) < D_1(\mathbf{A})$. Consequently, moving *orderly* from Topology 1 to 4, we expect progressively better performance due to the decrease in noise level of the estimated MS signals. The decreasing BER curves with the SNR (*not surprising*) and with topology order (*corroborating our analysis*) are depicted in Fig. 3.3.

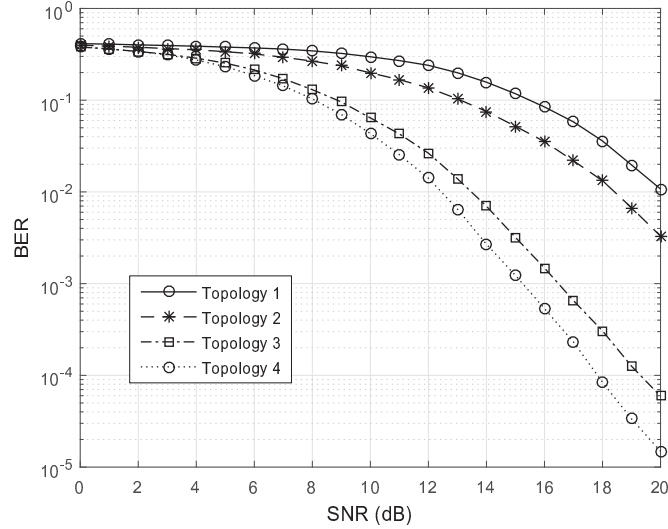


Figure 3.3: Decrease in BER with Signal-to-Noise Ratio (SNR) and topology order for each of the four different topologies considered in Fig. 3.1.

3.3.2 Proposed Strategy for Operation under Non Idealities

We propose the *Channel-Select* strategy, which changes the transmitting frequency (channel) of each user so to make the mixing matrices “as diagonally dominant as possible”. Depending on the ‘instantaneous’ topology, we optimize the frequency allocation for each MS so that the channel coefficient matrix in each channel is as diagonal dominant as possible. To achieve this goal, *Channel-Select* uses the following objective function,

$$\mathcal{F}(\mathbf{A}_1, \dots, \mathbf{A}_L) = \min \max[D(\mathbf{A}_1), \dots, D(\mathbf{A}_L)], \quad (3.5)$$

where \mathbf{A}_l is the mixing matrix in the l^{th} frequency channel f_l and L is the total number of channels available in the OFDMA system. The complexity of this combinatorial optimization problem depends on the number of MSs and cluster size, and grows exponentially as these parameters increase. Assuming K MSs are uniformly distributed in the cluster, the problem complexity is $\mathcal{O}((K/M)^M)$: consequently, as we are dealing with a large number of MSs in a cluster, a solution under real-world timing constraints is infeasible. Therefore, we introduce a simple heuristic algorithm that makes the diagonal and non-diagonal component of matrix \mathbf{A} higher and lower, respectively, causing $D(\mathbf{A}_l)$'s in (3.5) to be low.

Without any loss in generality, we assume that: **(i)** We have L frequency channels (f_1, \dots, f_L) and K MSs; **(ii)** We have enough frequency channels to admit all the users in each cell; **(iii)** All cells have the same size and in each cluster all the RRHs can receive all the MSs' signals; **(iv)** All MSs use the same output power (i.e., no power control is performed); **(v)** We approximately know where the MSs are, but we do not know their trajectory (i.e., no horizon).

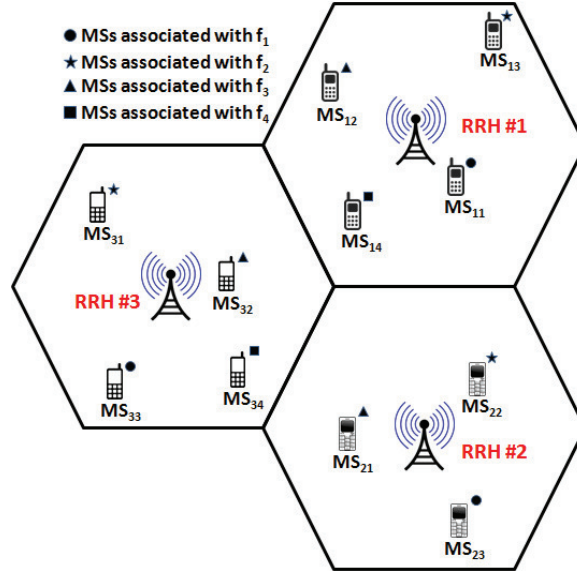


Figure 3.4: Example for allocating frequency channels to the MS's.

With these realistic working assumptions, we propose *Channel-Select*, an algorithm to allocate the frequency channels to the MSs in such a way that $D(\mathbf{A}_l)$'s become as low as possible. Figure 3.4 clarifies our explanations for the case when the cluster size M is 3 and the number of channels L is 4. Firstly, based on the location of the MSs, we calculate the distances between the MSs and RRHs. Then, we define how many MSs should be allocated to each frequency channel as $N = \lceil K/L \rceil$ (as in Fig. 3.4, where $K = 11$, $L = 4$, and $N = 3$). Furthermore, we find the nearest MS in cell #1 (MS_{11}) and $N - 1$ farthest MSs in the other cells (MS_{23} and MS_{33}) to the RRH #1 and allocate channel f_1 to this group of MSs. We repeat this procedure for the remaining cells and MSs until when all the MSs have been allocated a channel. Algorithm 1 presents the pseudo-code of our *Channel-Select* allocation strategy: here, lines 6 and 8 make the diagonal and non-diagonal component of matrix \mathbf{A} , respectively, higher and lower, which forces the maximum $D(\mathbf{A}_l)$ to be as small as possible, as required by the objective function in (3.5). Figure 3.5 compares our *Channel-Select* strategy with random select and optimal solution for different number of MS's. As we expect,

for a large number of MSs the possible combination of MSs increases and, as a result, the average $D(\mathbf{A})$ of our *Channel-Select* strategy and optimal solution decreases. So, unlike in random select, *Channel-Select* is able to increase the SNR (by decreasing the negative effect of background noise) of estimated source signals by exploiting diagonal dominant mixing channel coefficient matrices. From Fig. 3.2, we see that the difference between *Channel-Select* and optimal is not significant as the increase in BER is in order of 10^{-4} .

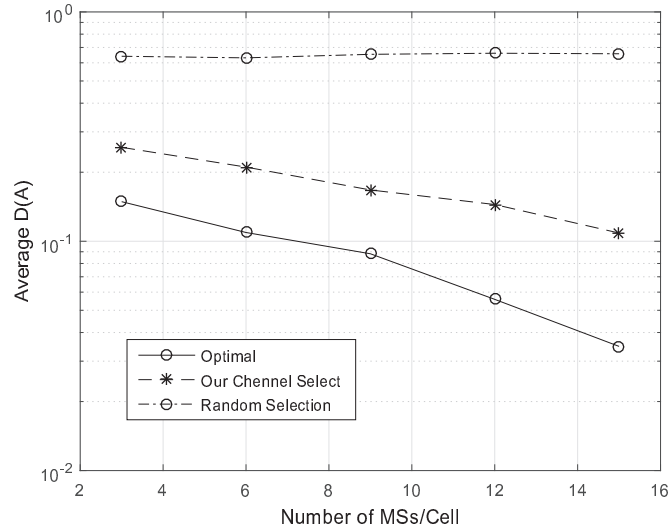


Figure 3.5: *Channel-Select* vs. optimal solution (by exhaustive search) for small problem sizes (cluster size $M = 3$).

It should be mentioned that our solution, *Cloud-BSS*, is transparent to the MSs. The only over-the-air signaling that it requires is the one for conveying the channel allocation decision (made by *Channel-Select*) to the MSs; and this uplink-channel-allocation signaling is already part of current as well as next-generation OFDMA-based cellular systems.

3.3.3 Cluster Size and Computational Complexity

One of the main requisites for LTE is the requirement of very low level of latency. So, it is necessary to explore the computational complexity and run time of our *Cloud-BSS* solution for different cluster sizes. The cluster size dictates the computational complexity and the accuracy of the ICA methods, where the former depends on the no. of sources (N), no. of mixtures (M), no. of data samples (T),

Algorithm 1 *Channel-Select Strategy*

Input: L = Total number of frequency channels available, M = Number of cells in a cluster

Output: MS_l = Set of MSs associated with the l^{th} channel

Description:

```

1: for  $l = 1; l \leq L; l++$  do
2:    $t = 1; K = l \bmod M;$ 
3:   if  $K = 0$  then
4:      $K = M;$ 
5:   end if
6:    $MS_l(t)$  = Find in cell # $K$  the nearest MS to RRH # $K$ ;
7:   for  $j = 1 : M$  &&  $j \neq K$  do
8:      $MS_l(++t)$  = Find in cell # $j$  the farthest MS to RRH # $K$ ;
9:   end for
10:  Among  $MS_l(2 : L)$  keep the  $N - 1$  farthest MSs and remove the others, reducing the size of
     $MS_l$  from  $M$  to  $N$ ;
11:  Allocate  $f_l$  to the remaining  $MS_l$ s;
12:  if All MSs have been allocated with a channel then
13:    return;
14:  end if
15: end for

```

no. of iterations (Q), and no. of sweeps²(I). As the cluster size, i.e., the no. of RRHs (mixtures) and MS signals (sources), increase the computational complexity increases. The computational complexity of an algorithm is measured by the required floating point operations (flops) to execute it, where a flop corresponds to a multiplication followed by an addition.

Here, we briefly compare the complexity and accuracy of three well-known complex-valued ICA algorithms: JADE [55], Complex ICA-EBM [56], and Complex FastICA [57]. Complex ICA-EBM adopts a line-search optimization procedure using a projected conjugate gradient, while Complex FastICA finds independent components by separately maximizing the negentropy of each mixture. To compare the separation quality of these algorithms, we use the Performance Index (PI), which measures the difference between the mixing and estimated separating matrix, defined as,

$$PI = \sum_{i=1}^N \left[\left(\sum_{k=1}^N \frac{|p_{ik}|^2}{\max_j |p_{ij}|^2} - 1 \right) + \left(\sum_{k=1}^N \frac{|p_{ki}|^2}{\max_j |p_{ji}|^2} - 1 \right) \right], \quad (3.6)$$

where p_{ij} is the $(i, j)^{th}$ element of the matrix $\mathbf{P} = \mathbf{BA}$, and $\max_j |p_{ij}|$ and $\max_j |p_{ji}|$ are the maximum absolute value in the i^{th} row and column of matrix \mathbf{P} , respectively. As the PI increases,

²A sweep is an iteration process over all principal 2×2 submatrices.

the difference between \mathbf{B} and \mathbf{A}^{-1} increases, so the separation quality is correspondingly poorer. If the separation is perfect, then the separating matrix is the inverse of the mixing matrix and the PI is zero. Table 3.1 lists the computational complexity, separation quality, and run time³ of the aforementioned ICA algorithmic methods for different numbers of data samples T . As we can see, the PI decreases as T increases from 2000 to 8000, although at the price of the Run Time (RT): this is because with more data samples more information about the statistics of the mixtures is available, which enables the ICA algorithms to estimate the separating matrix more accurately. From Table 3.1 it is clear that the execution time of our *Cloud-BSS* solution using JADE algorithm is in order of millisecond, which is feasible in LTE systems.

Table 3.1: Computational Complexity, Run Time (RT), and Performance Index (PI) of three competing ICA methods for five parameters: N = no. of sources, M = no. of mixtures, T = no. of data samples, Q = no. of iterations, and I = no. of executed sweep; in the simulations, we considered $N = M = 5$.

Method	Computational Complexity (flops)	T=2000		T=4000		T=8000	
		RT [s]	PI	RT [s]	PI	RT [s]	PI
JADE [55]	$\min\{TM^2/2+4M^3/3+NMT, 2KM^2\} + 3TN(N+1)(N^2+N+2)/8 + TN^2 + \min(4N^6/3, 8N^3(N^2+3)) + IN(N-1)(75+21N+4N^2)/2$	0.03445	7.08145	0.04657	2.10674	0.07535	0.43901
Complex ICA-EBM [56]	$\min\{TM^2/2+4M^3/3+NMT, 2TM^2\} + 4M^3/3 + (Q-1)M^3/2 + IN(N-1)(17(M^2-1)+75+4N+4N(M^2-1))/2$	1.05756	8.07938	1.50168	2.13367	1.69157	0.35794
Complex FastICA [57]	$\min\{TM^2/2+4M^3/3+NMT, 2TM^2\} + (2(N-1)(N+T) + 5TN(N+1)/2)K$	0.45037	9.33160	0.75995	5.77939	1.38608	1.78655

Moreover, Fig. 3.6 shows the increase in RT (left y-axis) and PI (right y-axis) with the increase in the number of sources and mixtures (here $N = M$). To sum up, increasing the cluster size leads to higher computational complexity and lower accuracy; however, it also brings a few advantages, which we study in the following section, calling for finding the right trade-off.

3.4 Other Benefits of our Proposed Cloud-BSS

Besides improving the system spectral efficiency, using BSS within C-RAN brings several other advantages, some of which are briefly discussed below.

³The experiments were performed on an Intel Core2 Quad CPU 2.4-GHz PC with 8 GB of RAM.

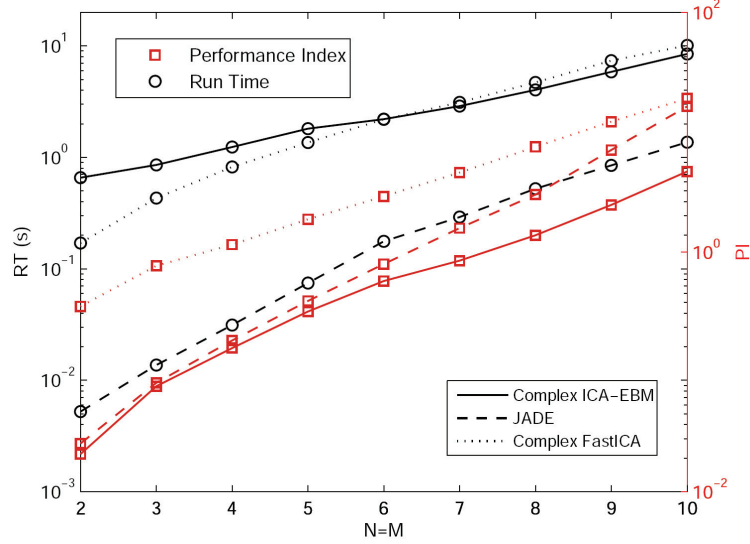


Figure 3.6: Increase in Run Time (RT) and Performance Index (PI) of the three ICA algorithms with increase in the no. of sources and mixtures (here $T=8000$). The left y-axis reports the RT in seconds, while the right y-axis reports the PI as in (3.6).

Table 3.2: Reduction of handovers by clustering the cells using our BSS-based solution; cell radius = 1 km, simulation area = 30×30 km², $s_{min} = 0$, $s_{max} = 30$ m/s, simulation time = 1 hr, no. of MSs = 1000, $\bar{d} = \pi$, $\bar{s} = 15$ m/s, $d_{x_{n-1}} \sim \mathcal{N}(\pi, 1)$, $s_{x_{n-1}} \sim \mathcal{N}(15, 3)$, no. of simulations = 100.

Mobility Model	Number of Handovers			
	Without Clustering	Cells/Cluster = 3	Cells/Cluster = 4	Cells/Cluster = 5
Random Waypoint	$5716 \pm 5\%$	$2318 \pm 4\%$	$1268 \pm 5\%$	$843 \pm 6\%$
Gauss-Markov	$3673 \pm 0.6\%$	$1682 \pm 1.1\%$	$711 \pm 2.3\%$	$457 \pm 2.9\%$

3.4.1 Fewer Handovers

As long as the active users stay in the same cluster, there is no need to perform costly handovers because when a MS moves from one cell to another all the RRHs within the cluster are still able to receive the mixtures of the transmitted signals. The number of handovers can be further reduced by increasing the size of the clusters. However, with an increase in both N and M , the complexity of the ICA methods and of the frequency-allocation algorithm, as well as the noise level in the estimated sources, will also increase.

To show the performance of our proposed solution in terms of number of handover sessions, we consider two mobility models: 1) Random Waypoint and 2) Gauss-Markov [59]. In the first model, a MS moves from its current location to a new one by choosing randomly a direction d [rd] and a speed s [m/s] from pre-defined ranges, e.g., $[0, 2\pi]$ and $[s_{min}, s_{max}]$, respectively. After choosing

these parameters, a MS moves to its new location by traveling for a certain time or distance. The model also includes pause time between changes in direction and speed. The second mobility model is designed to adapt to different levels of randomness by means of a tuning parameter: the direction and speed at the n^{th} step are calculated based on those at the $(n-1)^{th}$ step and on a random variable, as,

$$\begin{aligned} d_n &= \alpha d_{n-1} + (1 - \alpha)\bar{d} + \sqrt{(1 - \alpha^2)}d_{x_{n-1}} \\ s_n &= \alpha s_{n-1} + (1 - \alpha)\bar{s} + \sqrt{(1 - \alpha^2)}s_{x_{n-1}}, \end{aligned} \quad (3.7)$$

where d_n and s_n are the new direction and speed for the n^{th} step, α ($0 \leq \alpha \leq 1$) is the tuning parameter to vary the randomness, \bar{d} and \bar{s} are constants representing the mean value of direction and speed as $n \rightarrow \infty$, and $d_{x_{n-1}}$ and $s_{x_{n-1}}$ are random variables from a Gaussian distribution.

Table 3.2 represents the reduction in the number of handover sessions using *Cloud-BSS*. In the simulations, we performed an handover to the neighboring cell/cluster if both of the following conditions are met [60]: **(1)** If the signal strength from the neighboring cell/cluster exceeds that of the serving cell/cluster by an hysteresis (i.e., margin) level of at least 1 dB; **(2)** If the distance from the serving cell/cluster exceeds that of the neighboring cell/cluster by more than 1.1 km. It is clear that the number of handover sessions decreases with the increase of the cluster size. However, as we show in Figs. 3.2 and 3.6, the complexity of the ICA algorithms and the noise level of the estimated MS signals also increase.

Furthermore, we show how robust our solution is in terms of mobility and handover. As we observed previously, the achievable BER is highly dependent on the topology; so, in order to improve the BER performance, we introduced *Channel-Select*, a frequency-channel allocation heuristic. Now, we study how robust our solution is under user mobility without considering *Channel-Select*. To do this, we consider clusters of four cells (cell radius = 3 km), as shown in Fig. 3.7, and study four cases: in the first, all the MSs are in different cells while in the forth all the MS's have moved into cell #2. As we can see, in the first case, the topology is diagonal dominant and we expect an acceptable BER. However, from case #1 to case #4, $D(\mathbf{A})$ increases and we expect a decrease in the BER performance. Figure 3.8 shows the BER performance for these four cases, which corroborates our analysis.

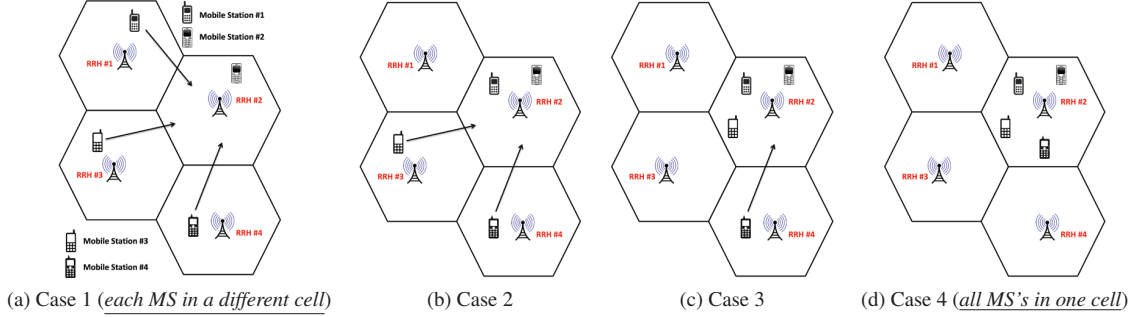


Figure 3.7: Four cases of mobile network in which all the MS's are using the same frequency channel.

3.4.2 Increased Reliability

We can trade capacity for improved BER performance. As mentioned earlier, we can assign each frequency channel to a maximum of as many as the total number of RRHs (recall that ICA algorithms require the no. of mixtures to be equal or greater than the no. of sources, i.e., $M \geq N$). The relationship between the *Net Channel Capacity* C_n of our proposed *Cloud-BSS* solution and the no. of admitted MSs N per frequency channel is,

$$C_n = N \cdot C_{ch} \cdot [1 - BER(N)], \quad (3.8)$$

where C_{ch} is the capacity of the frequency channel and $BER(N)$ indicates that the BER depends on N , as studied in Fig. 3.2. Figure 3.9 shows the increase of the net channel capacity with respect to the number of admitted MS's for the SNR ranging in $[5, 20]$ dB and $D(\mathbf{A}) = 0.3$.

When the capacity is not the key issue, we can improve the BER by not using all the potential capacity of the network, i.e., by allocating each channel to fewer MSs so to induce diagonally dominant mixing matrices. This would lead to the reduction of the columns of matrix \mathbf{A} and to a higher degree of freedom in making the mixing matrix diagonally dominant. To illustrate this intuition, we consider Topology 2 in Fig. 3.1(b), which is not diagonally dominant. However, we can make it so by allocating the channel to only two users instead of three, e.g., we can either remove MS #2 or MS #3. Figure 3.10 shows the BER performance in such scenario: interestingly, by removing MS #3 the performance is better than removing MS #2 as we obtain a lower $D(\mathbf{A})$, leading to a lower BER.

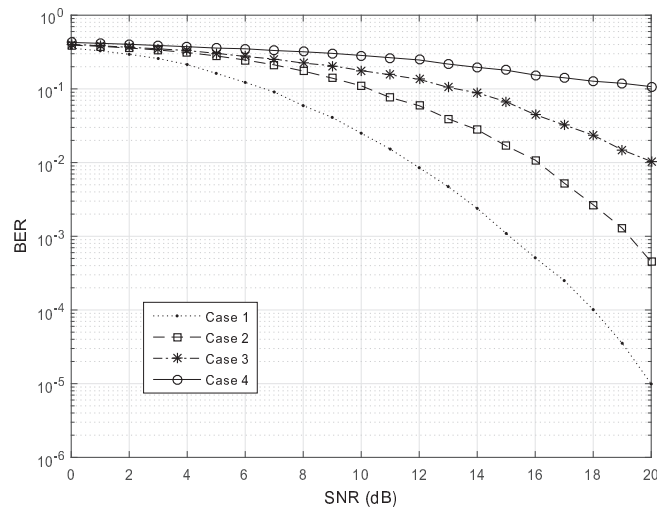


Figure 3.8: Increase of BER by moving the MS's towards a common cell.

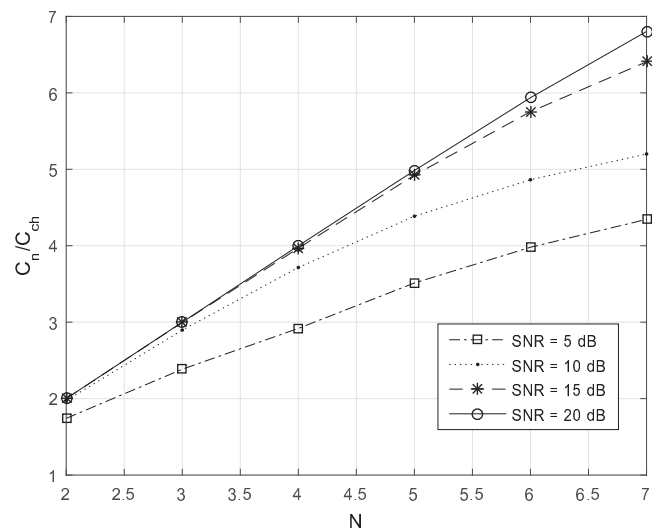


Figure 3.9: Increase in the Net Channel Capacity with increase in N , with $M = 7$, for different $SNR = 5, 10, 15, 20$ dB and $D(\mathbf{A}) = 0.3$.

3.4.3 Interference Cancellation

Due to the orthogonality of subcarriers in LTE systems, the MSs have immunity to intra-cell interference. However, cell-edge users are known to face large ICI, especially, in a highly-loaded cellular environment. In *Cloud-BSS*, as BSS deals with mixed signals, intra-cluster interference is not a concern as it is a part of the received mixed signals and, as such, the ICA algorithms take care of it when separating the sources. Hence, there is no need for the BSs to go through costly inter-BS message

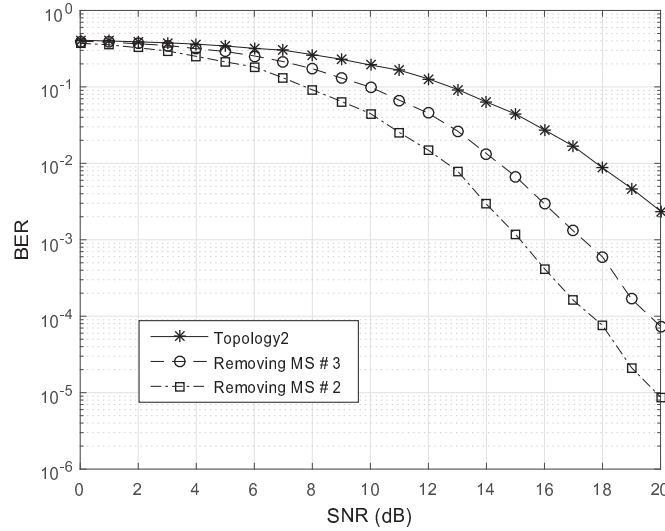


Figure 3.10: Trading off capacity for improved BER: decrease of BER with SNR when removing MS # 2 or MS # 3 from Fig. 3.1(b).

exchange to execute coordinated interference cancelation. In fact, by applying the ICA algorithm to the received signals in a cluster, harmful interference can be turned into useful signal, which boosts performance by transforming a ‘foe’ into a ‘friend’. Moreover, the *Channel-Select* strategy decreases the defective impact of inter-cluster interference (background noise) on the estimated signals by exploiting the diagonal dominant mixing channel coefficient matrices. With the increase in the cluster size, the average Signal to Interference plus Noise Ratio (SINR) also increases, which allows the cellular network to enjoy great spectral efficiency enhancement. Table 3.3 represents the improvement of spectral efficiency and throughput using *Cloud-BSS*. With a cluster size equal to 5, *Cloud-BSS* enhances the uplink average cell user and cell-edge user throughput by 49% and 93%, respectively.

Table 3.3: Comparison of uplink Spectral Efficiency (SE) and Throughput (R) between non-cooperative traditional systems and *Cloud-BSS* (cell radius = 1 km).

Method	Average Cell User		Cell Edge User	
	SE [bps/Hz]	R [Mbps]	SE [bps/Hz]	R [Mbps]
Traditional System (Non-Cooperative)	$2.17 \pm 7.3\%$	10.85	$0.73 \pm 6.8\%$	3.65
<i>Cloud-BSS</i> ($M = 3$)	$2.76 \pm 6.8\%$	13.79	$1.12 \pm 6.2\%$	5.60
<i>Cloud-BSS</i> ($M = 4$)	$3.07 \pm 7.1\%$	15.35	$1.27 \pm 6.3\%$	6.35
<i>Cloud-BSS</i> ($M = 5$)	$3.23 \pm 7.1\%$	16.14	$1.41 \pm 7.8\%$	7.05

3.4.4 No Additional Overhead Compared to CoMP

CoMP is another approach to mitigate the average interference, in which the BSs within a cluster exchange CSI [61]. However, this approach requires a pilot-symbol overhead in order to estimate the channel coefficients [62]. Releasing this huge amount of capacity can increase the net bit rate, which may be used for other purposes like coding to increase reliability. Our BSS-based solution implicitly estimates the channel coefficients and therefore does not require pilot-data exchange as in CoMP.

3.5 Discussion

There are quite a few blind techniques which is applied in wireless communication [63]. In this chapter, we also presented a novel BSS-based solution, *Cloud-BSS*, that leverages the centralized characteristic of C-RAN so to improve performance of highly mobile cellular networks. Cloud-BSS divides a set of neighboring cells into clusters that can use all of the frequency channels in the system band, thus increasing the system spectral efficiency, decreasing handovers, and eliminating the need for bandwidth-consuming channel estimation while mitigating interference. We discussed the effect of irregular topologies on Cloud-BSS performance in terms of BER and introduced a strategy, named *Channel-Select*, to improve the SNR.

Chapter 4

Dynamic Joint Processing for Interference Cancellation in C-RAN

4.1 Overview

The Coordinated Multi-Point (CoMP) transmission and reception technique, which is based on cooperative MIMO, is one of the major methods to mitigate the average interference and increase the spectral efficiency at the cost, however, of increased receiver complexity [61]. In CoMP, a set of neighboring cells are divided into *clusters*; within each cluster, a *fixed* set of BSs are connected to each other via the BPU and exchange CSI as well as MS signals (see Fig. 4.1). Coordination of the BSs within a cluster can improve the overall SINR. In the uplink, each BS receives a combination of MS signals from its own and from the other neighboring cells (see Fig. 4.2). By combining the CSI from different cells and sharing the received signals at the BPU, CoMP is thus able to cancel the intra-cluster interference.

Although CoMP is able to reject the intra-cluster interference, it cannot mitigate the inter-cluster interference [64, 65]; hence, cluster-edge MSs can produce an intensive inter-cluster interference at the neighbouring external BSs (see Fig. 4.2). Consequently, in cellular networks with a frequency reuse factor equal to 1, the achieved system capacity is still significantly far from the interference-free capacity upper bound. Furthermore, one of the main requisites of 5G systems is the very low level of latency: *the additional processing required for multiple-site reception/transmission and CSI acquisition as well as the communication incurring among different BSs add delay significantly and limit the cluster size (especially for massive MIMO)*. Moreover, BSs' clocks need to be in phase in order to enable proper operation of CoMP. This requires a highly accurate phase or time-of-day synchronization. To overcome these challenges, the BSs should be connected together in a form of centralized RAN. Therefore, novel architecture and algorithms is necessary for the next generation of wireless cellular network to overcome the aforementioned challenges and achieve the ambitious data rate.

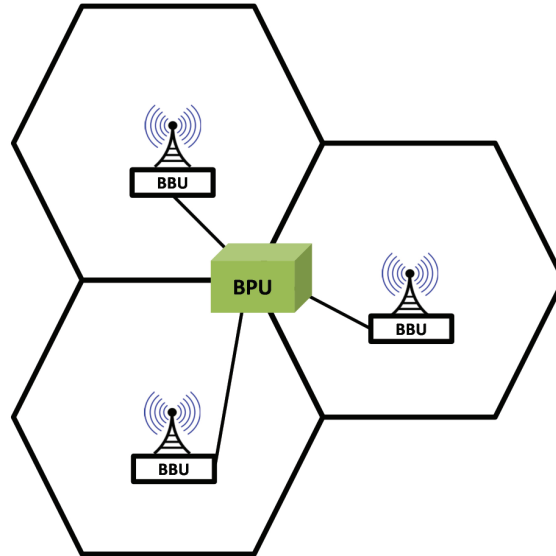


Figure 4.1: Data exchange within a cluster in Coordinated Multi-Point (CoMP) transmission and reception.

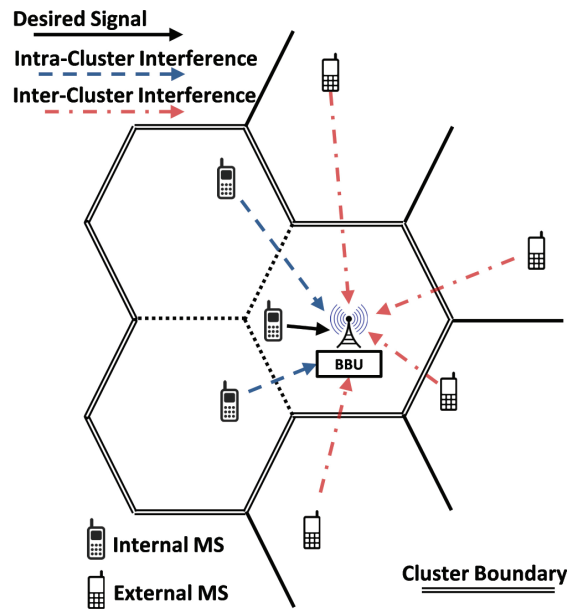


Figure 4.2: Intra- and inter-cluster uplink interference (we name the MS (BS) inside the cluster as *internal* and outside the cluster as *external MS (BS)*).

In this chapter, we leverage the C-RAN architecture to exploit fully the potential of CoMP so to suppress the ICI and increase spectral efficiency. Specifically, we propose a novel uplink clustering scheme, called *Dynamic Joint Processing (DJP)*, which decreases *both* the intra- and inter-cluster

interference without increasing the size of clusters [7]. Firstly, we introduce the idea of “VBS-Cluster”, in which we merge VBSs serving a cluster into a unit VBS-Cluster while the RRHs’ antennae in each cluster act as a single coherent antenna array distributed over the cluster region, and briefly talk about its advantages. Then, in the proposed solution, we divide the MSs into two categories based on their average velocity: 1) low-mobility and 2) high-mobility MSs. Based on the mobility level of the MSs, we present two different coexisting clustering approaches and propose to exploit their complementary advantages simultaneously.

4.2 System Model and Challenges

To understand better our solution, we formulate the problem and detail the issues with CoMP. Moreover, with a simple case study, we clarify why the omni-subband clustering is unable to address the current cellular network challenges and explain why the clustering of the RRHs must be studied jointly with spectrum allocation.

4.2.1 System Description

Consider a CoMP uplink system with frequency reuse factor equal to 1. In CoMP, a set of neighboring cells is divided into clusters, and in each cluster the BSs coordinate with each other in order to reject the intra-cluster interference. Let $\mathcal{L} = \{1, \dots, L\}$ be the set of all BSs, $\mathcal{U} = \{1, \dots, U\}$ be the set of all MSs, and $\mathcal{J} = \{1, \dots, J\}$ be the set of all clusters. We assume that the frequency band is divided into a set of subbands $\mathcal{F} = \{f_1, \dots, f_K\}$ (K is the total number of subbands) and each active MS is allocated with one subband. Each cluster consists of a set of BSs $\mathcal{M}_j = \{1, \dots, M_j\}$, where $\sum_{j=1}^J M_j = L$. Also, depending on the spectrum resource allocation, in each cluster there is a set of active MSs $\mathcal{N}_j^{(k)} = \{1, \dots, N_j^{(k)}\}$ allocated with the k^{th} subband, where $N_j^{(k)} \leq M_j$ and $\sum_{k=1}^K \sum_{j=1}^J N_j^{(k)} = U$. In this chapter, $\mathcal{N}_j^{(k)}(i)$ refers to the i^{th} MS in the set $\mathcal{N}_j^{(k)}$. Let also $\mathbf{P}_j^{(k)} = [P_j^1, \dots, P_j^{N_j^{(k)}}]$ be the $N_j^{(k)} \times 1$ vector of transmission power of the set $\mathcal{N}_j^{(k)}$. For the k^{th} subband, the relationship between the received signals by internal BSs¹ of the set \mathcal{M}_j (BSs of the j^{th} cluster) and the transmitted MS signals at different time instants can be expressed through the

¹We name the MS (BS) inside the cluster as *internal* and outside the cluster as *external* MS (BS).

following linear noisy model,

$$\begin{aligned} \mathbf{y}_j^{(k)} &= \sum_{l \in \mathcal{N}_j^{(k)}} s_j^{(k)}(l) \mathbf{h}_{jj}^{(k)}(l) + \sum_{q \in \mathcal{J}, q \neq j} \sum_{r \in \mathcal{N}_q^{(k)}} s_q^{(k)}(r) \mathbf{h}_{qj}^{(k)}(r) + \mathbf{n}_j^{(k)} \\ &= \mathbf{H}_{jj}^{(k)} \mathbf{s}_j^{(k)} + \sum_{q \in \mathcal{J}, q \neq j} \mathbf{H}_{qj}^{(k)} \mathbf{s}_q^{(k)} + \mathbf{n}_j^{(k)}, \end{aligned} \quad (4.1)$$

where, for clarity, the time variable t is omitted. Here, $\mathbf{s}_j^{(k)} = [s_j^{(k)}(1), \dots, s_j^{(k)}(N_j^{(k)})]^T$ is the $N_j^{(k)} \times 1$ vector of MS signals of the j^{th} cluster operating over the k^{th} subband, $\mathbf{h}_{qj}^{(k)}(r)$ is $M_j \times 1$ vector of channel coefficients between the MS $\mathcal{N}_q^{(k)}(r)$ and BSs of the set \mathcal{M}_j , $\mathbf{H}_{qj}^{(k)}$ is the $M_j \times N_q^{(k)}$ channel coefficients between the MSs of the set $\mathcal{N}_q^{(k)}$ and BSs of the set \mathcal{M}_j , $\mathbf{y}_j^{(k)} = [y_j^{(k)}(1), \dots, y_j^{(k)}(M_j)]^T$ is the $M_j \times 1$ vector of received signals by the internal BSs, and $\mathbf{n}_j^{(k)} = [n_j^{(k)}(1), \dots, n_j^{(k)}(M_j)]^T$ is the $M_j \times 1$ vector of Additive White Gaussian Noise (AWGN).

Although in each cluster the BSs receive a combination of internal and external MS signals (see Fig. 4.2), *CoMP is only able to cancel the intra-cluster interference (caused by internal MSs from neighbouring cells)*. A simple form of coordination is achieved by employing a Zero-Forcing (ZF) receiver. In the ZF receiver (for the uplink), since the CSI from all the internal BSs in a cluster is available through the BPU, we can form the equalizer as,

$$\mathbf{G}_j^{(k)} = \left(\left(\mathbf{H}_{jj}^{(k)} \right)^\dagger \mathbf{H}_{jj}^{(k)} \right)^{-1} \left(\mathbf{H}_{jj}^{(k)} \right)^\dagger. \quad (4.2)$$

By multiplying the equalizer to the vector of received signal, the output of the ZF receiver is given by,

$$\hat{\mathbf{s}}_j^{(k)} = \mathbf{G}_j^{(k)} \mathbf{y}_j^{(k)} = \mathbf{s}_j^{(k)} + \mathbf{w}_j^{(k)}, \quad (4.3)$$

where

$$\mathbf{w}_j^{(k)} = \underbrace{\sum_{q \in \mathcal{J}, q \neq j} \mathbf{G}_j^{(k)} \mathbf{H}_{qj}^{(k)} \mathbf{s}_q^{(k)}}_{\text{Inter-Cluster Interference}} + \underbrace{\mathbf{G}_j^{(k)} \mathbf{n}_j^{(k)}}_{\text{AWGN}}. \quad (4.4)$$

From (4.3) and (4.4), the SINR and data rate of $\mathcal{N}_j^{(k)}(i)$ is,

$$\gamma_{ij}^{(k)} = \frac{P_j^{(k)}(i) \left| \mathbf{g}_j^{(k)}(i) \mathbf{h}_{jj}^{(k)}(i) \right|^2}{N_0 \Delta B^{(k)} + \sum_{q \in \mathcal{J}, q \neq j} \sum_{r \in \mathcal{N}_q^{(k)}} P_q^{(k)}(r) \left| \mathbf{g}_j^{(k)}(i) \mathbf{h}_{qj}^{(k)}(r) \right|^2}, \quad (4.5)$$

$$R_{ij}^{(k)} = \Delta B^{(k)} \log_2 \left(1 + \gamma_{ij}^{(k)} \right), \quad (4.6)$$

where $\mathbf{g}_j^{(k)}(i)$ is the i^{th} row of the equalizer matrix $\mathbf{G}_j^{(k)}$, $\mathbf{h}_{qj}^{(k)}(r)$ is the r^{th} column of $\mathbf{H}_{qj}^{(k)}$, N_0 is the white noise power spectral density, and $\Delta B^{(k)}$ is the bandwidth of k^{th} subband. It is clear from (4.13) that *the interference generated by the external cluster-edge MSs dramatically decreases the SINR and data rate.*

4.2.2 Problem Statement

The objective is to find the optimal clustering decision and transmission power so as to maximize the sum rate while meeting a set of predefined constraints, as follows.

$$\mathbf{p} : \underset{\left\{ M_j, P_j^{(k)} \right\}_{j \in J}}{\operatorname{argmax}} \quad \sum_{k \in F} \sum_{j \in J} \sum_{i \in N_j^{(k)}} R_{ij}^{(k)} \quad (4.7a)$$

$$\text{subject to} \quad P_j^{(k)}(i) \leq P_{\max}, \quad (4.7b)$$

$$R_0 \leq R_{ij}^{(k)}, \quad (4.7c)$$

$$M_j \leq M_0. \quad (4.7d)$$

Constraint (6.12b) indicates that the MS transmission power cannot exceed the maximum allowed transmission power. Constraint (6.12c) guarantees a minimum per-user data rate and constraint (4.7d) specifies the maximum cluster size. Here, with a simple case study we explain why this optimization problem is NP-hard and cannot be solved under realistic constraints. More specifically, we show that for different spectrum allocation scenarios the clustering problem changes.

4.2.3 Case Study

Here, we explain the motivation of the proposed solution and the necessity of studying clustering and spectrum allocation jointly. For this purpose, with a simple example we explain that i) how spectrum allocation can affect the clustering problem, ii) why fixed clustering in any condition cannot solve the inter-cluster interference problem, iii) why even dynamic clustering does not work, and iv) why the clustering problem is NP-hard. As shown in the Fig. 4.3(a), consider a network of

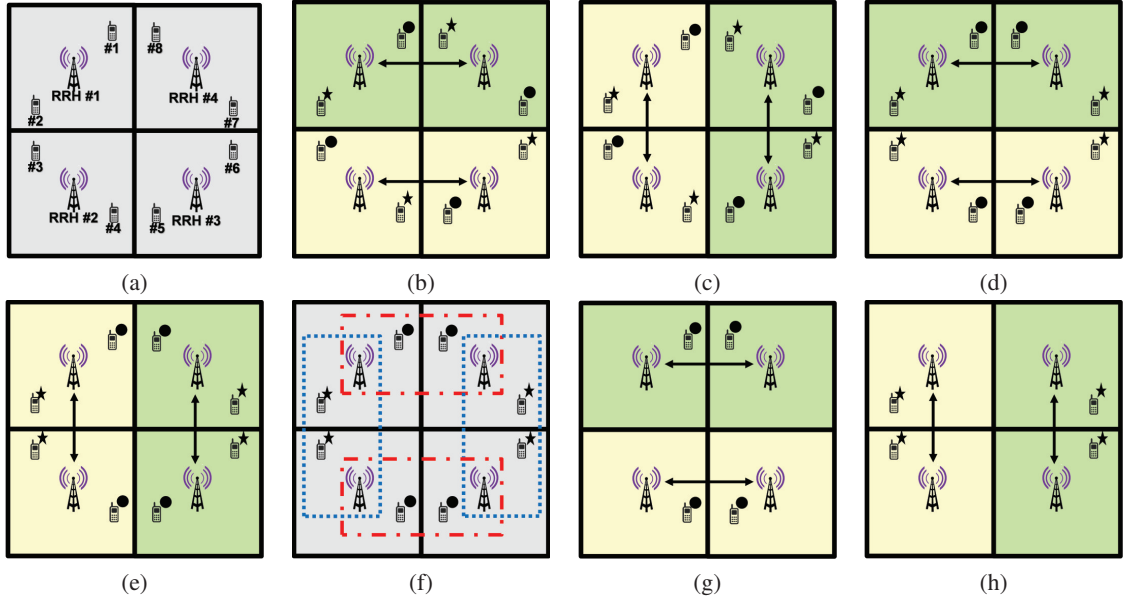


Figure 4.3: Case study to show the issues with traditional CoMP: (a) Network of 4 cells where each cell has 2 MSs to serve; (b) and (c) Horizontal and vertical omni-subband clustering for the first scenario of spectrum allocation; (d) and (e) Horizontal and vertical omni-subband clustering for the second scenario of spectrum allocation; (f) Uni-subband clustering for the second scenario of spectrum allocation; (g) Virtual uni-subband clusters for subband #1; (h) Virtual uni-subband clusters for subband #2.

4 cells and 8 MSs working under the traditional CoMP where each cell has 2 MSs to serve. Also, assume that there are 2 frequency subbands (f_1 and f_2) to allocate to the MSs and cluster size cannot be greater than 2 (due to the delay and complexity constraints). Depending on which subband is allocated to which MS there are 16 different scenarios for spectrum allocation. In this case study, we will focus on 2 of these scenarios.

Figures 4.3(b) and 4.3(c) show our first scenario of spectrum allocation where MSs #1, #3, #5, #7 (circled MSs) are allocated with f_1 and MSs #2, #4, #6, #8 (stared MSs) are allocated with f_2 . Note that in the figures we have used circle and star to distinguish between the MSs allocated with f_1 and the MSs allocated with f_2 , respectively. In this case, in traditional CoMP if we form clusters horizontally, as shown in Fig. 4.3(b) where different clusters are associated with different colors, the MSs #2 and #7 become cluster-edge MSs in the green colored cluster and have a destructive inter-cluster interference on the yellow colored cluster. Likewise, MSs #3 and #6 become the cluster-edge MSs in the yellow colored cluster and have a destructive inter-cluster interference on the green colored cluster. Now, if we form the clusters vertically, as shown in Fig. 4.3(c), MSs #1, #4, #5, #8 become cluster-edge MSs and have destructive inter-cluster interference on their neighboring

clusters.

Now, let us consider a second scenario of spectrum allocation, as shown in Figs. 4.3(d) and 4.3(e), where MSs #1, #4, #5, #8 are allocated with f_1 and MSs #2, #3, #6, #7 are allocated with f_2 . Note that in the second scenario, we only have changed the order of spectrum allocation in cells #2 and #4 compare to the first scenario. In this case, if we form the clusters horizontally, as shown in Fig. 4.3(d), the performance of subband f_1 becomes very good. This is because for subband f_1 there is no cluster-edge MS and due to the path loss the inter-cluster interference is very low. However, all the MSs performing on subband f_2 become cluster-edge MSs and have a destructive inter-cluster interference on the neighboring external cells. For instance, RRHs #2 and #3 receive a strong inter-cluster interference from MSs #2 and #7, respectively. Likewise, if we form the clusters vertically, as shown in Fig. 4.3(e), all the MSs performing on sub-band f_1 become cluster-edge MSs while there is no cluster-edge MS operating over subband f_2 .

As we discussed above, based on the spectrum allocation the clustering problem changes. In other words, the performance of the clustering highly depends on the spectrum allocation and this is why we should study the clustering and spectrum allocation jointly. Moreover, with static clustering we always have cluster-edge MSs. In traditional CoMP, since all the spectrum is used in each cluster, even with dynamic clustering we cannot solve the inter-cluster interference problem and there will be always some MSs located on the edge of clusters. This is because traditional CoMP only changes the boundaries of interference from cell to cluster. *So, to really find the optimal clustering decision, we need to consider all the spectrum allocation scenarios and find the optimal clustering decision for each subband separately.* For instance, in a network with M cells and K subbands, where we have $(K!)^M$ scenarios for spectrum allocation, we need to solve $K(K!)^M$ optimization problems to find the optimal clustering decision. This makes the clustering problem NP-hard, which is why finding the optimal solution under real-world timing constraints is infeasible. In the following section, we discuss Figs. 4.3(f-h) and explain how uni-subband clustering can solve the aforementioned problem.

4.3 Proposed Solution

In C-RAN, all the VBSs of a large region are centralized in a common datacenter. This centralized characteristic along with real-time virtualization technology provides an extra degree of freedom that is useful to mitigate both the intra-cluster as well as inter-cluster interference. In addition, all the VBSs can communicate and exchange data with each other at Gbps speeds. Unlike in traditional CoMP where each cell is only associated *statically* with a certain cluster, in C-RAN we are able to associate each cell with different clusters and dynamically add/remove cells to/from a certain cluster. Here, we focus on clustering problem and leverage these properties to form *virtual clusters* and *hybrid cells* so to mitigate the intra- and inter-cluster interference and boost the system spectral efficiency and data rate.

It is expected that 5G will be able to handle about 1000 times more mobile data than today's cellular systems and that it will become the backbone of the Internet of Things (IoT) linking up fixed and mobile devices. Since the speed of the MSs leads to different conditions to the system, we need to differentiate the high-mobility from the low-mobility MSs in order to provide better QoS. So, in our solution, named *Dynamic Joint Processing (DJP)*, we introduce two *coexisting* clustering approaches (for different mobility levels). In both approaches the frequency reuse factor is equal to 1 and we use all the frequency band in the cells. In the first approach (for low-mobility MSs with average velocity less than V_{th}), we propose to form *virtual uni-subband clusters* and dynamically change the cluster size based on the position of the MSs. In the second approach (for high-mobility MSs with average velocity greater than V_{th}), we divide each cell into 3 sectors and merge 3 neighboring sectors from different cells to form a *hybrid cell*. Moreover, in order to avoid the inter-cluster interference, we assign a different set of subbands to different hybrid cells.

Since one of the main applications of 5G is autonomous cars and intelligent transportation, we consider high-mobility scenario for MSs with a speed greater than the maximum walking speed. Hence, in our simulations we use $V_{th} = 5$ m/s (maximum walking/running speed) as the threshold between high-mobility (driving) and low-mobility (walking or stationary) speed. In the following sections, we detail these two approaches, study their pros and cons, and explain how we exploit their complementary advantages *simultaneously*.

4.3.1 Virtual Base Station Cluster

Clustering the neighboring cells in the C-RAN architecture—together with enabling the coordination of the VBSs in the cluster—can improve the system performance by exploiting the extra degrees of freedom so to make optimal decisions. Here, we introduce the idea of *VBS-Cluster*, wherein the VBSs associated with a certain cluster are merged together, and the RRHs' antennae in each cluster act as a single coherent antenna array distributed over the cluster region. Figure 4.4 shows two VBS-Clusters, #1 (on the left) and #2 (on the right), where the sizes of the clusters are 2 and 3, respectively. Since in the C-RAN architecture all the VBSs are collocated in a common place and implemented on VMs, we can dynamically change the size of VBS-Clusters based on the network requirements.

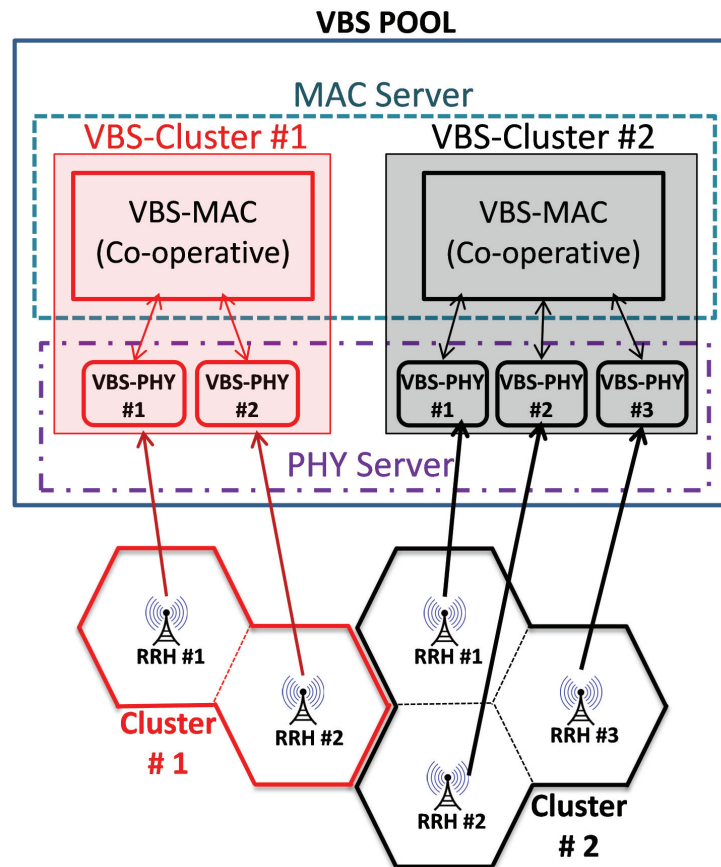


Figure 4.4: Virtual Base Station Cluster (VBS-Cluster): VBSs associated with a cluster are merged together in the VBS-Cluster and RRHs antennae in each cluster act as a single coherent antenna array distributed over the cluster region.

4.3.2 Low-mobility Approach (DJP-LM)

In the first approach, named *DJP-LM*, in order to avoid cluster-edge MSs, for each subband we divide the neighboring cells into *virtual clusters* based on the position of the associated MSs and their distances from the neighboring RRHs. This means that the virtual clusters are defined per subband such that the detrimental impact of inter-cluster interference is minimum. Unlike in the traditional CoMP in which the clusters are “*omni-subband*” (i.e., in each cluster all subbands are used), in the first approach the virtual clusters are “*uni-subband*” (i.e., each cluster only deals with one subband). Consequently, each cell may be involved in different virtual clusters for different subbands.

To clarify the motivation, we use the network of 4 cells described in Sect. 4.2.3. As we discussed in Sect. 4.2.3, with omni-subband clustering there are always cluster-edge MSs that have a destructive inter-cluster interference on the neighboring external RRHs. To address this problem, we propose to form *virtual uni-subband clusters* based on the position of MSs and RRHs. Virtual clustering must be done in such a way that the internal MSs have minimum inter-cluster interference on the neighboring virtual clusters. To do this, we need to measure the received power from each MS to the internal and external RRHs, and decide to change the serving cluster if the interference on external RRH is greater than the interference on internal RRHs.

In Fig. 4.3(f), dot-dash and dotted lines show uni-subband clustering of cell sites associated with subband #1 and #2, respectively. Figures 4.3(f) and (g) also show the uni-subband clusters for subbands #1 and #2, respectively. *From Figs. 4.3(g) and 4.3(g)(h), it is clear that for each subband we have different set of clusters.* For example, cells #1 and #4 form a virtual uni-subband cluster for subband #1 (see Fig. 4.3(g)) and cells #1 and #2 form a virtual uni-subband cluster for subband #2 (Fig. 4.3(h)). *Note that each cell is associated with 2 uni-subband clusters, while in the traditional CoMP each cell is only associated with one omni-subband cluster.* As shown in Figs. 4.3(g) and 4.3(h), with uni-subband clustering there is no cluster-edge MSs and the received power from MSs to external RRHs is very low. This is because with uni-subband clustering, all the internal MSs are as far as possible from the external RRHs and located in the center of the virtual cluster.

Moreover, in *DJP-LM*, the size of virtual clusters is not fixed. In the C-RAN architecture, as the VBS-Clusters are implemented on VMs, we can change the size of clusters based on the MSs’

positions. More accurately, if a MS in the cluster moves such that it becomes a cluster-edge MS we remove the serving cell from the serving virtual cluster and add it to a neighboring virtual cluster in such a way that the MS causes less inter-cluster interference. In *DJP-LM*, we assume that the frequency band is divided into a set of subbands $\mathcal{F} = \{f_1, \dots, f_K\}$ and for each subband the network has a set of virtual uni-subband clusters $\mathcal{J}_{LM}^{(k)} = \{1, \dots, J^{(k)}\}$ ($1 \leq k \leq K$), each virtual cluster consists of a set of RRHs $\mathcal{M}_j^{(k)} = \{1, \dots, M_j^{(k)}\}$ ($1 \leq j \leq J^{(k)}$), and in each virtual cluster there are a set of active MSs $\mathcal{N}_j^{(k)} = \{1, \dots, N_j^{(k)}\}$ ($1 \leq j \leq J^{(k)}$). We measure the received power (in dB) from the MS $n_i^k \in \mathcal{N}_i^{(k)}$ by the RRH $m_l^k \in \mathcal{M}_l^{(k)}$ at time t as,

$$P_{rx}(n_i^k, m_l^k, t) = P_{tx}(n_i^k, t) - PL(n_i^k, m_l^k, t) - P_{fad}(n_i^k, m_l^k, t), \quad (4.8)$$

where $PL(n_i^k, m_l^k, t)$ is the large-scale path loss between the MS n_i^k and the RRH m_l^k at time t , $P_{tx}(n_i^k)$ is the transmitted power of the MS n_i^k , and $P_{fad}(n_i^k, m_l^k, t)$ is the time-varying shadow fading loss. Since CoMP cancels the intra-cluster interference, our goal is to minimize the inter-cluster interference. To do this, we measure the summation of received inter- and intra-cluster interference power from the MS n_i^k to the neighboring and serving clusters,

$$\begin{aligned} P_{ex}(n_i^k, j, t) &= \sum_{\forall m_j^k \in \mathcal{M}_j^{(k)}} P_{rx}(n_i^k, m_j^k, t), \\ P_{in}(n_i^k, i, t) &= \sum_{\forall m_i^k \in \mathcal{M}_i^{(k)}, m_i^k \neq n_i^k} P_{rx}(n_i^k, m_i^k, t), \end{aligned} \quad (4.9)$$

where $P_{ex}(n_i^k, j, t)$ is the received inter-cluster interference from MS n_i^k by the j^{th} virtual cluster and $P_{in}(n_i^k, i, t)$ is the received intra-cluster interference from MS n_i^k by its serving virtual cluster (i^{th} cluster). Then, we find the cluster which receives maximum inter-cluster interference from MS n_i^k and select it as the nominated cluster,

$$P_{j_{max}}(n_i^k, t) = \max_{\substack{1 \leq j \leq J^{(k)} \\ j \neq i}} P_{ex}(n_i^k, j, t), \quad (4.10)$$

where $P_{j_{max}}(n_i^k, t)$ is the maximum inter-cluster interference from MS n_i^k and j_{max} is the index of the nominated cluster to be added to the serving cell in the k^{th} subband at time t . In each iteration, we remove the serving cell from serving cluster and add it to the nominated cluster if $P_{j_{max}}(n_i^k, t)$

exceeds $P_{in}(n_i^k, i, t)$ by a hysteresis threshold thr [dB] (see Algorithm 2).

Algorithm 2 DJP-LM

Input: \mathcal{F}_r = Set of associated subbands to the MS, $K_r = |\mathcal{F}_r|$ = Number of associated subband to the MS, thr = Hysteresis threshold, T = Time between two iterations

Description:

- 1: **for** $k = 1; k \leq K_r; k++$ **do**
 - 2: i = index of serving virtual uni-subband cluster
 - 3: Calculate $P_{in}(n_i^k, i, t)$
 - 4: **for** $j = 1; j \leq J^{(k)}; j++$ **do**
 - 5: Calculate $P_{ex}(n_i^k, j, t)$
 - 6: **end for**
 - 7: Calculate $P_{jmax}(n_i^k, t)$
 - 8: **if** $P_{jmax}(n_i^k, t) - P_{in}(n_i^k, i, t) > thr$ **then**
 - 9: Remove the serving cell from i^{th} cluster and add it to the j^{th} cluster
 - 10: **end if**
 - 11: **end for**
 - 12: After T seconds repeat DJP-LM Algorithm (go to step 1)
-

Although the first approach has its own advantages to decrease the inter-cluster interference, it is not well suited for high-mobility scenarios. In such environments because of the mobility of the MSs we have to add/remove cells to/from the clusters more frequently. To do a re-clustering session the following messages needs to be exchanged (see Fig. 4.5). The serving VBS acquires information about the network topology by computing the total internal and external interference; then, it needs to advertise this information by TOP-NBR-ADV message to the serving and the neighboring clusters. When the serving and candidate cluster receive this message, they know that a MS from the serving cluster is approaching the candidate cluster. Once the serving cluster receives the TOP-NBR-ADV message, it will send a CLS-REQ message to the candidate cluster to check whether to change the cluster size. The candidate cluster sends CLS-RSP message to serving cluster as a response to the CLS-REQ to know whether it approves or rejects the CLS-REQ. CLS-REP is transmitted by the serving cluster to inform the serving VBS about the decision. If the decision is to change the cluster size, the serving VBS sends VBS-REQ message to the candidate cluster as a request to join. VBS-REQ contains the initial parameters that candidate cluster may need to know. The candidate cluster acknowledges the VBS-REQ by sending VBS-ACK to the serving VBS. VBS-REP is transmitted by serving VBS to the MS to inform about the change of serving cluster. At this time the serving VBS is added to the candidate cluster. Now, it is needed to synchronize and estimate the channel coefficient between the MS and new set of RRHs. This

procedure is time consuming and needs many iterations to adjust its local parameters. When the synchronization and channel estimation are done, MS can continue its normal operation. As it is discussed in Sect. 4.4, for high-mobility scenarios DJP-LM is associated with a high number of re-clustering procedure, which decreases the system performance. To overcome this problem we propose the other approach for high-mobility MSs.

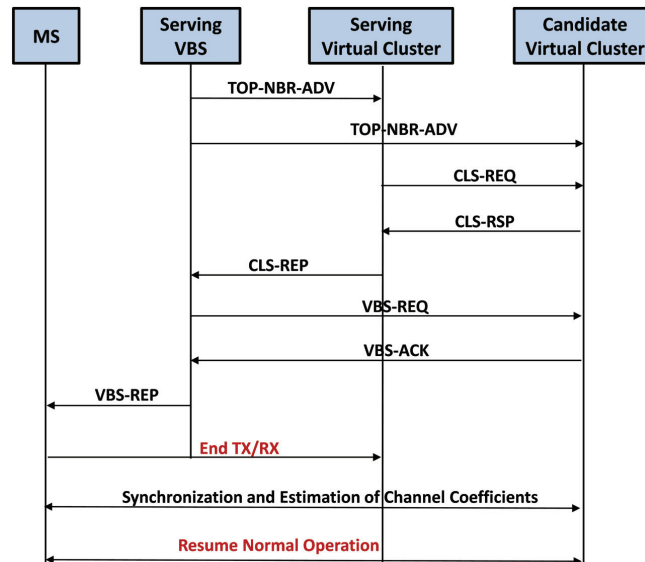


Figure 4.5: Message exchanges among a MS, serving VBS, and virtual clusters during re-clustering.

4.3.3 High-mobility Approach (DJP-HM)

In this part, we propose a new approach based on the C-RAN architecture that is appropriate for the high-mobility MSs. In this approach, named *DJP-HM*, we divide each cell into 3 sectors (so called S1, S2, and S3) and merge 3 neighboring sectors from different cells so to form a “*hybrid cell*” (see Fig. 4.6(a)). Consequently, as it is shown in Fig. 4.6(b), each VBS-Cluster serves a hybrid cell and consists of 3 Sector-VBSs, each of which serves different sector in the hybrid cell. Hence, hybrid cells are under the cooperation of 3 Sector-VBSs and, as a consequence, cooperative interference cancellation methods can be applied in hybrid cells.

Moreover, different sectors of a certain cell use different set of subbands such that the sectors of a hybrid cell use the same set of subbands (Fig. 4.6(c)). Hence, neighboring hybrid cells use different portions of the frequency band. In this case, all the subbands are used by each cell and the frequency reuse factor is equal to 1. Each Sector-VBS assigns each subband to a MS so that the subband is

used at most by three MSs in the hybrid cell. As a result, in each sector the intra-cluster interference is from the neighboring sectors of the serving hybrid cell. Since Sector-VBSs are able to cooperate with each other through VBS-Cluster, CoMP is able to cancel intra-cluster interference. On the other hand, since the neighboring hybrid cells in the first tier do not use the same set of subbands as the serving hybrid cell, we do not have any inter-cluster interference from them. Besides, as the hybrid cells operating on the same set of subbands are at the second tier of each other, they do not experience inter-cluster interference as high as that experienced by conventional CoMP.

In *DJP-HM*, we are also able to change dynamically the dedicated frequency band (subbands) to each hybrid cell. This leads to have more capacity and accept extra users *without deploying any extra antenna at RRHs*. In traditional cellular system, due to the static spectrum resources, we are not able to handle unanticipated fluctuations in the number of users and per-user capacity demands. However, in some scenarios like man-made disasters or when many users change their locations (e.g., from residential areas to downtown areas in the morning, and viceversa in the evening, the so-called “tidal effect”) the network may have more service demanding users in some hybrid cells rather than in their neighboring cells. To address this problem, we propose to change dynamically the dedicated frequency band to each hybrid cell based on the number of active MSs in the hybrid cells.

Whenever in a certain hybrid cell we have an overload and we need to serve more MSs, VBS-Cluster serving the hybrid cell can ask from all three associated VBSs to dynamically change the spectrum boundaries. If the associated VBSs have extra room in the other hybrid cells (i.e., hybrid cells in the first tier of overloaded hybrid cell), they handshake with each other and decrease dedicated frequency band of hybrid cells in the first tier and increase the frequency band of the overloaded hybrid cell (see Fig. 4.6(c)). Note that since we only decrease the frequency band of the first tier and do not change the frequency band of second tier, only the frequency bands of the overloaded hybrid cell and its first tier will be changed, and the symmetry of the rest of the network does not change. Consequently, there is no excessive ICI caused by allocating subbands from first tier of the overloaded hybrid cell.

In *DJP-HM*, we consider that the frequency spectrum is partitioned into 3 bands as,

$$\mathcal{F}^l = \{f_1^l, f_2^l, \dots, f_{K_l}^l\}, \quad l = 1, 2, 3, \quad (4.11)$$

where f_i^l is the i^{th} subband of the l^{th} band and $K_{tot} = K_1 + K_2 + K_3$ is the total number of subband. Let J^{HM} be the number of hybrid cells, $\mathcal{B}_j^{HM} = \{b_j^1, \dots, b_j^6\}$ ($1 \leq j \leq J^{HM}$) the set of neighboring hybrid cells located in the first tier of j^{th} hybrid cell, $\mathcal{D}_j^{HM} = \{d_j^1, d_j^2, d_j^3\}$ the set of associated VBSs in the j^{th} hybrid cell, \mathcal{F}_j^l the l^{th} band used by j^{th} hybrid cell, and $\bar{\mathcal{F}}_j^l = \sum_{q \neq l} \mathcal{F}_j^q$ the sum of bands used by \mathcal{B}_j^{HM} . As described in Algorithm 4, in the case of overloaded situation in j^{th} hybrid cell, the associated VBSs in \mathcal{D}_j^{HM} check for available subbands in $\bar{\mathcal{F}}_j^l$ and allocate them to \mathcal{F}_j^l . In Sect. 4.4 we will explain how this dynamic spectrum allocation can improve the system performance.

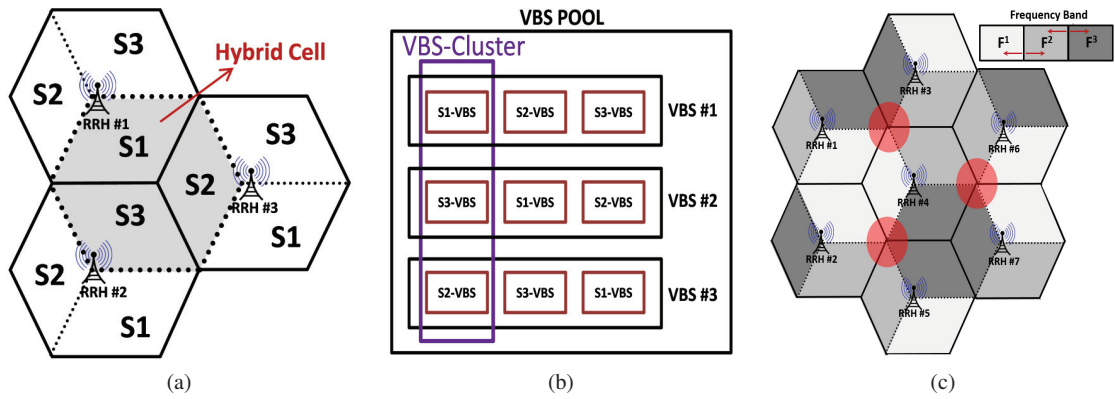


Figure 4.6: (a) Each cell consists of three sectors (S1, S2, and S3) and neighboring sectors from different cells form hybrid cells; (b) Each VBS consists of 3 Sector-VBSs each of which serves the corresponding sector in the cell (each VBS-Cluster is formed of 3 Sector-VBSs from different neighboring cells); (c) To avoid inter-cluster interference we use different portion of frequency band in different hybrid cells; we also change the boundaries of frequency sub-bands to address the unanticipated fluctuations in the number of users and per-user capacity demands.

Although in DJP-HM we do not need to change the cluster size and we do not have to re-provision the VBS-Clusters, there is an interference leakage from some corners of the hybrid cell to the neighboring hybrid cells. So, MS signals may interfere with neighboring external RRHs that use the same set of subbands. Figure 4.6(c) shows some circled areas in which the MS signals may be interfered with RRHs of non-neighboring hybrid cells. In Sect. 5.4, we will show that this phenomena decreases the performance of DJP-HM compared to DJP-LM.

4.3.4 Dynamic Joint Processing (Joint DJP-LM and DJP-HM)

Here, we explain how we are able to support both high- and low-mobility MSs. Since functionalities of both high- and low-mobility approaches are implemented on VMs, we are able to exploit them

Algorithm 3 DJP-HM

Input: K_r = Number of required subbands to serve the MS, j = index of serving hybrid cell, \mathcal{B}_j^{HM} = Set of neighboring hybrid cells, \mathcal{F}_j^l = Frequency band used by serving hybrid cell, $\bar{\mathcal{F}}_j^l$ = Frequency band used by \mathcal{B}_j^{HM}

Description:

- 1: **if** the K_r required subbands is available in \mathcal{F}_j^l **then**
 - 2: Set the K_r required subbands to the MS;
 - 3: **else**
 - 4: Check if there is unused subbands in $\bar{\mathcal{F}}_j^l$;
 - 5: **if** yes **then**
 - 6: Ask \mathcal{B}_j^{HM} to allocate subbands from $\bar{\mathcal{F}}_j^l$ to \mathcal{F}_j^l until there is K_r required subband in \mathcal{F}_j^l
 - 7: Set the K_r required subbands to the MS;
 - 8: **end if**
 - 9: **end if**
-

jointly so as to solve the inter-cluster interference problem. As we explained earlier, we propose to divide the MSs into two categories: (i) low-mobility and (ii) high-mobility MSs, based on the their velocity. Then, for low-mobility MSs, we propose to deploy DJP-LM, where we have more freedom to adjust the clusters size and decrease the inter-cluster interference. For high-mobility MSs, since DJP-LM leads to frequent variations in cluster size, we propose to deploy DJP-HM. Hence, our solution is to use both approaches jointly in order to leverage the combined advantages of both DJP-LM and DJP-HM.

Moreover, it should be mentioned that the number of subbands assigned to each approach can also be changed based on the number of high- and low-mobility MSs as well as on the traffic fluctuation in the network. If over the time the number of high- and low-mobility MSs changes in a region, we can also change the number of associated subbands to each approach so as to match the mobility fluctuation. It should be mentioned that in both approaches, since each MS is served by a set of VBSs there is no handover as it is defined in traditional cellular network. This means that each MS is actively connected to multiple VBSs and even in the re-clustering procedure at least one of the VBSs remains the same. This is different from the hard handover scheme in traditional cellular system where the connection between the serving BS and MS is terminated before the connection between the new BS and the MS is started. So, there is no traditional handover definition and due to the movement of MS only the set of cooperative VBSs should be changed in a smart way to provide better performance.

4.4 Performance Evaluation

We provide here a range of Monte Carlo simulations to evaluate the performance of our solution. Table 6.3 lists the stimulation parameters used during our experiments. In the simulations, we use an equally-sized hexagonal cell structure with two tiers of interfering cells, the inter-site distance D , and cell radius R (as depicted in Fig. 4.8) where 50 MSs are uniformly distributed over each cell site. To implement the conventional CoMP scheme, we consider the omni-subcarrier clusters of size 3. We compare the metrics between the traditional cellular network (without Inter-Cell Interference Coordination (ICIC)), Soft FFR [66], Regular CoMP, DJP-LM, and DJP-HM. For DJP-LM, we consider virtual uni-subcarrier clusters of size ranging in 2 – 4, where the average size is equal to the cluster size chosen for CoMP, Soft FFR, and DJP-HM (i.e., 3).

Table 4.1: Simulation Parameters.

Parameters	Mode/Value
Cellular Layout	Hexagonal grid
Channel Model	Path Loss and Shadowing
Frequency Reuse Factor	1
Transmission Power Ratio (ρ)	0.8
Cell Radius	500 m
Cluster Size in DJP	2 – 4
Channel Bandwidth	10 MHz
FFT size	1024
Number of Occupied Subcarrier	600
Subcarrier Spacing	15 kHz
Interior Radius in Soft FFR	$0.6R$
Distance Dependent Path Loss	$38.88 + 32\log(d)$ dB
Log-normal Shadowing Standard Deviation (σ)	7.5 dB
Threshold Velocity (V_{th})	5 m/s
Path Loss Exponent	3.2
Carrier Frequency	2.1 GHz
Number of Antennas (N_{TX}, N_{RX})	(1, 1)
MS Transmit Power	21 dBm
Hysteresis Threshold (thr)	6.2 dB
White Noise Power Density	-174 dBm/Hz
MS Antenna	Omni-directional
Receiver Processing	Zero Forcing
Modulation Scheme	OFDMA

For Soft FFR, we consider the structure showed in Fig. 4.7 with clusters of size 3, cell-edge reuse factor of 1/3, and cell-center radius of $0.6R$ (which is the optimum cell-center radius for a cluster of size 3 [67]). In Soft FFR, neighboring cells are divided into clusters of M cells and the overall system frequency band is partitioned into M sub-bands, where the cell-edge MSs are allocated based on a frequency reuse factor of $1/M$ and the cell-center MSs are allowed to share the sub-bands of cell-edge MSs in the other cells. The spectral efficiency of cell-edge MSs is controlled by the transmission power ratio (ρ), which is the ratio of the transmission power level of cell-center

region to the transmission power level of cell-edge region ($\rho = P_{in}/P_{out}$). It should be mentioned that decreasing the transmission power ratio will lead to an increase in the SINR of cell-edge region and a decrease in SINR of cell-center region. In our simulations we consider $\rho = 0.8$ and the proportional fair scheduling is used to allocate subcarriers to the MSs.

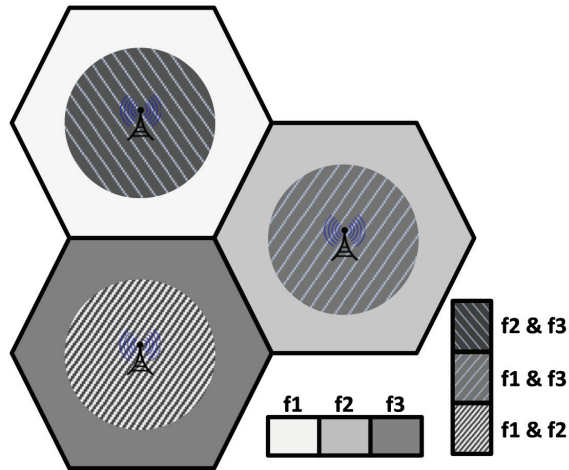


Figure 4.7: Soft-FFR deployment with a cell-edge reuse factor of 1/3.

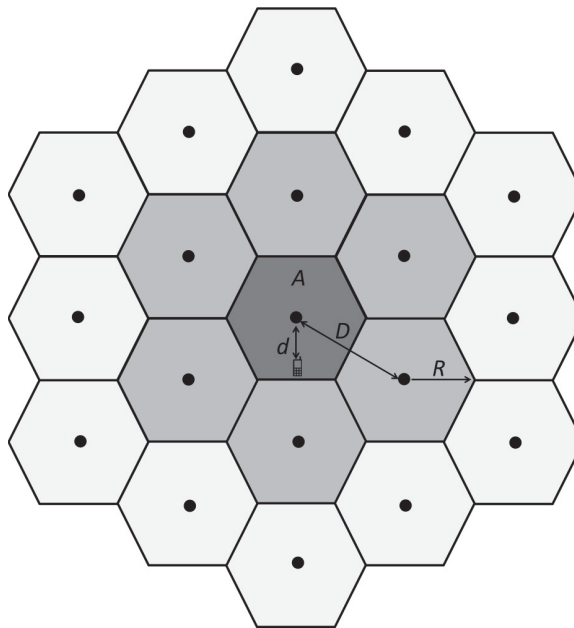


Figure 4.8: Equally-sized hexagonal cell structure with two tiers of interfering cells, where R is the Cell Radius, $D = \sqrt{3}R$ the Inter-site Distance, and $A = \frac{3\sqrt{3}}{2}R^2$ the Cell Area.

4.4.1 Propagation Model

Deterioration of signal quality is commonly assumed to depend upon the distance between the two antennae, the path(s) taken by the signal, and the environment around the path. We concentrate on the effects of path loss and shadowing, and employ this propagation model,

$$P_{rx} = K_0 \cdot \left(\frac{d}{d_0}\right)^{-\lambda} \cdot \psi \cdot P_{tx}. \quad (4.12)$$

In (6.1), P_{rx} , P_{tx} , d , and λ denote received power, transmitted power, propagation distance, and path-loss exponent, respectively. The parameter d_0 indicates a reference distance where the signal strength is known. The random variable ψ is used to model the slow fading caused by shadowing and follows a log-normal distribution such that the variable $10 \log_{10} \psi$ has a zero-mean Gaussian distribution with standard deviation σ . Parameter K_0 is a constant corresponding to the path loss at distance d_0 and depends on carrier frequency, antenna characteristics, propagation environment, and reference distance. Note that the full advantage of CoMP is achievable when the instantaneous CSI is available at the receiver. However, the CSI acquisition is practically limited by how fast the channel conditions are changing. In fast-fading systems only statistic CSI is reasonable to assume, whereas, in slow-fading systems, instantaneous CSI can be estimated.

4.4.2 Simulation Results

In the first simulation, we compare SINR and SE in terms of the Normalized Distance. The SINR and Spectral Efficiency (SE) of the i^{th} user operating over the k^{th} subcarrier are defined as,

$$\text{SINR}_i(k) = \frac{P_i \left| \mathbf{g}_i^{zf}(k) \mathbf{h}_i^{in}(k) \right|^2}{N_0 \Delta B + \sum_{j=1}^L P_j \left| \mathbf{g}_i^{zf}(k) \mathbf{h}_j^{ex}(k) \right|^2}, \quad (4.13)$$

$$\text{SE}_i = \log_2(1 + \text{SINR}_i(k)),$$

where $\mathbf{g}_i^{zf}(k)$ is the i^{th} row of the equalizer matrix $\mathbf{G}_{ZF}(k)$, $\mathbf{h}_i^{in}(k)$ is the i^{th} column of $\mathbf{H}_{in}(k)$, $\mathbf{h}_j^{ex}(k)$ is the j^{th} column of $\mathbf{H}_{ex}(k)$, N_0 is the white noise power spectral density, and ΔB is subcarrier spacing. Let d be the distance between a MS and the center of its serving cell as shown in Fig. 4.8. In Figs. 4.9 and 4.10, the SINR and SE of different schemes are compared for different Normalized Distances (d/R). Compared with the traditional network, Soft FFR, and regular CoMP,

our proposed solutions provide a significant gain. For instance, for cell-edge MSs ($d/R = 0.9$) compared to regular CoMP, we have 176% and 107% improvement for DJP-LM and DJP-HM, respectively. This is because we dynamically change the cluster size, which leads the distance between the external MSs and internal RRHs to be larger and the corresponding channel to have a smaller norm ($\|H_{ex}^{DJP}\| < \|H_{ex}^{CoMP}\|$).

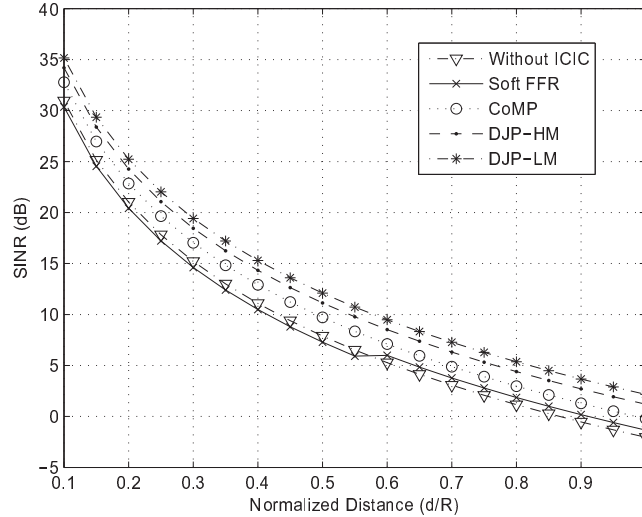


Figure 4.9: Signal-to-Interference-plus-Noise Ratio (SINR) for different Normalized Distances.

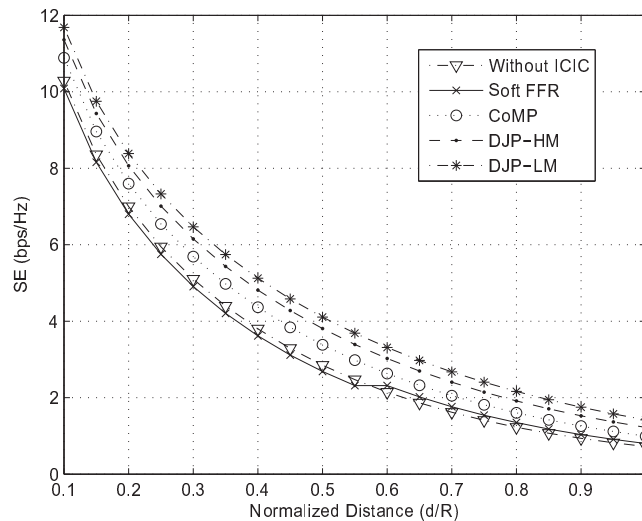


Figure 4.10: Spectral Efficiency (SE) in terms of Normalized Distance.

In the second simulation, we examine the performance of our solution in terms of outage probability, which is defined as the probability that a MS's instantaneous SINR falls below a threshold θ , i.e., $P(\text{outage}) = P(\text{SINR} < \theta) = 1 - P(\text{SINR} > \theta)$. Figure 6.11 shows the variations of outage probability in terms of different SINR thresholds. Note that for $\theta = 3$ dB the outage probability for DJP-LM and DJP-HM are 0.11 and 0.23, respectively, while regular CoMP has the outage probability of 40%. In the next simulation, we compare the Cumulative Distribution Function (CDF) concerning the SINR for different schemes. From Fig. 6.12, it is clear that for Soft FFR, 20% of the MSs have the SINR less than 0 dB. This means that the power of received interference for 20% of MSs is greater than the power of the received desired signal; whereas in our solution all the MSs have a SINR greater than 2 dB.

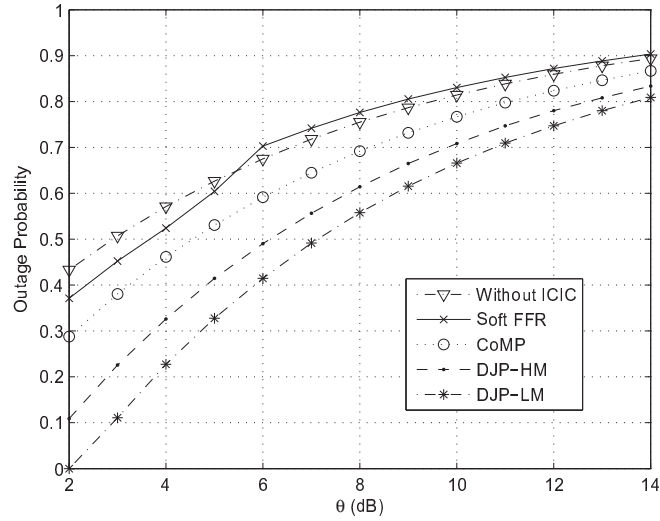


Figure 4.11: Outage probability for different thresholds.

Since the interference highly depends on the path loss exponent, in the other experiment we explored the variation of the average throughput of the system versus path loss exponent for different schemes. The throughput of the i^{th} MS is also obtained based on SINR of the MS as,

$$T_i = W_i \log_2(1 + \text{SINR}_i), \quad (4.14)$$

where W_i is the bandwidth of subcarriers assigned to the MS. Then, the cell throughput is the total

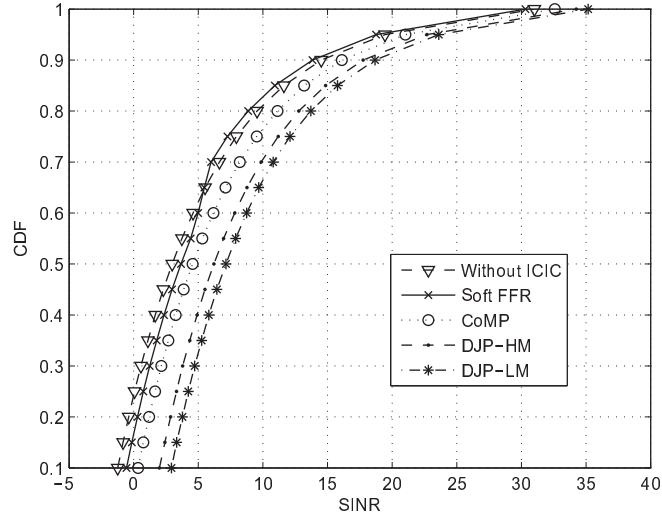


Figure 4.12: Cumulative Distribution Function (CDF) as a function of SINR.

throughput of all the MSs in the cell,

$$T_{cell} = \sum_{i=1}^N T_i, \quad (4.15)$$

where N is the total number of MSs. Moreover, to show the performance of our joint solution (DJP) integrating DJP-LM and DJP-HM, we consider 2 scenarios. In the first scenario 30% of the MSs in each cell are high mobility and 70% of them are low mobility, while in the second scenario 70% of the MSs in each cell are high mobility and 30% of them are low mobility. As shown in Fig. 6.13, for an urban area where the average pass loss exponent is 3.1, DJP-LM and DJP-HM have an average throughput of 24.81 and 21.77 Mbps respectively, whereas for regular CoMP the average throughput is equal to 15.09 Mbps. As expected, the performance of our joint solution is bounded between the performance of DJP-HM and DJP-LM. Note that the first scenario with higher number of low-mobility MSs has a better performance than the second scenario.

In the other experiment we explore the variation of Average System Spectral Efficiency (ASSE) for different SNR. ASSE is measured in bps/Hz/cell and is a measure of information rate that can be transmitted over a given bandwidth in a defined geographic area. As it is shown in Fig. 6.14, for low SNR values, ASSE for all schemes are very close to each other, but when SNR increases our proposed solution outperform the other schemes. For instance, for SNR= 20 dB, DJP-LM and

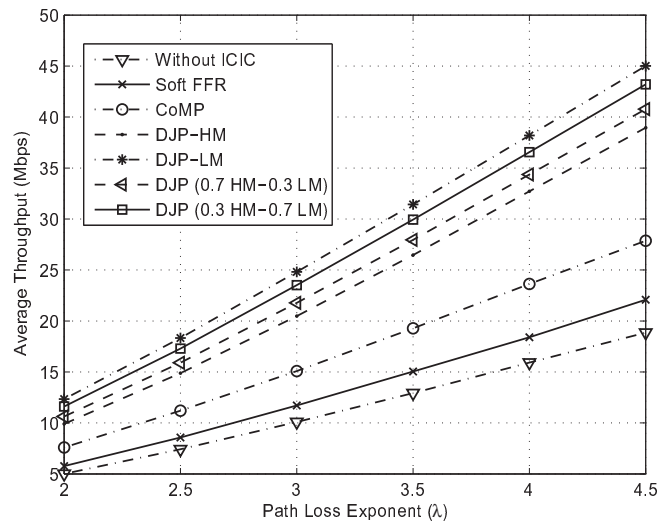


Figure 4.13: Average Throughput for different path loss exponents.

DJP-HM have the ASSE of 2.55 and 2.11, respectively, while for regular CoMP ASSE is equal to 1.58.

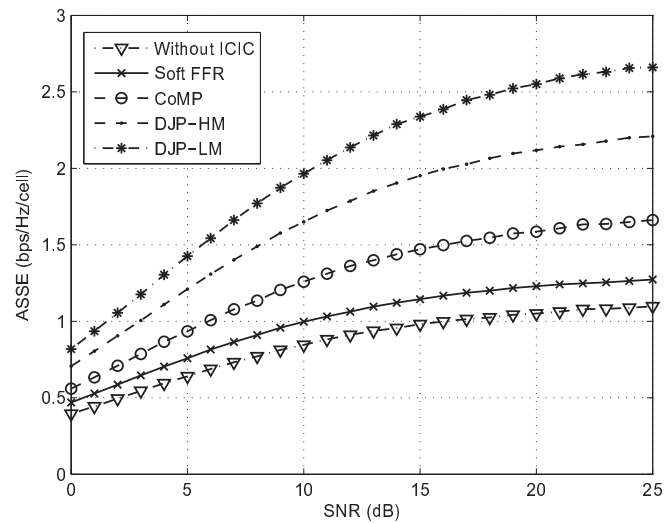


Figure 4.14: Average System Spectral Efficiency (ASSE) as a function of SNR.

In Fig. 6.15, BER performance of different schemes is investigated for different Normalized Distances. Due to the lower interference, our solution provides better performance than the other schemes. For instance, for cell-edge MSs ($d/R = 0.9$), the BER for DJP-LM and DJP-HM are 0.034 and 0.049, respectively, while for CoMP is 0.061.

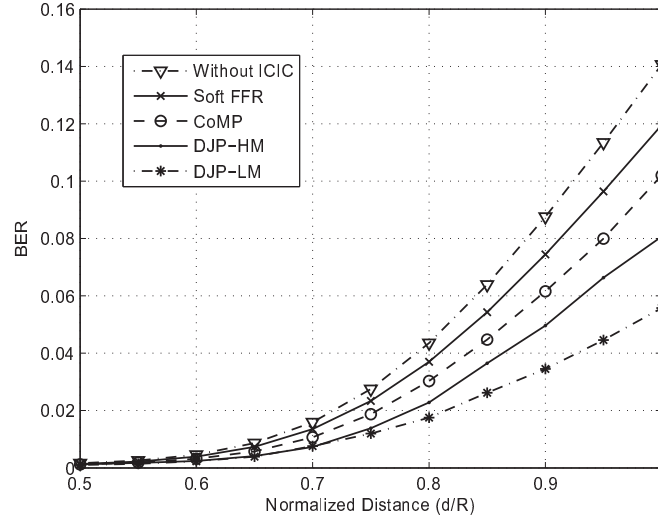


Figure 4.15: BER for different Normalized Distances.

In order to show the performance of imperfect CSI due to the fast-fading loss, we model the noisy channel estimation as in [68],

$$\hat{\mathbf{H}} = \mathbf{H} + e\mathbf{\Omega}, \quad (4.16)$$

where $e\mathbf{\Omega}$ is the estimation error that is uncorrelated with \mathbf{H} ; the entries of $\mathbf{\Omega}$ are normally distributed (with zero mean and unit variance), and e is the measure of channel estimation accuracy. Figure 6.16 shows the average BER of different schemes in terms of different channel uncertainties. As expected, by increasing the channel uncertainty the BER of CoMP, DJP-LM, and DJP-HM will increase and converge to each other.

Re-clustering (add/drop sessions) highly depends on the MS velocity and cell radius. Decreasing the cell radius or increasing the MS velocity will increase the number of re-clustering procedures. We have provided a table on this phenomenon and showed the number of re-clustering procedures for different cell radii and MS velocities. To show the performance of DJP-LM in terms of number of add/drop sessions, we consider Random Waypoint and Gauss-Markov [59] mobility models which are studied in Chapter 3.4. Table 4.2 shows the number of add/drop sessions for different cell radii, velocities, and methods where the simulation time is one hour. For high-mobility MSs and small cells, DJP-LM is associated with a large number of add/drop sessions, which may decrease the system performance, while DJP-HM is associated with lower number of add/drop sessions.

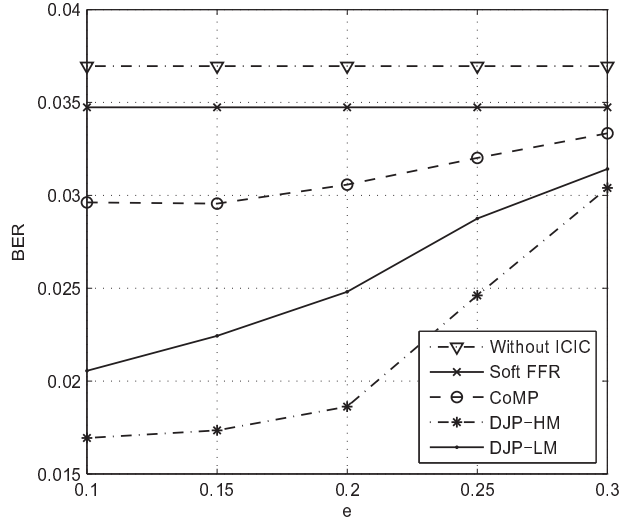


Figure 4.16: Comparison of Average BER in terms of channel uncertainty.

Table 4.2: Re-clustering procedures per subcarrier per cell for different cell radii, velocities, and methods.

Method and Velocity	Cell Radius = 100 m		Cell Radius = 300 m		Cell Radius = 600 m	
	DJP-LM	DJP-HM	DJP-LM	DJP-HM	DJP-LM	DJP-HM
Random Waypoint $s_{min} = 5m/s, s_{max} = 10m/s$	371	107	136	28	72	15
$s_{min} = 10m/s, s_{max} = 20m/s$	654	187	239	51	125	29
$s_{min} = 20m/s, s_{max} = 40m/s$	1044	293	371	82	198	46
Gauss-Markov $\bar{s} = 7.5m/s$	245	59	74	14	37	8
$\bar{s} = 15m/s$	501	76	167	21	53	11
$\bar{s} = 30m/s$	629	230	197	43	151	24

In the next experiment, we examine the performance of our solution in terms of Energy Efficiency (EE); we consider a metric and a power consumption model as described below. EE is defined as the ratio of cell throughput to the cell power consumption and is measured in bit-per-Joule. Since in C-RAN the power consumption of the system is lower than in distributed cellular networks [20] and DJP improves the spectral efficiency (and consequently throughput), we expect to have better EE. In order to assess the potential of DJP in terms of EE, we use the CoMP power model in the uplink as specified in [69], such that,

$$P_T = N_{ms}P_{ms} + P_{bh}, \quad (4.17)$$

where N_{ms} is the number of MSs in the cluster, P_{ms} is the transmit power of each MS, and P_{bh} is the power required for backhauling. We also use the backhaul link power model as given in [70],

$$P_{bh} = P_{olt} + \sum_{j=1}^{M_{rrh}} P_{tl}^j, \quad (4.18)$$

where P_{olt} is Optical Line Terminal (OLT) power consumption, P_{tl} is the transport link power consumption, and M_{rrh} is the number of RRHs in the cluster. The typical values are $P_{olt} = 20W$ and $P_{tl} = 3.85W$. Then, the cell's EE is defined as,

$$\eta_{EE} = \frac{M_{rrh} T_{cell}}{P_T}. \quad (4.19)$$

Figure 4.17 compares the η_{EE} of different schemes for different environments (different path loss exponents). As expected, DJP shows better EE than the other schemes. For instance, in urban areas with $\lambda = 3.1$, η_{EE} for DJP-LM and DJP-HM are 249 and 202 kbits/J, respectively, while for CoMP is 153 Kbits/J.

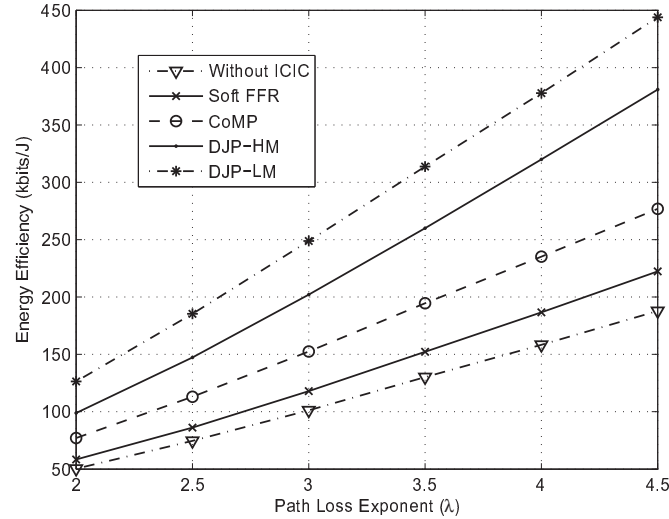


Figure 4.17: Performance of Energy Efficiency (EE) of different methods in different environments vs. varying path loss exponents.

As we discussed in Sect. 4.3.3, to address the fluctuation in capacity demand we proposed to dynamically change the frequency band boundaries. To examine this characteristic of DJP-HM, we simulated the following simple scenario. We assume a set of cells have equal number of MSs (in

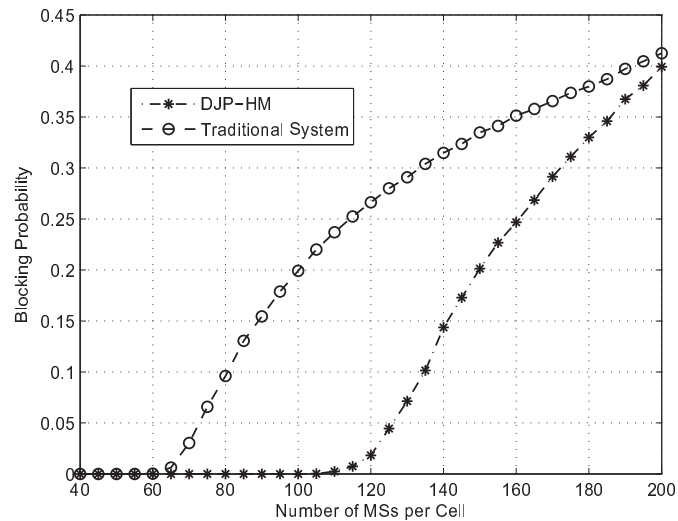


Figure 4.18: Comparison of Blocking Probability between traditional cellular system and DJP-HM for different number of MSs.

our simulation the number of MSs per cell varies from 40 to 200), each cell have 600 subcarrier to serve the MSs, and in each cell an active MSs needs 1 Resource Block (12 subcarriers) to be served. We also assume that we have 2 kind of cells: 1) the cells in which the probability of MSs to be active is $1/4$ and 2) the cells in which the probability of MSs to be active is $3/4$. This indicates that, because of some emergency reasons, we have more active MSs in some region by 3 times. Figure 4.18 compares the blocking probability when the number of users per cell increases. As it is shown, the blocking probability for DJP-HM is less than the traditional network and we are able to serve more users.

4.5 Discussion

We presented a solution that leverages the centralized nature of C-RAN to decrease the inter-cluster interference in CoMP. We discussed two different approaches, DJP-LM and DJP-HM, for low- and high-mobility MSs, respectively: in the former we define uni-subcarrier clusters whose sizes are changed based on the position of the MSs. In the latter each cell is divided into three fixed-size sectors and different neighboring sectors of various cells form the hybrid cells; to avoid inter-cluster interference, neighboring hybrid cells use different sets of subcarriers. Both approaches can coexist so to leverage their complementary advantages. Monte Carlo simulations show that DJP-LM and

DJP-HM have an average SINR of 7.24 and 6.15 dB, respectively, both higher than in conventional CoMP (4.72 dB).

Chapter 5

Coordinated Fractional Frequency Reuse in C-RAN

5.1 Overview

Fractional Frequency Reuse (FFR) and Coordinated MultiPoint (CoMP) processing are two major interference management techniques and are expected to play a fundamental role in achieving the high data-rate requirement of 5G systems. However, both FFR and CoMP have their own drawbacks over the current D-RAN. This is because the current D-RAN architecture is over 40 years old and was not originally designed for high spectral efficiency performance, but for coverage and mobility consideration. *On the other hand, the interference cancellation in the uplink is more challenging than the downlink for two reasons. First, in the uplink the transmission antennas are omnidirectional and we can not direct the signal to the desired point. Second, in the uplink there is no inter-MS connection between the MSs and they cannot exchange data to precode the signals and form the beams before transmission.*

There are two main types of FFR deployments presented in the literature, namely *Strict FFR* and *Soft FFR* [71]. Strict FFR, as shown in Fig. 5.1(a), is a modification of the traditional frequency reuse used extensively in multi-cell networks where a low frequency reuse factor is chosen for the cell-edge MSs while a larger frequency reuse factor is used for the cell-center MSs. Although Strict FFR decreases the ICI, it results in poor overall frequency reuse. To alleviate this problem, Soft FFR uses the same cell-edge bandwidth partitioning strategy, but the cell-center MSs are allowed to use the sub-band frequencies allocated to the cell-edge MSs of the other cells (see Fig. 5.1(b)). This strategy leads to a higher availability of spectrum resources; nevertheless, it generates more interference to both cell-center and cell-edge MSs than Strict FFR [71]. *Last, but not least, partition sizes in FFR schemes are not adaptive to dynamic changes in capacity demand, which makes FFR not able to handle the unanticipated fluctuations in the number of users.* On the other hand, as we discussed in Chapter 6, CoMP has the problem of high inter-cluster interference, delay, complexity,

and scarce inter-BS connectivity.

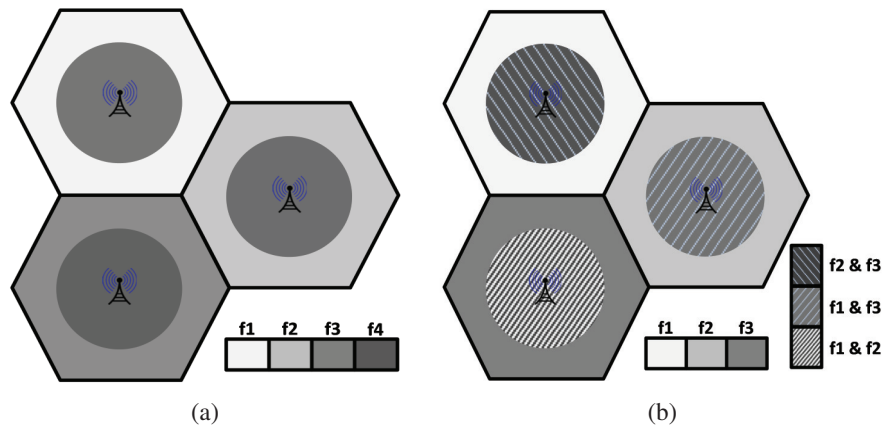


Figure 5.1: (a) Strict-FFR and (b) Soft-FFR deployments with cell-edge reuse factor of $1/3$.

In this chapter, we leverage the advantages of FFR, CoMP, and C-RAN and propose a novel clustering and spectrum sharing scheme for uplink interference-cancellation to increase the system spectral efficiency and also decrease *both* the intra- and inter-cluster interference. In the proposed solution, for each cell we define an Interference Region (IR); based on the IR of its neighboring cells, we then determine the Cell-Center Region (CCR). Since the cell-center MSs experience high level of SINR, we propose to apply CoMP processing *only* to cell-edge MSs, which leads to a decrease in the total complexity and latency. This way, unlike the traditional OFDMA systems, the performance of the system in *all* the cell-edge regions relies on the cooperation of different VBSs, which avoids handover interruptions. Moreover, in order to deal with inter-cluster interference, which is not addressed in traditional CoMP, we propose to exploit the cooperation of different VBSs for different cell-edge regions. We define the clusters of size 2 and 3 depending on the IR intersection of neighboring cells; we partition the frequency band into 13 non-overlapping sub-bands, and allocate the frequency bands to the MSs based on their position. In our solution, we also dynamically change the boundaries of sub-bands and optimize their widths in order to address the unanticipated fluctuations in the number of users and per-user capacity demands.

5.2 Challenges of Fractional Frequency Reuse

FFR has been proposed as a solution to find a tradeoff between interference reduction and system spectral efficiency. In Strict FFR, the overall system frequency band is partitioned in such a way

that, in a *cluster* of M cells, the MSs in the CCR are allocated a common sub-band of frequencies while the rest of the frequencies are equally partitioned into M sub-bands and assigned separately to Cell-Edge Regions (CERs) of the cluster. Figure 5.1(a) shows a cellular network using a Strict-FFR deployment where the cell-edge reuse factor is equal to $1/3$. Since the cell-edge MSs use different frequency sub-bands than the cell-center MSs, the interference is reduced in both CCR and CER. With K_{tot} defining the total number of available subcarriers, the number of subcarriers allocated to the cell-center MSs K_{center} and cell-edge MSs K_{edge} is given in [71] as,

$$\begin{aligned} K_{center} &= \left\lceil K_{tot} \left(\frac{r_{center}}{r} \right)^2 \right\rceil, \\ K_{edge} &= \lfloor (K_{tot} - K_{center}) / M \rfloor, \end{aligned} \quad (5.1)$$

where r_{center} and r are the CCR and cell radii, respectively.

Although Strict FFR increases the SINR, only two sub-bands are allocated per cell in a cluster, which still leads to poor system spectral efficiency. In order to alleviate this problem, Soft FFR has been proposed. As shown in Fig. 5.1(b), in Soft FFR the frequency partitioning is the same as in its Strict counterpart, but the cell-center MSs are allowed to share sub-bands of CERs in the other cells. In Soft FFR, the allocation of subcarriers for cell-center MSs is the same as in Strict FFR, whereas the number of subcarriers allocated to the cell-edge MSs are given respectively as [71],

$$K_{edge} = \min (\lceil K_{tot} / M \rceil, K_{tot} - K_{center}), \quad (5.2)$$

And yet, while Soft FFR increases the system spectral efficiency, it results in more interference to *both* cell-edge and cell-center MSs, leading to a high service outage probability. Moreover, *in both Strict FFR and Soft FFR, the partition sizes are fixed and cannot adapt dynamically to the demand changes per region.* This means that, as there is no coordination among the neighboring cells, changing the partition sizes in one cell may cause intensive interference in the other cells.

To solve the aforementioned problems and improve the system performance, we propose to use *both* CoMP and FFR under the C-RAN architecture.

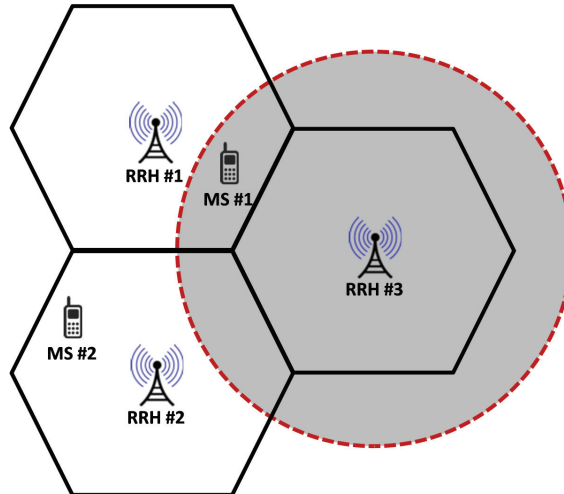


Figure 5.2: The Interference Region (IR) associated with cell #3 (gray region) includes the cell itself as well as the neighboring Cell-Edge Regions (CERs).

5.3 Coordinated Fractional Frequency Reuse in the Cloud (Cloud-CFFR)

In our Cloud-CFFR solution, we introduce a new clustering approach by exploiting the advantages of both FFR and CoMP as well as the capabilities of C-RAN to improve the overall system performance along different performance dimensions. Although the idea of Cloud-CFFR can be applied to any cell deployment, for simplicity we use regular hexagonal grid deployment (Fig. 5.2). We define an Interference Region (IR) for each cell as a region in which if MSs from other cells moved in, they could produce an “intense” interference at the BS serving the cell. Figure 5.2 shows three neighboring cells and the IR associated with cell #3 (in gray), which includes the cell itself as well as its neighboring Cell-Edge Regions (CERs). Here, both MS #1 and #2 are cell-edge MSs; in a system with a frequency reuse factor equal to 1, they may have destructive effects on the performance of their neighboring cells. Hence, their interference on the other cells needs to be canceled or mitigated to improve the overall SINR. Although MS #2 is a cell-edge MS, its interference at RRH #3 is low. This is because MS #2 is far from RRH #3 and, due to the path loss, the power of received signal (from MS #2) in the uplink at RRH #3 is low; hence, there is no need for VBS #2 and #3 to cooperate with each other in order to cancel the interference caused by MS #2 at RRH #3. Conversely, since MS #1 is in the IR of cell #3, there may be an intense interference from MS #1 to RRH #3; thus, coordination between VBS #1 and #3 is needed to cancel this interference.

In our solution, like in the traditional FFR, we partition the frequency band into 2 sub-bands,

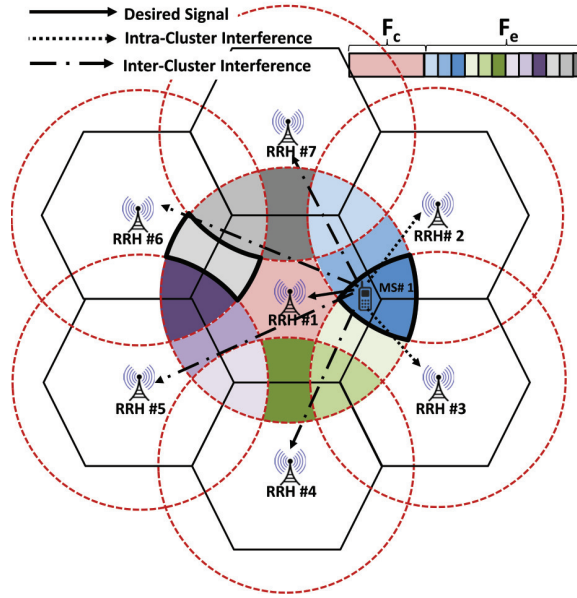


Figure 5.3: Intersections of serving cell's Interference Region (IR) with its neighboring cells' IRs.

namely F_c and F_e , for cell-center and cell-edge regions, respectively. Then, as shown in Fig. 5.3, we further divide the cell-edge spectrum (F_e) into 12 portions, each allocated to a certain cluster of VBSs to serve a certain region of cell edge. *So, in each cell all the frequency band is used by the MSs and the frequency reuse factor of 1 is achieved.*

Unlike in the traditional CoMP – in which the positions of MSs in the cell are not taken into account and all the BSs within a cluster cooperate with each other by exchanging CSI and MS signals – in our solution we divide the VBSs into *virtual edge clusters* based on the MS positions and minimize the number of coordinated VBSs so to bound the overall complexity and the delay associated with multiple-site reception/transmission as well as with CSI acquisition. In fact, we distinguish among the MSs based on their positions. We also leverage the C-RAN architecture and virtualization technology in such a way as to associate each VBS with different virtual edge clusters; this means that, for different areas of CER, each VBS coordinates with different VBSs in different virtual clusters, which increases the overall system performance. This way, only VBSs which have intensive interference from each other cooperate with each other to cancel the ICI.

Figure 5.3 shows the intersections of IRs of 7 hexagonal neighboring cells. We define CCR as the area where there is no intersection between the IR of the serving cell and the IRs of its neighboring cells (central and pink in the figure). If we define the IR of the i^{th} cell as $IR(i)$ then

its CCR is defined as relative complement of union of the IRs of its neighbouring cells with respect to $IR(i)$,

$$CCR(i) = IR(i) \setminus \bigcup_{j \in \mathcal{N}(i)} IR(j), \quad (5.3)$$

where $\mathcal{N}(i)$ is the set of neighbouring cells in the first tier of the i^{th} cell.

Since the CCR of each cell is out of the IRs of its neighboring cells, the interference from this region to the neighboring RRHs is not intense; hence, applying CoMP in this region would be highly inefficient due to the complexity, delay, and bandwidth usage to compute and exchange the CSI. Consequently, in our solution we do not apply computationally-expensive CoMP in CCR and the system performance in this region relies on simple single transmitter and receiver. To allocate the subcarriers to the CCR, we follow the strategy expressed in (5.1), as the number of allocated subcarriers is proportional to the CCR,

$$K_{CCR} = \left\lceil K_{tot} \left(\frac{A_{CCR}}{A_{cell}} \right) \right\rceil, \quad (5.4)$$

where K_{tot} is the total number of subcarriers, A_{CCR} is the area of CCR, and A_{cell} is the area of the cell site.

The system operation in cell-edge regions relies on the cooperation of different VBSs for different regions. Since we operate under the C-RAN architecture and all the VBSs are co-located in a common place (at the server, enclosure, or rack level in a datacenter), *it is possible for each VBS to cooperate with all its neighboring VBSs and share the CSI as well as MS signals at Gbps.* We define the CER of the i^{th} cell as relative complement of $CCR(i)$ with respect to $IR(i)$,

$$CER(i) = IR(i) \setminus CCR(i), \quad (5.5)$$

where, as shown in Fig. 5.3, $CER(i)$ consists of different intersection regions each of which is the intersection of $IR(i)$ with the IR of different neighbouring cells. We propose to divide the VBSs into clusters based on the intersections of their corresponding IRs in CER and apply CoMP within each cluster so to cancel the intra-cluster interference. This means that, in the cell edge and in each intersection region, the system performs under the cooperation of associated VBSs. For example, in the IR intersection of cells #1, #2, and #3, distinguished by bold lines on the right side of Fig. 5.3,

the system performs under the cooperation of VBSs #1, #2, and #3. This is because MSs located in this (dark blue) region and served by each of these three VBSs #1, #2, and #3 induce an intense interference on the other two VBSs (non-serving VBSs). For instance, in Fig. 5.3, MS #1 (which is served by VBS #1) is inside the IR of cells #2 and #3 and may cause poor system performance to VBSs #2 and #3; however, since MS #1 is outside the IR of the other neighboring cells and is far from their corresponding RRHs, due to the path loss, it does not induce a large interference on their VBSs.

To generalize from this example, we can state that *in order to improve the SINR of received signal by each RRH, we need to cancel the interference from those MSs located in its corresponding IR*. This requires *cooperation of each VBS with all its neighboring VBSs and in different clusters, which is only achievable in C-RAN architecture*. Similarly, with reference to the aforementioned example for MS #1, in the IR intersection of cells #1 and #6, the gray area distinguished by bold line on the left side of Fig. 5.3, only VBSs #1 and #6 need to collaborate with each other. In this way, each VBS is simultaneously associated with 12 different clusters to serve different regions of cell edge. Similar to (5.4) where the allocated subcarriers to CCR is proportional to the area of CCR, the number of allocated subcarriers to each edge-cluster region is given by,

$$K_{CER}(p) = \left\lfloor K_{tot} \left(\frac{A_{CER}(p)}{M(p)A_{cell}} \right) \right\rfloor, \quad (5.6)$$

where $K_{CER}(p)$ is the number of allocated subcarriers to the p^{th} cluster ($1 < p < 12$), $A_{CER}(p)$ is the area of the edge-cluster region, and $M(p)$ is the cluster size.

As in our solution we only apply CoMP to CERs and the average cluster size is 2.5, the complexity and delay is reduced compared to traditional CoMP. Moreover, as depicted in Fig. 5.4, in our solution the MSs using the same frequency sub-bands and served by different clusters are so far from each other that each cluster induces a very low level of interference on the corresponding neighboring cluster. *The average distance between the MSs using the same subcarrier and located in the different clusters are 3 times of cell radius, which is almost equal to the reuse distance of a cellular system with frequency-reuse factor of 1/3*. Since in our solution CoMP cancels the intense intra-cluster interference and VBSs experience a small inter-cluster interference (due to the long average inter-cluster distance), we achieve a low level of interference on the received uplink signal.

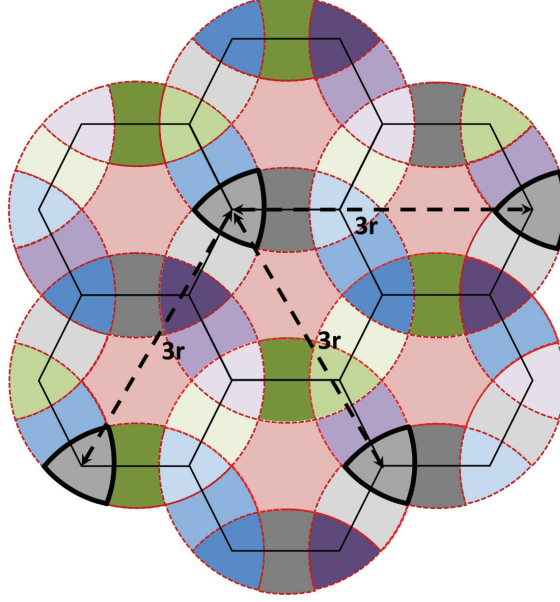


Figure 5.4: The average distance between the MSs using the same subcarrier and located in the different clusters are 3 times of cell radius.

The SINR of received signals at i^{th} RRH can be expressed as,

$$\begin{aligned} \text{SINR}_{\text{Cloud-CFFR}}^i &= \frac{\beta_i P_i |h_{i,i}^{in}|^2}{\sigma^2 + \sum_{j \in \mathcal{C}; j \neq i} P_j |h_{i,j}^{in}|^2 + \sum_{l \in \mathcal{I}} P_l |h_{i,l}^{ex}|^2} \\ &+ \frac{(1-\beta_i) P_i |\mathbf{g}_i^{zf} \mathbf{h}_i^{in}|^2}{\sigma^2 + \sum_{l \in \mathcal{I}} P_l |\mathbf{g}_i^{zf}(k) \mathbf{h}_l^{ex}(k)|^2} \end{aligned} \quad (5.7)$$

where P_i is the transmitted power of the MS located in the i^{th} cell, \mathcal{C} is the set of cells in the serving cluster, and \mathcal{I} is the set of interfering external cells. $h_{i,j}^{in}$ and $h_{i,j}^{ex}$ are the $(i, j)^{\text{th}}$ components of \mathbf{H}_{in} and \mathbf{H}_{ex} , respectively. \mathbf{g}_i^{zf} is the i^{th} row of the equalizer matrix \mathbf{G}_{ZF} , \mathbf{h}_i^{in} and \mathbf{h}_i^{ex} are the i^{th} column of \mathbf{H}_{in} and \mathbf{H}_{ex} , respectively, and σ^2 is the power of the noise. β_i is the location indicator and is equal to 1 when the MS is located in the CCR of i^{th} cell and equal to 0 when the MS is located in the CER. *We will analyse the SINR and compare it with different methods in Sect. 5.4.*

Dynamic Frequency Sub-band: In Cloud-CFFR, we are also able to change dynamically the dedicated sub-band to each region. This leads to higher capacity and multiplexing gains without deploying additional antennae at the RRHs. In traditional FFR systems, due to the static spectrum resources, we are not able to handle unanticipated fluctuations in the number of users and per-user capacity demands. However, in some scenarios like natural or man-made disasters or due to

the temporal/geographical fluctuations of MSs (the so-called tidal effect), the network may have more service demanding users in some regions. To address this problem, we propose to optimize the dedicated frequency sub-band to each cluster based on the number of active MSs in the clusters. Whenever in a certain cluster we have an overload and need to serve more MSs, the associated VBSs communicate with each other and dynamically change the sub-band boundaries so to increase the frequency sub-band for the overloaded region. If the associated VBSs have extra room in the other clusters and regions, they negotiate with each other and decrease the dedicated frequency sub-band of the other regions and increase the frequency sub-band of the overloaded region.

In the case of extra demand in the CCR of the j^{th} cell, we allocate the unused subcarriers of edge clusters to CCR. Let $\mathcal{C}_j^p(k)$ be the subset of VBSs (including the j^{th} VBS) serving the p^{th} edge cluster over the k^{th} subcarrier ($1 < k < K_{\text{CER}}(p)$) in CER of the j^{th} cell and $\mathcal{C}_j^p(k) = \mathcal{C}_j^p(k) \setminus j$. To avoid the excessive ICI caused by allocating the k^{th} subcarrier of \mathcal{C}_j^p to CCR, the VBSs in \mathcal{C}_j^p are not allowed to use the k^{th} subcarrier in the CER. Conversely, in the case of extra demand in some edge clusters in the CER of the j^{th} cell, we allocate the unused subcarriers of CCR and the other edge clusters to the overloaded edge cluster. To avoid the excessive ICI caused by allocating the k^{th} subcarrier of the q^{th} edge cluster to the overloaded edge cluster (say the l^{th}), the VBSs in $\mathcal{C}_j^q(k) \setminus \mathcal{C}_j^l$ are not allowed to use the k^{th} subcarrier in the CER. However, in the case of allocating unused subcarriers of CCR to overloaded edge clusters, there is no excessive ICI to the performance of $\bar{\mathcal{C}}_j^q$ and all the associated VBSs with the overloaded edge cluster can use the subcarriers from the associated CCRs. Algorithm 4 describes the dynamic spectrum feature of Cloud-CFFR.

Handover Scheme: In the Fourth Generation (4G) wireless networks, only Hard Hand-Over (HHO) (in which the connection between the serving BS and MS is terminated before the connection between the new BS and the MS is started) is defined to support MSs' mobility. As studied in [72], the service disruption time caused by HHO can be 250 ms or more, which is intolerable for some real-time services like Voice over IP (VoIP). On the other hand, with small cells, MSs perform handover more frequently leading to a decrease in the perceived Quality of Service (QoS). The degradation of QoS is a consequence of short interruption in communication during HHO due to redundant overhead generated for controlling and managing handovers. In our solution, cell-edge MSs are actively connected to 2 or 3 VBSs simultaneously so they do not have to terminate their connection with a serving VBS when they are moving from one cell to the neighboring cells. Hence,

Algorithm 4 Dynamic sub-band allocation in Cloud-CFFR

Input: K_r = number of required subcarriers to serve the MS, \mathcal{C}_j^0 = VBS associated to the j^{th} cell, \mathcal{C}_j^p = subset of VBSs serving the p^{th} virtual edge cluster, K_a = number of available subcarriers at the serving cluster, β = location indicator of the MS, \mathcal{F} = set of all subcarriers, \mathcal{F}_j^p = sub-band subcarriers used by the p^{th} virtual edge cluster.

Description:

- 1: $\bar{\mathcal{F}}_j^p = \mathcal{F} \setminus \mathcal{F}_j^p$;
 - 2: \mathcal{U}_j^p = set of unused subcarriers in the set $\bar{\mathcal{F}}_j^p$;
 - 3: $\mathbb{C}_j = \bigcup_{p=0}^{12} \mathcal{C}_j^p$ = set of all associated clusters to the j^{th} cell;
 - 4: **if** $K_a > K_r$ **then**
 - 5: Set K_r subcarriers to the MS;
 - 6: **else if** $\beta = 1$ and $|\mathcal{U}_j^0| \geq (K_r - K_a)$ **then**
 - 7: Ask \mathbb{C}_j to allocate $(K_r - K_a)$ subcarriers from \mathcal{U}_j^0 to \mathcal{F}_j^0 ;
 - 8: Do not use the donated subcarriers in the CER of donor cells;
 - 9: **else if** $\beta = 0$ and $|\mathcal{U}_j^l| \geq (K_r - K_a)$ **then**
 - 10: Ask \mathbb{C}_j to allocate $(K_r - K_a)$ subcarriers from \mathcal{U}_j^l to \mathcal{F}_j^l ;
 - 11: Do not use the donated subcarriers in the CER of the set $\mathcal{C}_j^q \setminus \mathcal{C}_j^l$;
 - 12: **end if**
-

even with small cells and in a high-mobility scenario, MSs do not experience any service disruption as each MS operates under cooperation of multiple VBSs within a cluster.

5.4 Performance Evaluation

In this section, we analyze the behavior of our proposed Cloud-CFFR solution in different regions and provide a range of simulations to evaluate its performance.

5.4.1 Setting

Table 6.3 lists the simulation parameters used during our experiments. In the simulations, we use an equally-sized hexagonal-cell structure with two tiers of interfering cells, the inter-site distance D , and cell radius r (as depicted in Fig. 5.5) where 50 MSs are uniformly distributed over each cell site and d is the distance between the MS and its serving RRH. To implement conventional CoMP, we consider a cluster of size 3. To compare Cloud-CFFR with Strict and Soft FFR, we consider the structures showed in Figs. 5.1(a) and (b) with cell-edge reuse factor of $1/3$, cluster size of 3 ($M = 3$), and CCR radius equal to $0.7r$ (which is the optimum CCR radius for $M = 3$ [73]). In Soft FFR, the spectral efficiency of cell-edge MSs is controlled by the transmission power ratio

(ρ), which is the ratio of the transmission power level of CCR to the transmission power level of CER (i.e., $\rho = P_c/P_e$). It should be mentioned that decreasing the transmission power ratio will lead to an increase in the SINR of CER and a decrease in SINR of CCR. In our simulations, we consider $\rho = 0.8$ and use proportional fair scheduling to allocate subcarrier to the MSs. Also, in order to have the same CCR for Cloud-CFFR, we consider $R_i = 1.3r$, as illustrated in Fig. 5.5. In the simulations, we compare performance metrics among the traditional cellular network (without ICIC), CoMP, Strict FFR, Soft FFR, and Cloud-CFFR. Although the performance of the Cloud-CFFR can be improved by applying the power control schemes, to show the full potential of Cloud-CFFR compared to the other methods we do not use any kind of power control schemes and the MS transmission power is fixed to 21 dBm.

Table 5.1: Simulation parameters.

Parameters	Mode/Value
Cellular Layout	Hexagonal grid, 19-cell sites
Channel Model	Path Loss and Shadowing
Transmission Power Ratio (ρ) for Soft FFR	0.8
Cell Radius	500 m
FFT size	1024
Channel Bandwidth (ΔB)	10 MHz
Number of Occupied Subcarriers	600
Subcarrier Spacing	15 kHz
CCR Radius for Soft FFR and Strict FFR	$0.7r$
IR Radius	$1.3r$
Distance-dependent Path Loss	$38.88 + 32\log(d)$ dB
MS Transmit Power	25 dBm
Log-normal Shadowing Standard Deviation (σ)	7.5 dB
Path Loss Exponent	3.2
Carrier Frequency	2.1 GHz
Number of Antennae (N_{TX}, N_{RX})	(1, 1)
White Noise Power Density	-190 dBm/Hz
MS Antenna	Omni-directional
Receiver Processing for CoMP	Zero Forcing (ZF)
Modulation Scheme	OFDMA

With the propagation model defined in Chapter 6 and based on the system model, the SINR of

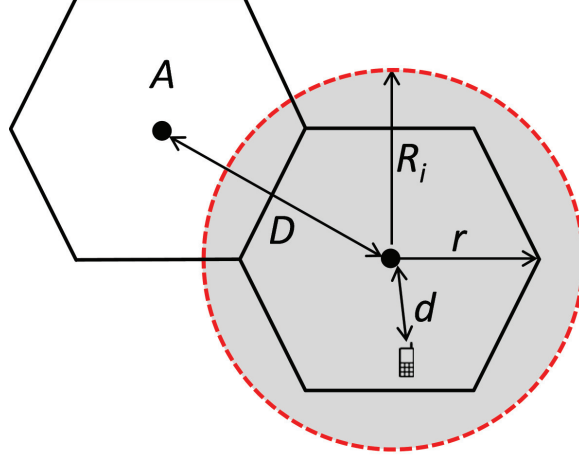


Figure 5.5: Equally sized hexagonal cell structures where r is the cell radius, $D = \sqrt{3}r$ is the inter-site distance, R_i is the IR radius, and $A = \frac{3\sqrt{3}}{2}r^2$ is the cell area.

received signals at i^{th} RRH for different methods can be expressed as,

$$\begin{aligned}
 \text{SINR}_{\text{StrictFFR}}^i &= \frac{\beta_i P_i |h_{i,i}^{\text{in}}|^2}{N_0 \Delta B_0 + \sum_{j \in \mathcal{C}, j \neq i} P_j |h_{i,j}^{\text{in}}|^2 + \sum_{l \in \mathcal{I}} P_l |h_{i,l}^{\text{ex}}|^2} \\
 &\quad + \frac{(1-\beta_i) P_i |h_{i,i}^{\text{in}}|^2}{N_0 \Delta B_0 + \sum_{l \in \mathcal{I}} P_l |h_{i,l}^{\text{ex}}|^2}, \\
 \text{SINR}_{\text{SoftFFR}}^i &= \frac{P_i |h_{i,i}^{\text{in}}|^2}{N_0 \Delta B_0 + \sum_{j \in \mathcal{C}, j \neq i} P_j |h_{i,j}^{\text{in}}|^2 + \sum_{l \in \mathcal{I}} P_l |h_{i,l}^{\text{ex}}|^2}, \\
 \text{SINR}_{\text{CoMP}}^i &= \frac{P_i |\mathbf{g}_i^{\text{zf}} \mathbf{h}_i^{\text{in}}|^2}{N_0 \Delta B_0 + \sum_{l \in \mathcal{I}} P_l |\mathbf{g}_i^{\text{zf}}(k) \mathbf{h}_l^{\text{ex}}(k)|^2}, \\
 \text{SINR}_{\text{Cloud-CFFR}}^i &= \frac{\beta_i P_i |h_{i,i}^{\text{in}}|^2}{N_0 \Delta B_0 + \sum_{j \in \mathcal{C}, j \neq i} P_j |h_{i,j}^{\text{in}}|^2 + \sum_{l \in \mathcal{I}} P_l |h_{i,l}^{\text{ex}}|^2} \\
 &\quad + \frac{(1-\beta_i) P_i |\mathbf{g}_i^{\text{zf}} \mathbf{h}_i^{\text{in}}|^2}{N_0 \Delta B_0 + \sum_{l \in \mathcal{I}} P_l |\mathbf{g}_i^{\text{zf}}(k) \mathbf{h}_l^{\text{ex}}(k)|^2}
 \end{aligned} \tag{5.8}$$

According to (5.8) and (5.7), here, we explain how Cloud-CFFR increases the overall throughput with respect to the other methods.

Compared to the Soft FFR, since $|h_{i,j}^{\text{in}}|$ in Cloud-CFFR is smaller (due to the higher path loss) than the one in Soft FFR we expect to have a better SINR for cell-center MS ($\beta_i = 1$). For cell-edge MS ($\beta_i = 0$), since there is no intra-cluster interference in Cloud-CFFR, we also expect to have a better performance than Soft FFR. Compared to the Strict FFR, the performance is the same for cell-center MSs, but SINR for cell-edge MSs in Cloud-CFFR is less than the one in

Strict FFR. This is because of the fact that in Strict FFR the cell edge reuse factor is $1/3$ and the number of interfering cells in Strict FFR is less than Cloud-CFFR ($|\mathcal{I}_{StrictFFR}| < |\mathcal{I}_{Cloud-FFR}|$). However, the number of available subcarriers per cell in Cloud-CFFR is 1.5 times more than the one in Strict FFR so that we expect to have more overall throughput with Cloud-CFFR (we will discuss about it through the simulations). Also, compared to CoMP, since the distance between the external MSs and internal RRHs is increased, the corresponding channel matrix in Cloud-CFFR has a smaller norm ($\|H_{ex}^{Cloud-CFFR}\|_2^2 < \|H_{ex}^{CoMP}\|_2^2$) which results to have a better performance in terms of both SINR and throughput. Moreover, the complexity of Cloud-CFFR is much lower than CoMP. The complexity of CoMP algorithm depends on the numbers of cooperative RRHs (M), associated MSs (N), and subcarriers (k_c). For instance, ZF receiver has a computational complexity of $\mathcal{O}(k_c M^3 N^3)$ [74]. Since in CoMP the interference cancelation is applied to all the subcarriers ($k_c = K_{tot}$), the system has an overall computational complexity of $\mathcal{O}(K_{tot} M^3 N^3)$. However, in Cloud-CFFR the average cluster size is 2.5 ($\bar{M} = \bar{N} = 2.5$) and ZF only is applied to the CER so that $k_c = 0.5K_{tot}$ which leads to have less computational complexity ($\mathcal{O}_{Cloud-CFFR} = 0.22\mathcal{O}_{CoMP}$).

5.4.2 Simulation Results

To test and validate the aforementioned statements, in the first simulation, we compare the SINR in terms of Normalized Distance. As it is shown in Fig. 5.6, Cloud-CFFR outperforms both CoMP and Soft FFR in CER; however, Strict FFR has a greater SINR in CER. This is because Strict FFR uses a frequency reuse factor of $1/3$ in CER and, according to (5.1) (for $r_{center} = 0.7r$), only use 66% of the frequency band. However, as we show next, the overall throughput of Strict FFR is less than that of Cloud-CFFR. Since the interference highly depends on path loss exponent, we also explore the variation of the average throughput of each cell versus path loss exponent for different schemes.

The throughput of each cell is given by,

$$R_{cell} = \frac{k_0}{K_{tot}} \Delta B \log_2 (1 + \text{SINR}), \quad (5.9)$$

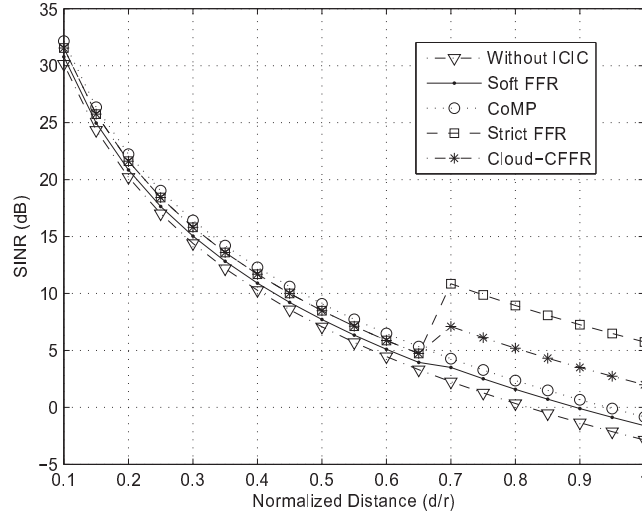


Figure 5.6: SINR for different Normalized Distances (d/r).

where k_0 and K_{tot} are the numbers of available subcarriers per cell and of total subcarriers, respectively, and ΔB is the channel bandwidth. As shown in Fig. 5.7, for an urban area where the average path loss exponent is 3.5, Cloud-CFFR has an average throughput of 28.43 Mbps, whereas for Strict FFR, Soft FFR, and CoMP the average throughput is 19.78, 18.92, and 24.26, respectively. As it is clear from Fig. 5.7, although Strict FFR has a better SINR in CER, its overall throughput is less than that of Cloud-CFFR. This is because Cloud-CFFR use all of the spectrum ($k_0 = K_{tot}$), while Strict FFR can only use a portion of it ($k_0 = 0.66K_{tot}$). We also examine the performance of our solution in terms of outage probability, which is the probability that a MS's instantaneous SINR falls below a certain threshold θ ,

$$P(\text{outage}) = P(\text{SINR} < \theta) = 1 - P(\text{SINR} > \theta), \quad (5.10)$$

Figure 5.8 shows the variation of the outage probability in terms of different SINR thresholds.

We also compare the Cumulative Distribution Function (CDF) concerning the SINR for different schemes; it is clear from Fig. 5.9 that for traditional network, Soft FFR, and CoMP, 20% of the MSs experience a SINR less than 0 dB. This means that the power of the received interference for 20% of MSs is greater than the power of received desired signal. However, in our solution all the MSs experience a SINR greater than 2.33 dB.

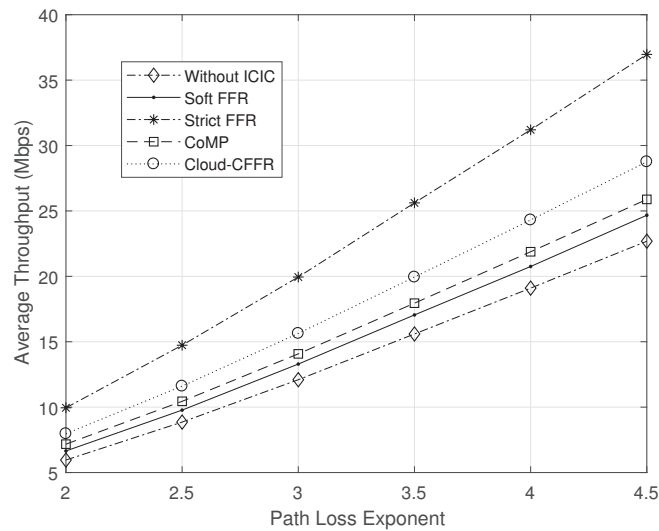


Figure 5.7: Average Throughput for different Pass Loss Exponent λ .

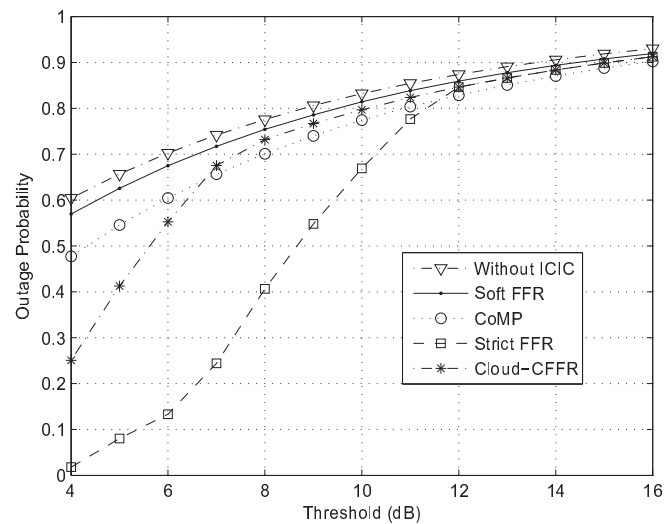


Figure 5.8: Outage Probability for different thresholds in dB.

In Fig. 5.10, BER performance of different schemes is investigated for CER ($0.7 < d/r < 1$). Due to the lower interference and higher SINR value, Cloud-CFFR provides better performance than CoMP and Soft FFR. For instance, for cell-edge MSs ($d/r = 0.9$), the BER for Cloud-CFFR is 0.023, while for CoMP and Soft FFR is 0.054 and 0.071, respectively. It should be mentioned that due to the frequency reuse factor equal to $1/3$ for cell-edge MSs, Strict FFR has better BER than Cloud-CFFR. However, as we discussed earlier and since the frequency reuse factor in Cloud-CFFR is equal to 1, the overall throughput of Cloud-CFFR is higher than that of Strict FFR.

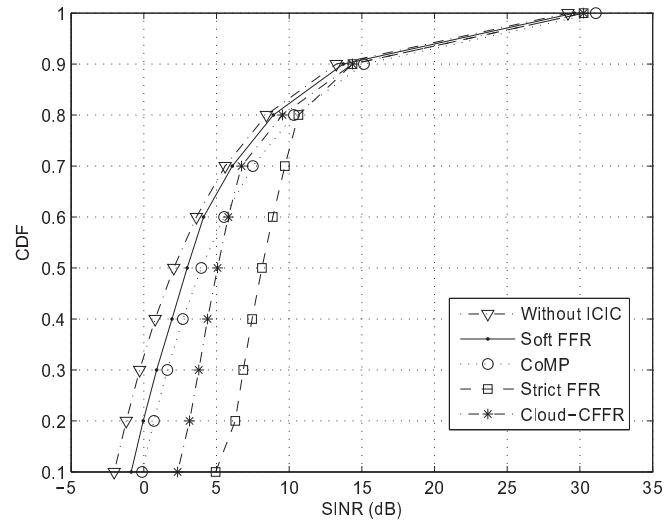


Figure 5.9: CDF as a function of SINR.

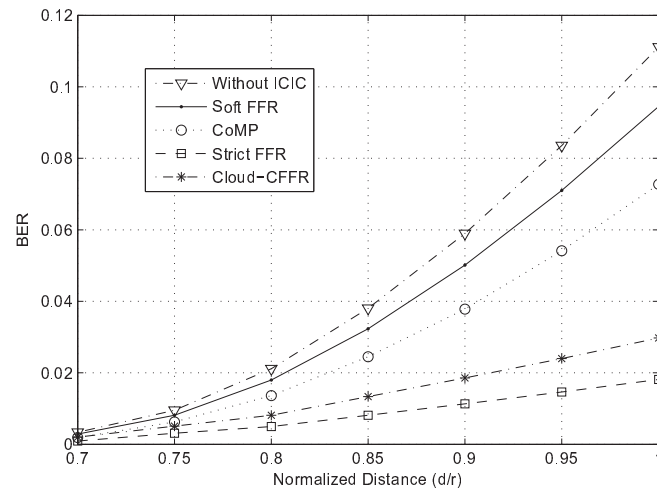


Figure 5.10: BER for different Normalized Distances.

Figure 5.11 shows the average BER of different schemes in terms of different channel uncertainties. As expected, by increasing the channel uncertainties, the performance of CoMP and Cloud-CFFR for cell-edge MSs decreases. This is because, the performance of Cloud-CFFR (in CER) and CoMP depends on the accuracy of CSI estimation, and with an imperfect CSI the intra-cluster interference cancelation cannot be perfect. However, as shown in Fig. 5.11, even with $e = 0.2$ Cloud-CFFR still shows great improvement over CoMP and Soft FFR.

In order to assess the potential of Cloud-CFFR in terms of energy efficiency, we use the CoMP

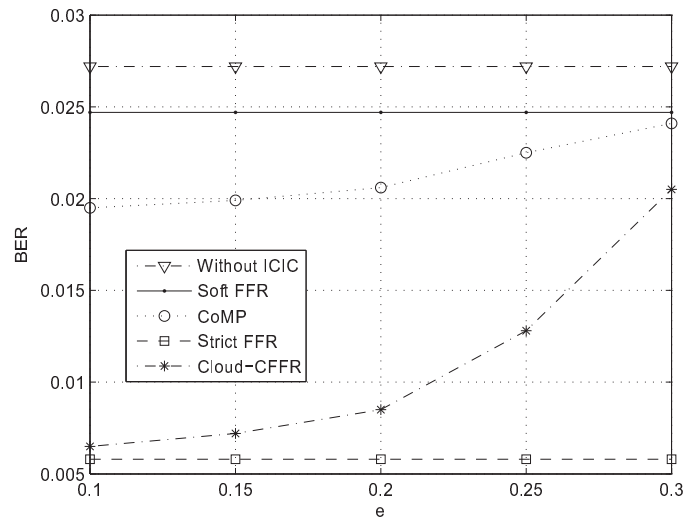


Figure 5.11: Comparison of Average BER in terms of channel uncertainty.

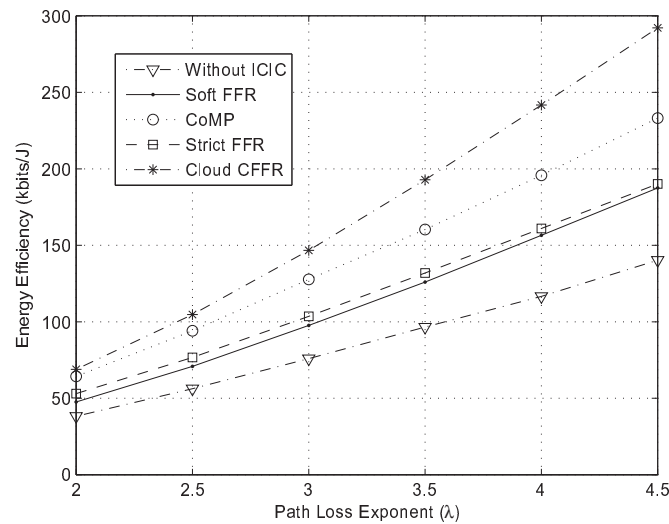


Figure 5.12: Performance of Energy Efficiency (EE) of different methods in different environments (different path loss exponents).

power model in the uplink, as specified in Chapter 6. Figure 5.12 compares the η_{EE} of different schemes for different environments (different path loss exponents). As expected Cloud-CFFR has better EE than the other schemes. For instance, in urban areas with $\lambda = 3.5$, η_{EE} for Cloud-CFFR is 192.8 Kbits/J, while for CoMP and Strict FFR is 160.4 and 131.9, respectively.

As discussed in Sect. 5.3, to address the fluctuation in capacity demand, we propose to change dynamically the frequency sub-band boundaries. To examine this characteristic of Cloud-CFFR, we

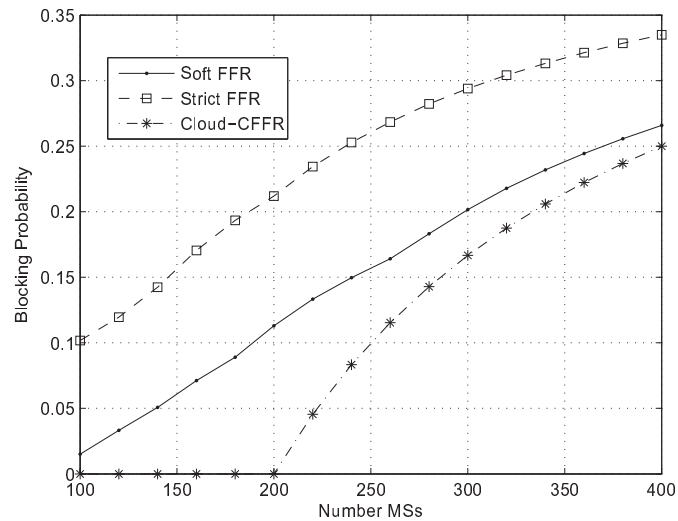


Figure 5.13: Comparison of Blocking Probability for different number of MSs.

simulated the following simple scenario; let us assume that a set of cells have an equal number of MSs (in our simulation the number of MSs per cell varies from 50 to 200), each cell has 50 resource blocks to serve the MSs, and in each cell an active MSs needs 1 resource block to be served. We also assume that we have three types of cells: 1) cells where the probability of cell-center and cell-edge MSs to be active is $1/2$ (i.e., density of active MSs in CER and CCR is equal), 2) cells where the probability of cell-center MSs to be active is $1/4$ while the probability of cell-edge MSs to be active is $3/4$ (i.e., the density of active MSs in CER is greater than CCR), and 3) cells where the probability of cell-center MSs to be active is $3/4$ while the probability of cell-edge MSs to be active is $1/4$ (i.e., the density of active MSs in CCR is greater than CER). Each cell can be any one of the three aforementioned types with equal probability. Figure 5.13 compares the blocking probability when the number of MSs per cell increases; as it is shown, the blocking probability for Cloud-CFFR is less than the traditional schemes and we are able to serve more active MSs.

5.5 Discussion

In the context of C-RAN, we proposed and validated a novel solution, named Coordinated Fractional Frequency Reuse in the Cloud (*Cloud-CFFR*). Our innovative cellular-uplink solution mitigates the inter-cluster interference and decreases complexity and delay while increasing the overall system spectral efficiency. We proposed to apply CoMP only to cell-edge MSs and exploit the cooperation

of different VBSs for different cell-edge regions. Moreover, to address the unanticipated change in capacity demand, Cloud-CFFR dynamically changes the sub-band boundaries based on the number of active users in the clusters. Simulation results confirmed the validity of our analysis and showed the benefits of this novel uplink solution. For instance, in the urban area Cloud-CFFR outperforms competing schemes such as Strict FFR, Soft FFR, and CoMP in the average throughput by 45%, 52%, and 20%, respectively.

Chapter 6

Demand-Aware Resource Allocation for High Energy Efficiency and Resource Utilization in C-RAN

6.1 Overview

At the stage of network planning, cell size and capacity are usually determined based on the estimation of peak traffic load. However, *due to the tidal effect, there is no fixed cell size and transmission power that optimize the overall power consumption of the network.* This means that the use of small cells is quite efficient in terms of power consumption as well as utilization of spectrum and computing resources when the capacity demand is high and evenly distributed in space; however, it becomes less so when the data traffic is low and/or uneven due to the static resource provisioning and fixed BS power consumptions. *This is because the current cellular architecture is over 40 years old and was not originally designed for a high energy and spectral efficiency performance, but for coverage and mobility considerations.*

The economic impact of power consumption is particularly dire in emerging markets and the Fifth Generation (5G) of wireless cellular network must be not only spectral efficient but also energy efficient (e.g., a $1000\times$ improvement in energy efficiency is expected by 2020). Although several recent efforts have been made to reduce the power consumption of existing small cell networks [18, 19], limited attention has been given to optimize the overall network deployment. Therefore, a novel design and architecture is necessary for the next generation of wireless cellular network to overcome the aforementioned challenges.

In this chapter, we focus on optimizing the power consumption and resource utilization by leveraging the full potential of C-RAN architecture. We propose a novel elastic resource provisioning framework, called “Elastic-Net”, to minimize the power consumption while addressing the fluctuations in per-user capacity demand. In our solution, we divide the covered region into clusters based on the traffic model and, within each cluster, we dynamically adapt the active RRH density,

transmission power, and size of the VM¹ based on the traffic fluctuations. We introduce the idea of “VBS-Cluster” in which we merge the VBSs serving a cluster into a unit VBS-Cluster while the RRHs’ antennae in the cluster act as a single coherent antenna array distributed over the cluster region. We also provide a comprehensive model for the power consumption of the C-RAN system including: (i) RRH and transport network power consumption and (ii) VBS pool power consumption. Then, we optimize the power consumption and resource utilization through a demand-aware resource provisioning approach. In order to minimize the power consumption in the cell sites while ensuring a certain minimum coverage and data rate, we propose to dynamically optimize and adapt the RRH density and transmission power based on the traffic demand and user density. Likewise, in order to minimize the power consumption in the cloud we dynamically optimize and adapt the size of the VMs while ensuring that the frame-processing time is less than the frame deadline.

6.2 System Model

We consider a C-RAN downlink system and assume that each user is served by the nearest active RRH. The RRHs and users are distributed according to two independent Poisson Point Processes (PPPs) in \mathbb{R}^2 , denoted as Φ_r and $\Phi_u(t)$, respectively. Note that the distribution of users is a function of time due to their temporal variation. Let λ_r and $\lambda_u(t)$ denote RRH density and time-dependent user density, respectively. The set of all RRHs is denoted by $\mathcal{L} = \{1, \dots, L\}$ and $\mathcal{A} \subseteq \mathcal{L}$ is the set of active RRHs and $\mathcal{Z} = \mathcal{L} \setminus \mathcal{A}$ is the set of inactive RRHs. Let also $\mu_a(t) \in [0, 1]$ denote the RRH activity factor which indicates the ratio of active RRHs to all RRHs, where $\lambda_r^a(t) = \mu_a(t)\lambda_r$ is the time-dependent density of active RRHs and $\lambda_r^s(t) = (1 - \mu_a(t))\lambda_r$ is the time-dependent density of inactive RRHs. The total bandwidth is denoted by B and the bandwidth per user is given by $B_u(t) = B \frac{\lambda_r^a(t)}{\lambda_u(t)}$. Although the similar analysis can be applied for multi-antenna systems, for the sake of simplicity we assume that all RRHs and users are equipped with single antenna. We also concentrate on the effect of path-loss and shadowing, and employ a commonly used signal-propagation model as follows,

$$P_r = Gr^{-\alpha}hP, \tag{6.1}$$

¹The size of a VM is represented in terms of its processing power, memory and storage capacity, and network interface speed.

where P_r , P , r , and α denote received power, transmitted power, propagation distance, and path-loss exponent, respectively. Additionally, G is the path-loss coefficient and the random variable h is used to model the slow fading caused by shadowing and it follows a log-normal distribution. Under these assumptions the received signal for a typical user, denoted as u^{th} user, is given by,

$$y_u = r_u^{-\frac{\alpha}{2}} \sqrt{Gh_u P} s_u + \sum_{j \neq u, j \in \mathcal{A}} r_j^{-\frac{\alpha}{2}} \sqrt{Gh_j P} s_j + n_0, \quad (6.2)$$

where r_u is the distance between the user and its serving RRH, r_j is the distance between the user and the j^{th} interfering RRH, and $n_0 \in \mathbb{C}$ is the Additive White Gaussian Noise (AWGN) at the receiver denoted as $n_0 \sim \mathcal{CN}(0, \sigma_n^2)$. From (6.2), the Signal-to-Interference-plus-Noise-Ratio (SINR) is calculated as,

$$\text{SINR}_u = \frac{h_u g(r_u) P}{\sum_{j \neq u, j \in \mathcal{A}} h_j g(r_j) P + \sigma_n^2}, \quad (6.3)$$

where σ_n^2 is the power of the noise and $g(r) = Gr^{-\alpha}$. Outage happens if the received SINR falls below a given threshold γ and the user is covered if $\text{SINR}_u > \gamma$. The relationship between the outage probability (P_{out}) and the coverage probability (P_{cov}) is given by,

$$P_{\text{cov}} = 1 - P_{\text{out}} = \Pr(\text{SINR}_u > \gamma). \quad (6.4)$$

The average throughput of each active RRH, denoted as R , is given by,

$$R = B \mathbb{E} [\log_2(1 + \text{SINR}_u)], \quad (6.5)$$

where $\mathbb{E}[\cdot]$ denotes the expectation value. We also define the user throughput as the average throughput per user, given by,

$$R_u(t) = B_u(t) \mathbb{E} [\log_2(1 + \text{SINR}_u)]. \quad (6.6)$$

6.2.1 RRH and Transport Network Power Consumption Model

Since in C-RAN the BSs are decoupled into RRHs and VBSs, we divide the network power consumption into two parts: (i) RRH and transport network power consumption and (ii) VBS pool

power consumption. To model the power consumption of a RRH, we consider the linear power model as in [75],

$$P_{rrh} = \begin{cases} P_{rrh}^a + \frac{1}{\eta}P & \text{if } P > 0 \\ P_{rrh}^s & \text{if } P = 0 \end{cases}, \quad (6.7)$$

where P_{rrh}^a is the active circuit power consumption, η is the power amplifier efficiency, P is the transmission power, and P_{rrh}^s is the RRH power consumption in the sleep mode.

Since the data transmitted between the RRHs and VBS pool is oversampled real-time I/Q digital data streams in the order of Gbps, the transport network power consumption has a significant impact on the network power consumption. We consider the future Passive Optical Network (PON) to provide the low-cost, high-bandwidth, low-latency connections between the RRHs and VBS pool [70]. PON comprises an Optical Line Terminal (OLT) that resides in the VBS pool and connects a set of associated Optical Network Units (ONUs) through a single fiber. Implementing sleep mode at ONUs is a promising power-saving solution in PON; however, OLT can not go into the sleep mode and its power consumption is fixed [70]. We consider *fast/cyclic sleep* mode where the ONU state alternates between the active state (when the RRH is in the active state) and the sleep state (when the RRH is in the sleep state). Hence, the power consumption of the transport network is given as in [70],

$$P_{tn} = P_{olt} + P_{onu}, \quad (6.8)$$

where P_{olt} is the OLT power consumption in the VBS pool and P_{onu} is the ONU power consumption, given as,

$$P_{onu} = |\mathcal{A}| P_{ul}^a + |\mathcal{Z}| P_{ul}^s, \quad (6.9)$$

where P_{ul}^a and P_{ul}^s are the consumed power by each ONU in the active and sleep mode, respectively. Since P_{olt} is consumed in the VBS pool, we consider it in the power consumption of the VBS pool. Therefore, the area RRH and transport network power consumption is given by,

$$\mathcal{P}_{area} = \lambda_r^a(t)(P_{rrh}^a + \frac{1}{\eta}P + P_{ul}^a) + \lambda_r^s(t)(P_{rrh}^s + P_{ul}^s). \quad (6.10)$$

6.2.2 VBS Pool Power Consumption Model

In order to model the power consumption of the VBS pool, we introduce the notion of *size of a VM*, which is represented in terms of its processing power [CPU cycles per second], memory and storage capacity [Bytes], and network interface speed [bps]. It primarily depends on the number of users and type of data traffic (per-user capacity requirements) as well as on the computational complexity and memory footprint of the signal processing algorithms at the PHY layer, and of the scheduling and frame processing algorithms at the MAC layer. As it is discussed in [76], compared to other system resources, the CPU consumes the main part of the power in the VBS pool, and hence in this work we focus on minimizing its power consumption. There is also a linear power-to-frequency relationship for a server and recent studies have shown that on average an idle server consumes approximately 70% of the power consumed by the server running at the full CPU speed [76]. Therefore, for each VM we consider the power model defined as,

$$P_{vm} = \Delta(t)P_{max}u(t) + \beta\Delta(t)P_{max}(1 - u(t)) + P_{olt}, \quad (6.11)$$

where $\Delta(t)$ is the size of the VM in terms of CPU cycles per second, P_{max} is the maximum power consumed per unit VM size when the server is fully utilized, β is the fraction of power consumed by the idle VM, and $u(t)$ is VM utilization. Note that in our model $\Delta(t)$ and $u(t)$ change over time due to the workload variation and hence they are functions of time.

6.2.3 Clustering the VBSs and RRHs

We introduce the idea of *VBS-Cluster*, where i) all the VBSs associated with a certain cluster are merged into a unit VM and ii) the RRHs' antennas in each cluster act as a single coherent antenna array distributed over the cluster region. Since in the C-RAN architecture the VBSs are implemented on VMs, the size of VBS-Clusters can be changed based on the network requirements and capacity demand. *Moreover, merging the VBSs of the neighboring RRHs into a unit VBS-Cluster allows for smooth transition and greater optimization in the ensuing VM allocation procedure. Since each VBS has a minimum power consumption, it also abstracts the minimum power consumption of different VBSs into one VM.* In the following section we explain how we use the concept of VBS-Cluster to minimize the overall power consumption.

6.3 Elastic-Net: Demand-Aware Provisioning

The number of active users at different locations varies depending on the time of the day and week. For instance, in traditional cellular system during a day the BSs in downtown office areas are the busiest; whereas at night (or non-working hours) the BSs in residential or entertainment areas are the busiest (see Fig. 6.1). Today, each BS's spectrum and computing resources are only used by the active users in that BS's cell. So, deploying small cells for the peak traffic time (i.e., worst case) leads to grossly under-utilized BSs in some areas/times and is highly energy inefficient; and conversely, deploying for the average leads to oversubscribed BSs in some areas/times. On the other hand, since the traffic fluctuates over time, *there is no fixed cell size and transmission power that optimize the energy consumption.*

Due to the aforementioned facts, the use of small cells is quite efficient in terms of power consumption as well as utilization of spectrum and computing resources when the capacity demand is high and evenly distributed in space; however, it becomes less so when the data traffic is low and/or uneven due to the static resource provisioning and BSs' fixed power consumption. This means that *deploying small cells will make the network energy inefficient due to the unavoidable energy costs when the capacity demand is low.* For instance, the circuitry, paging channel, cooling system, backhaul, and power amplifiers all consume power so that even in a non-operational mode, BSs would consume a considerable amount of energy [77]. Moreover, in traditional cellular network, the cell planning and optimization, mobility handling, resource management, signal processing, and coverage are all done by each BS uniformly. In this case, even if the BSs have no traffic, they cannot be turned off [34].

Conversely, *by decoupling BSs into VBS and RRH in C-RAN architecture, the latter would only be responsible to provide spectrum resources and can be dynamically turned on and off based on the traffic demand and also the size of VBSs can be changed dynamically accordingly.* So, to address the problem of tidal effect, we take advantage of C-RAN characteristic and propose a dynamic provisioning approach, called "Elastic-Net", aimed at increasing the energy efficiency and resource utilization while providing a high level of Quality of Service (QoS).

In the proposed solution, as shown in Fig. 6.1, we cluster the neighboring RRHs and their

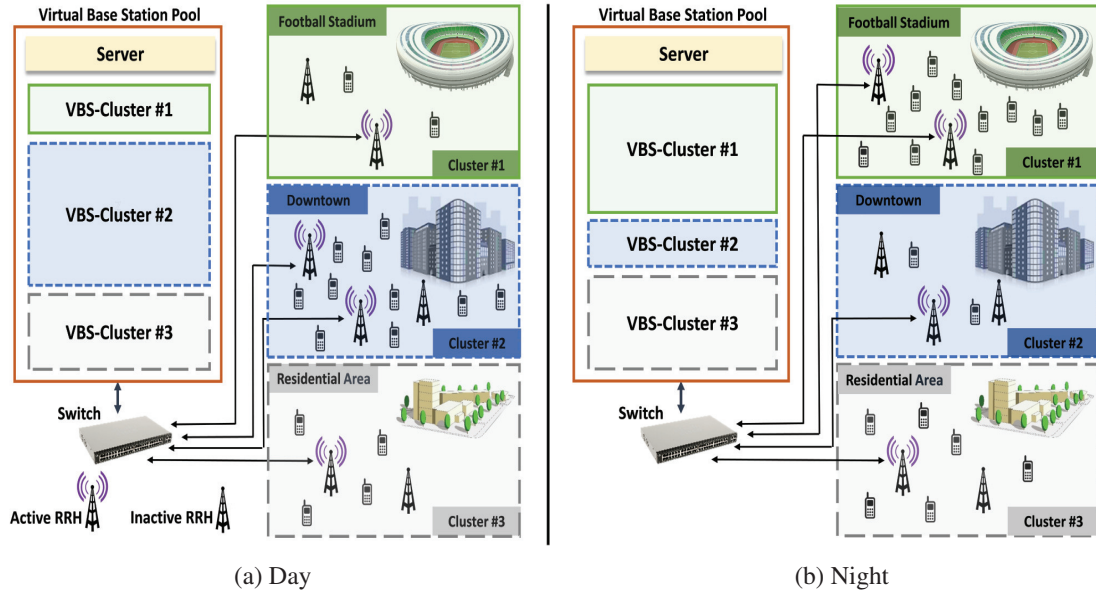


Figure 6.1: The use of virtualization in C-RAN allows dynamic re-provisioning of spectrum and computing resources (visualized here using different sizes) to the VBSs based on demand fluctuation; (a) and (b) illustrate the movement of mobile network load from the downtown office area to the residential and recreational areas over the course of a day and the corresponding changes in active RRH density and VBS size (we have used different icons for active RRH and inactive RRH).

corresponding VBSs based on traffic model, and in each cluster we adapt the system parameters accordingly. We advocate *demand-aware resource provisioning* where in each cluster the active RRH density, transmission power, and size of the VM are dynamically changed over time to minimize the power consumption and meet the fluctuating traffic demand and network constraints. For instance, as shown in Fig. 6.1, due to the higher capacity demand during day time in cluster #2 (Fig. 6.1(a)), we provision it with more active RRH and higher size of VBS-Cluster than those in night time (Fig. 6.1(b)) when the capacity demand is lower. Hence, the objective of this chapter is to obtain the optimal active RRH density, transmission power, and size of VM for each cluster so that the power consumption is minimized while meeting a predefined coverage probability, per-user data rate, and subframe processing time. To this end, we formulate the optimization problem for the i^{th} cluster as,

$$\mathbf{p} : \underset{\mu_a, P, \Delta}{\text{argmin}} \quad \mathcal{P}_{area}^i(\mu_a(t, i), P(t, i)) + P_{vm}^i(\Delta(t, i)) \quad (6.12a)$$

$$\text{subject to} \quad P_{cov} \geq \varepsilon P_{cov}^\infty, \quad (6.12b)$$

$$R_u(t) \geq R_0, \quad (6.12c)$$

$$T_{dl} \geq T_{fr}, \quad (6.12d)$$

where $\mathcal{P}_{area}^i(\mu_a(t, i), P(t, i))$ and $P_{vm}^i(\Delta(t, i))$ are the area power consumption and VBS-Cluster power consumption of the i^{th} cluster, respectively. P_{cov}^∞ is the coverage probability at no noise regime, R_0 is the per-user minimum data rate, T_{fr} is the subframe processing time, T_{dl} is subframe deadline, and ε is a positive number ranging from 0 to 1 ($0 < \varepsilon < 1$). Additionally, $\mu_a(t, i)$, $P(t, i)$, and $\Delta(t, i)$ are the RRH activity factor, transmission power, and size of the VM for the i^{th} cluster, respectively. Note that due to the temporal variation of traffic demand in each cluster, $\mu_a(t, i)$, $P(t, i)$, and $\Delta(t, i)$ are time-dependent and the optimal solution $[\mu_a^*(t, i), P^*(t, i), \Delta^*(t, i)]$ varies over the time.

The density of active and inactive RRHs in the i^{th} cluster can be written as,

$$\lambda_r^a(t, i) = \mu_a(t, i) \lambda_r(i), \quad (6.13a)$$

$$\lambda_r^s(t, i) = (1 - \mu_a(t, i)) \lambda_r(i), \quad (6.13b)$$

where $\lambda_r(i)$ is the density of all RRHs in the i^{th} cluster. By substituting (6.13a) and (6.13b) into (6.10), we can write,

$$\mathcal{P}_i(P(t, i), \mu_a(t, i)) = \lambda_r(i) (\mu_a(t, i) Q_1(t, i) + Q_2), \quad (6.14)$$

where

$$Q_1(t, i) = P_{rrh}^a + \frac{1}{\eta} P(t, i) + P_{tl}^a - P_{rrh}^s - P_{tl}^s, \quad (6.15a)$$

$$Q_2 = P_{rrh}^s + P_{tl}^s. \quad (6.15b)$$

From (6.14) and (6.15a), we can see that our objective function is non-convex because of the multiplication term of $\mu_a(t, i)$ and $P(t, i)$. However, in this case to minimize the objective function, as it is explained in [78], we can use the coordinate descent algorithm and minimize $\mu_a(t, i)$, $P(t, i)$, and $\Delta(t, i)$ independently, such that the constraints are met.

6.4 Optimal Active RRH Density and Transmission Power

In this section, we derive the optimal active RRH density and transmission power based on user density and per-user capacity demand. For this purpose, first we minimize the active RRH density such that the average throughput per user is greater than R_0 . Then, given the optimal RRH density, we minimize the transmission power to assure that the coverage probability is greater than its threshold.

Lemma 2. *The minimum RRH activity factor for which the constraint $R_u \geq R_0$ is met is given by,*

$$\mu_a^*(t, i) = \frac{R_0 \lambda_u(t, i)}{B \lambda_r(i) \left[\log_2(1 + \gamma) + \gamma^{\frac{2}{\alpha}} \mathcal{A}(\alpha, \gamma) \right]}, \quad (6.16)$$

where

$$\mathcal{A}(\alpha, \gamma) = \int_{\gamma}^{\infty} \frac{x^{-2/\alpha}}{1+x} dx. \quad (6.17)$$

Proof. The spectral efficiency achievable by a randomly chosen user when it is in coverage is given as in [79],

$$\tau(\alpha, \gamma) = \log_2(1 + \gamma) + \gamma^{\frac{2}{\alpha}} \mathcal{A}(\alpha, \gamma). \quad (6.18)$$

Hence, the per-user data rate in the i^{th} cluster and at time instant t can be written as,

$$R_u(t, i) = \frac{B \mu_a(t, i) \lambda_r(i)}{\lambda_u(t, i)} \left[\log_2(1 + \gamma) + \gamma^{\frac{2}{\alpha}} \mathcal{A}(\alpha, \gamma) \right]. \quad (6.19)$$

So, considering the constraint (6.12c) we can write,

$$\mu_a(t, i) \geq \frac{R_0 \lambda_u(t, i)}{B \lambda_r(i) \left[\log_2(1 + \gamma) + \gamma^{\frac{2}{\alpha}} \mathcal{A}(\alpha, \gamma) \right]}, \quad (6.20)$$

which establishes the minimum RRH activity factor as a function of $\lambda_u(t, i)$ to satisfy per-user data

rate constraint. \square

Once we obtain the minimum active RRH density, we need to minimize the transmission power of each cluster based on its active RRH density. Both coverage and outage probability highly depend on the density and transmission power of the active RRHs. This means that, given a fixed active RRH density, we can minimize the transmit power of the active RRHs so to achieve a certain coverage and outage probability. Since in our solution the active RRH density of different clusters changes over time based on the traffic demand, we need to also dynamically optimize the transmit power accordingly. This can further decrease the power consumption of the system. For instance, when the density of active RRHs becomes higher, each RRH has only a small coverage area and users can be in coverage even with a lower transmission power.

Lemma 3. *The minimum transmission power for which the constraint $P_{\text{cov}} \geq \varepsilon P_{\text{cov}}^\infty$ is met is given by,*

$$P_c^*(t, i) = \frac{L_1}{[\mu_a(t, i) \lambda_r(i)]^{\frac{\alpha}{2}}}, \quad (6.21)$$

where

$$L_1 = \frac{\gamma \sigma^2 \Gamma\left(\frac{\alpha}{2} + 1\right)}{\pi^{\frac{\alpha}{2}} [1 + \Upsilon(\gamma, \alpha)]^{\frac{\alpha}{2}} (1 - \varepsilon)}, \quad (6.22a)$$

$$\Upsilon(\gamma, \alpha) = \gamma^{\frac{2}{\alpha}} \int_0^\infty \frac{1}{1 + z^{\frac{\alpha}{2}}} dz. \quad (6.22b)$$

Proof. The coverage probability in the i^{th} cluster is given as [80],

$$P_{\text{cov}}(\alpha, \gamma, \mu_a) = \pi \mu_a(t, i) \lambda_r(i) \times \int_0^\infty e^{-\pi \mu_a(t, i) \lambda_r(i) (1 + \Upsilon(\alpha, \gamma)) - \gamma \sigma^2 v^{\alpha/2} P^{-1}} dv. \quad (6.23)$$

Now, by using the substitution $\gamma \sigma^2 P^{-1} \rightarrow s$ in (6.23) and the approximation $e^{-sv^{\alpha/2}} \approx (1 - sv^{\alpha/2})$ (in the case of low noise regimes $\sigma_n^2 \rightarrow 0$), we can write,

$$P_{\text{cov}}(\alpha, \gamma, \mu_a) \approx P^\infty \left(1 - \frac{\gamma \sigma^2 \Gamma\left(\frac{\alpha}{2} + 1\right)}{P [\pi \mu_a(t, i) \lambda_r(i) (1 + \Upsilon(\alpha, \gamma))]^{\frac{\alpha}{2}}} \right), \quad (6.24)$$

where P^∞ is the coverage probability without noise [80],

$$P^\infty = (1 + \Upsilon(\alpha, \gamma))^{-1}, \quad (6.25)$$

and $\Gamma(x) = \int_0^\infty t^{x-1} e^{-t} dt$ is the standard gamma function. Then, the minimum transmission power $P_c^*(t, i)$ that satisfies the coverage constraints can be obtained by combining (6.24) and (6.12b). \square

6.5 Computational Characteristics of a Virtual Base Station and Optimal VM Size

In order to minimize the computing resource consumption of a VM hosting the VBS-Cluster, we need to characterize the computational requirements of the corresponding VBS-Cluster in terms of traffic load and number of users in order to provide adequate processing capabilities that ensure the subframe processing time. In other words, resource provisioning of the VBS-Clusters must be done in such a way that the subframe processing time is less than the subframe deadline. Software implementation coupled with real-hardware experiments is essential to understand the runtime complexity as well as performance limits of VBS-Cluster. The realization of the C-RAN emulation testbed on virtualized general-purpose computing servers allows for profiling of the computational complexity of the different communication functionalities implemented in software. In particular, such profiling results provide a “mapping” between traffic load and required computing resources. Here, we present our testbed experiments and the empirical models that we have established for estimation of processing time and CPU utilization.

6.5.1 Emulation Platform and Testbed Architecture

We choose an open-source software implementation of LTE standard called OpenAirInterface (OAI) developed by EUROCOM to realize the virtualized C-RAN system [81]. OAI can be used to build and customize mobile network operators consisting of eNBs and Commercial Off-The-Shelf (COTS) UEs as well as software-defined UEs. The structure of OAI mainly consists of two components: one part, called Openairinterface5g, is used for building and running eNB units; the other part, called Openair-cn, is responsible for building and running the Evolved Packet Core (EPC) networks, as shown in Fig. 6.2. The Openair-cn component provides a programmable environment to implement and manage the following network elements: Mobility Management Entity (MME), Home Subscriber Server (HSS), Serving Gateway (S-GW), and PDN Gateway (P-GW).

Figure 6.3 illustrates the architecture of our testbed. The RRH front-ends of the C-RAN testbed

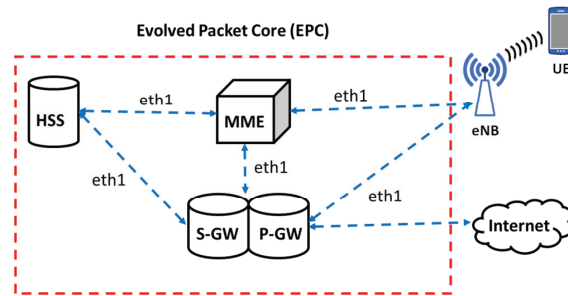


Figure 6.2: Evolved Packet Core (EPC) network topology diagram.

are implemented using SDR USRP B210s, each supporting 2×2 MIMO with sample rate up to 62 MS/s. In addition, each RRH is equipped with a GPSDO module for precise synchronization. Each instance of the VBS is implemented using the OAI LTE stack, which is hosted in a VMware VM. All the RRHs are connected to the VBS pool (the physical servers hosting the VMs) via USB 3 connections. The Ubuntu 14.04 LTS with kernel 3.19.0-91-lowlatency is used for both host and guest operating systems. In order to achieve a high performance for our testbed, all power-management features in the BIOS, C-states, and CPU frequency scaling have been turned off. The CPU should support the sse3 and sse4.1 features. These flags must be exposed from the host to the guest, and can be checked by using the command `cat /proc/cpuinfo|grep flags|uniq`. For the physical server hosting the VMs, we use a Dell Precision T5810 workstation with Intel Xeon CPU E5-1650, 12-core at 3.5 GHz, and 32 GB RAM.

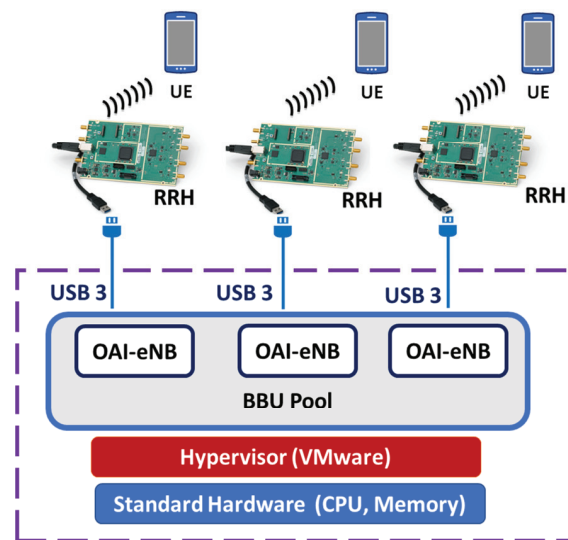


Figure 6.3: Logical illustration of C-RAN testbed architecture.

6.5.2 Monitoring the OAI eNB and the UE

As illustrated in Fig. 6.4, our C-RAN experimental testbed consists of one unit of UE and one unit of eNB, both implemented using the USRP B210 boards and running on OAI. The OAI software instances of the eNB and UE run in separate Linux-based Intel x86-64 machines comprising of 4 cores for UE and 12 cores for eNB, respectively, with Intel i7 processor core at 3.6 GHz. OAI comes with useful monitoring tools such as network protocol analyzers, loggers, performance profilers, timing analyzers, and command line interfaces for performing the intended measurements and monitoring of the network. The main configuration parameters are summarized in Table 6.1. In particular, the eNB is configured in band 7 (FDD) and the transmission bandwidth can be set to 5, 10, and 20 MHz, corresponding to 25, 50, and 100 Physical Resource Blocks (PRBs), respectively.

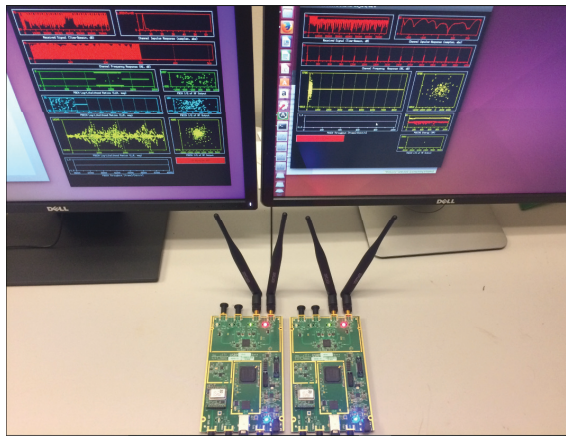


Figure 6.4: C-RAN testbed implementation utilizing OAI.

Table 6.1: Testbed Configuration Parameters

Parameters	eNB	UE
Duplexing mode	FDD	FDD
Frequency	2.66 GHz	2.66 GHz
Transmitted power	[150 ÷ 170] dBm	[150 ÷ 170] dBm
MCS	[0 ÷ 27]	[0 ÷ 27]
Mobility	Static	Static
PRB	25, 50, 100	25, 50, 100
Radiation pattern	Isotropic	Isotropic

6.5.3 Processing Time of LTE Subframes

Here, we study the processing time of a VBS for each LTE subframe with respect to different CPU frequency configurations in the VMware environment. The execution time of each signal processing module in the downlink is measured using *timestamps* at the beginning and at the end of each subframe. OAI uses the RDTSC instruction implemented on all x86 and x64 processors as of the Pentium processors to achieve precise timestamps [82]. The *cpupower* tool in Linux is used to control the available CPU frequencies. To avoid significant delay and to not miss the synchronization between eNB and UE hardware, we recommend to run the experiment within a $2.8 \div 3.5$ GHz CPU frequency range.

In Fig. 6.5, we illustrate the processing time of the eNB given different CPU-frequency steps, in which the Modulation and Coding Scheme (MCS) index is set to 27 for both UL and DL. It can be seen that the processing time dramatically decreases when the CPU frequency increases. To model the subframe processing time against the CPU frequency and radio-resource configuration, we repeat the experiment in Fig. 6.5 with different MCS indexes. The subframe processing time $T_{\text{fr}} [\mu\text{s}]$ can be well approximated as,

$$T_{\text{fr}} [\mu\text{s}] = \frac{\alpha_{\text{PRB}}}{\omega N_c} + \beta_{\text{MCS}} + 2.508, \quad (6.26)$$

where N_c is the number of CPU cores, ω is the CPU speed per each core measured in GHz, and α_{PRB} and β_{MCS} are two parameters that depend on the values of PRB and MCS, respectively. Table 6.2 describes how α_{PRB} and β_{MCS} are related to PRB and MCS.

Table 6.2: Values of parameters α_{PRB} and β_{MCS} .

PRB	25	50	100			
α_{PRB}	900	940	970			
MCS	0	9	10	16	24	27
$\beta_{\text{MCS}} [\mu\text{s}]$	0	9.7	11.8	37.5	64.8	75

6.5.4 CPU Utilization

In C-RAN, it is of critical importance to understand the CPU utilization of the VBS in order to design efficient resource provisioning and allocation schemes. In the previous subsections, we

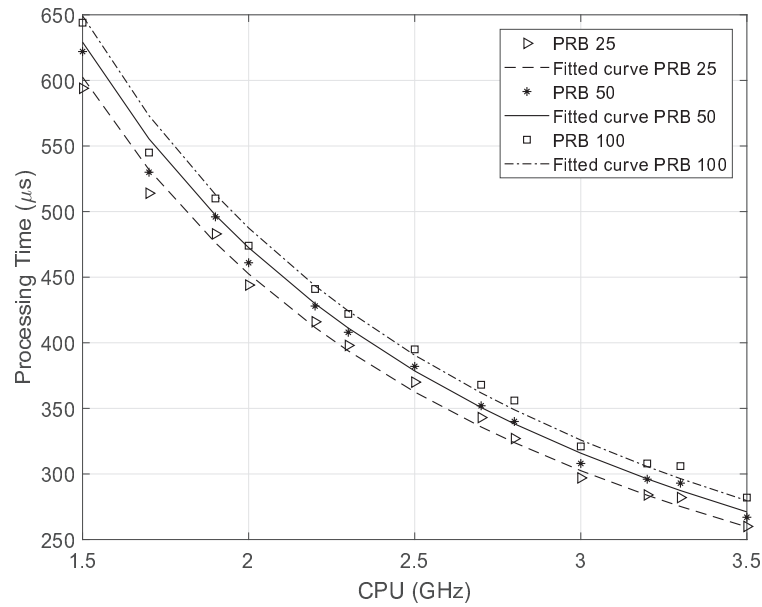


Figure 6.5: Processing time of LTE subframes against CPU frequency with MCS = 27 and various PRB allocations.

have seen the relationship between MCS and CPU usage for different values of PRBs. In this experiment, the CPU utilization percentage is calculated using the top command in Linux, which is widely used to display processor activities as well as various tasks managed by the kernel in real time. We repeatedly send UDP traffic from the eNB to the UE with various MCS and PRB settings. The CPU utilization percentage has been recorded as in Fig. 6.6. By setting the CPU frequency of the OAI eNB to 3.5 GHz, we have seen that the highest CPU consumption occurred at MCS 27, corresponding to 72%, 80%, and 88% when PRBs are 25, 50, and 100, respectively. We can conclude that the total processing time and computing resources were mainly spent on the modulation, demodulation, coding, and decoding. These tasks played the bigger roles in terms of complexity and runtime overhead in the BBU protocol stack of the VBS.

To understand better the VBS computational consumption in C-RAN with respect to the users' traffic demand, we will now establish the relationship between the DL throughput and the percentage of CPU usage at the VBS. To begin, we learn that OAI supports 28 different MCSs with index ranging from 0 to 27. In the downlink direction, MCSs with the index 0 to 9 are modulated using QPSK, index 10 to 16 are modulated using 16-QAM, and the rest are based on 64-QAM. For instance, in LTE FDD system with PRB 100, corresponding to bandwidth of 20 MHz, we can get $12 \times 7 \times 2 = 168$ symbols per ms, in case of normal Cyclic Prefix (CP), which is equivalent to a

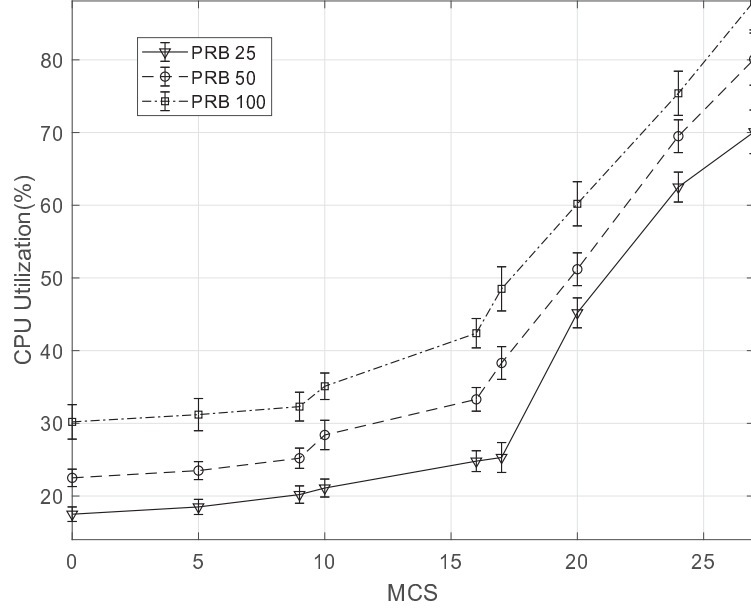


Figure 6.6: CPU utilization of the VBS at different values of MCS and PRB.

data rate of 16.8 Mbps [83]. Based on the MCS index used in each experiment, we can calculate the corresponding DL throughput by multiplying the bit rate by the number of bits in the modulation scheme.

Figure 6.7 shows the CPU utilization percentage at the VBS corresponding to different DL throughputs. Using the calculated results, we have fitted the CPU utilization as a linear function of the DL throughput as,

$$\text{CPU} [\%] = 0.6237R_0 + 21.3544, \quad (6.27)$$

where R_0 is the throughput measured in Mbps.

6.5.5 Optimal Size of VM

Power consumption of a VM is mostly determined by the CPU, memory, and storage capacity. In comparison to other system resources, the CPU consumes the main part of energy, and hence in this work we focus on minimizing its power consumption. We can recast the power consumption of the i^{th} VBS-Cluster as,

$$P_{vm}^i = \Delta(t, i) P_{\max} u(t, i) (1 - \beta) + \beta \Delta(t, i) P_{\max} + P_{olt}, \quad (6.28)$$

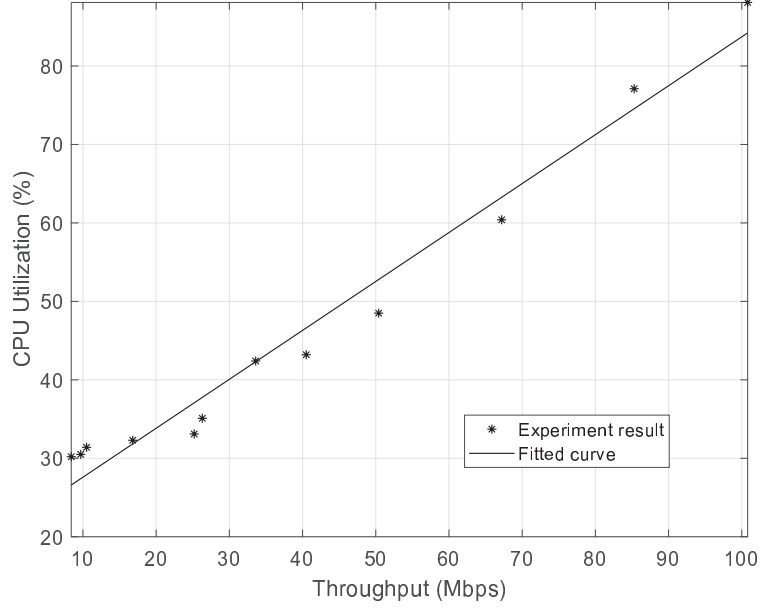


Figure 6.7: Percentage of CPU usage versus the downlink throughput.

where for a given workload, $u(t, i)$ is inversely proportional to $\Delta(t, i)$ [84]. So, to minimize the power consumption of the VM, we need to minimize the size of the VM (CPU cores) such that the network requirements are met.

The effective data rate is highly controlled by MCS index and number of PRBs. So, the workload in the VBS-Cluster depends on the MCS index, number of PRBs, and the channel bandwidth [82]. Moreover, according to [85], the Round Trip Time (RTT) between RRH and VBS pool cannot exceed $400\mu s$. Since the total delay budget in LTE is considered as $3ms$, this leaves the VBS-Cluster only around $2.6ms$ for signal processing at VBS pool. Hence, once the VBS-Cluster receives a subframe from the RRH, there is a hard deadline $\leq 3ms$ for subframe processing depending on the distance between the RRH and VBS pool. The required CPU speed (VM size) for a given number of PRBs, MCS index, and subframe processing time can be derived from Eq. (6.26) as,

$$\Delta(t, i) = N_c(t, i)\omega = \frac{\alpha_{PRB}}{T_{fr} - \beta_{MCS} - 2.508}, \quad (6.29)$$

where T_{fr} is the processing time and is measured in μs , α_{PRB} is a PRB dependent constant, β_{MCS} is a MCS dependent constant, $N_c(t, i)$ is the number of dedicated CPU cores to the i^{th} VBS-Cluster at time t , and ω is the CPU speed measured in GHz. Hence, the minimum number of required CPU

cores to meet the subframe deadline is given by,

$$N_c^*(t, i) = \left\lceil \frac{\alpha_{\text{PRB}}}{\omega (T_{\text{dl}} - \beta_{\text{MCS}} - 2.508)} \right\rceil, \quad (6.30)$$

where T_{dl} is the subframe deadline.

6.6 Performance Evaluation

In this section, we provide a range of simulations and real-time emulations to evaluate the performance of our proposed solution. In the simulations, we consider a cellular network where the RRHs and the users are distributed according to two independent homogeneous PPPs. Table 6.3 lists the stimulation parameters used during our experiments.

Table 6.3: Simulation Parameters.

Parameters	Mode/Value
Cellular Layout	Poisson Point Process
Channel Model	Path Loss and Shadowing
Channel Bandwidth	20 MHz
Number of Antennas (N_{TX}, N_{RX})	(1, 1)
OLT power consumption (P_{olt})	20 W
ONU Power Consumption in Active Mode (P_{oi}^a)	4 W
ONU Power Consumption in Sleep Mode (P_{oi}^s)	0.5 W
RRH Circuit Power Consumption in Active Mode (P_{rrh}^a)	12.4 W
RRH power consumption in sleep mode (P_{rrh}^s)	3.5 W
Power Amplifier Efficiency (η)	0.32
MSC Dependent Constant (α)	117.4
Fraction of Power Consumed by Idle VBS (β)	0.7
Fraction of Minimum Coverage Probability (ε)	0.75
Minimum Data Rate (R_0)	200 Kbps

6.6.1 Simulation Results

In the first simulation, we compare the active RRH density in terms of the minimum transmission power for different environments. As shown in Fig. 6.8, with increasing the active RRH density the minimum transmission power decreases. For instance, for $\alpha = 4$ by increasing the active RRH density from $10^{-4}/m^2$ to $10^{-3}/m^2$, we have almost 10 dBm decrease in minimum transmission power. This is because with increasing the density of active RRHs, the coverage area of each RRH becomes smaller and so we can exploit a lower transmission power while guaranteeing the same coverage probability.

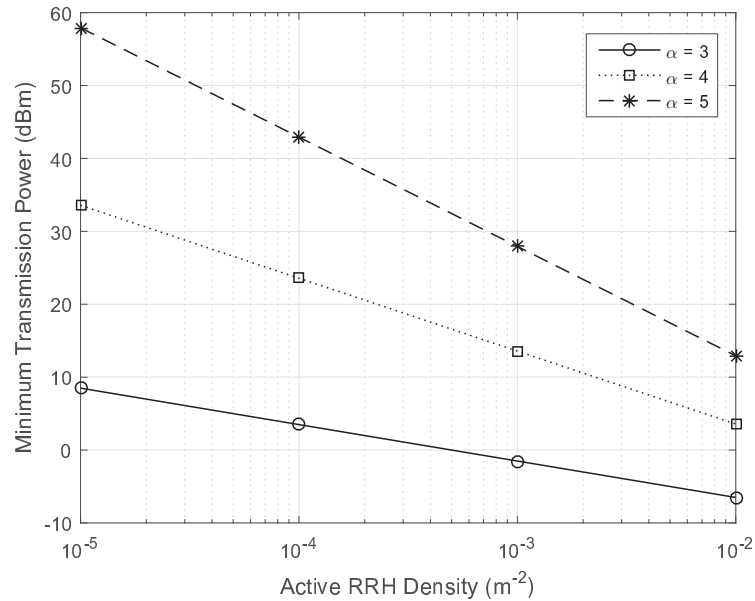


Figure 6.8: Minimum transmission power as a function of active RRH density ($\gamma = 10$ dB and $\sigma^2 = \lambda_r^a \times 10^{-4}$).

In the second simulation, we examine how different user densities affect the minimum transmission power. We have examined our simulation for different environments ($\alpha = 4, 5$) and SINR thresholds ($\gamma = 0, 15$ dB). As it is shown in Fig. 6.9, increasing the user density will result in a decrease in the minimum transmission power. The reason is that by higher user densities we require higher active RRH density and hence smaller cells. For instance, given $\alpha = 4$ and $\gamma = 0$ dB, we need a minimum transmission power of 34.96 dBm and 24.96 dBm for $\lambda_u = 10^{-3}$ and $\lambda_u = 10^{-2}$, respectively. In Fig. 6.10, we also compare the coverage probability as a function of SINR threshold for different environments. The curves all exhibit the basic shape and as one would expect, the coverage probability is higher for higher path loss exponents.

In the next simulation, we examine the performance of our solution in terms of area power consumption with respect to the active RRH density. In this experiment we only consider the coverage probability constraint and show how area power consumption changes with different active RRH densities. As shown in Fig. 6.11, for $\alpha = 3, 4, 5$, by increasing the active RRH density, the area power consumption increases. However, for $\alpha = 6$ the area power consumption first decreases and then increases. This is because for low active RRH densities the dominant term in area power consumption is transmission power, while for higher active RRH densities the dominant term becomes the circuit power consumption. In the other experiment, we explore the variation of active RRH

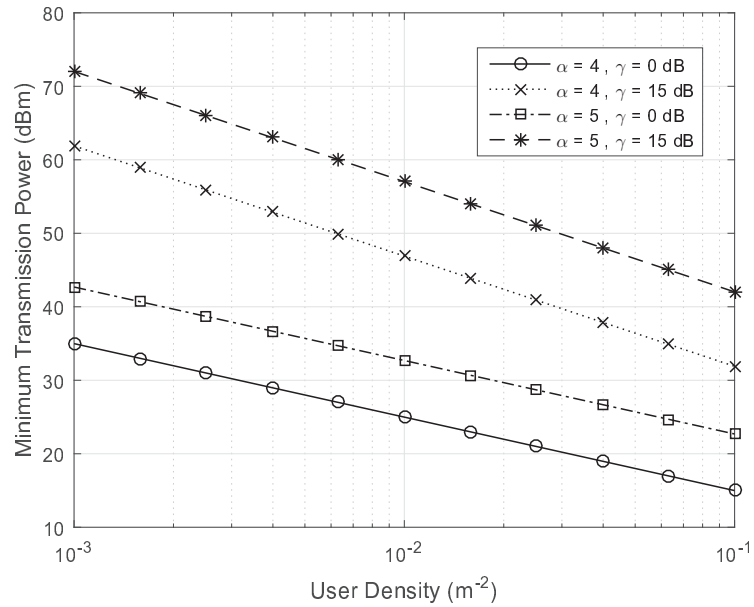


Figure 6.9: Minimum transmission power as a function of user density.

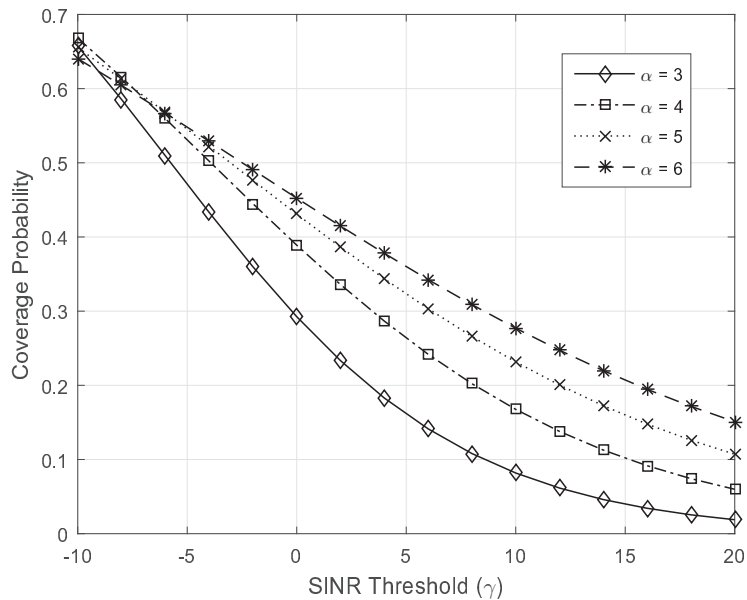


Figure 6.10: Coverage probability as a function of SINR threshold.

density for different active user densities. As the active user density increases, we need more active RRHs to provide service and data rate for the users and consequently the active RRH density needs to be increased. As shown in Fig. 6.12, active RRH density also depends on the path loss exponent and SINR threshold. As the threshold and the path loss exponent increases, we need less active RRHs to serve the users.

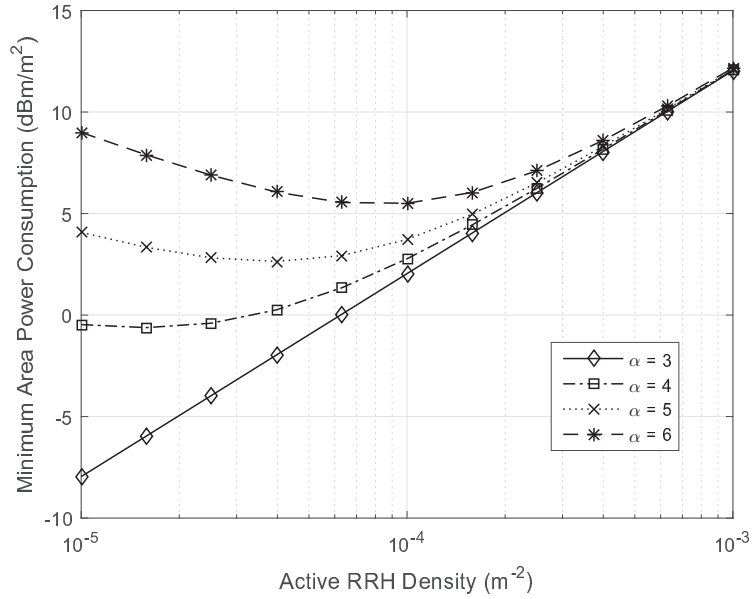


Figure 6.11: Area power consumption as a function of active RRH density.

In Fig. 6.13, the number of required CPU cores is investigated for different number of PRBs. As we mentioned in Sect. 6.5.5, resource provisioning for VBS-Clusters must be done such that the frame-processing time is less than the frame deadline. In order to minimize the power consumption and maximize the resource utilization we need to provision the VBS-Clusters with minimum CPU cores such that the frame-processing time is less than the frame deadline. With increasing the density of active RRHs and users more PRBs will be required and, consequently, more computing resources is needed. As shown in Fig. 6.13, for $T_{dt} = 3ms$ we need 5 CPU core of speed 1.5 GHz or 3 CPU cores of speed 3.3 GHz to process 180 PRBs.

6.6.2 Impact of Traffic Variation in Power Consumption

In the other simulation, we simulate the traffic fluctuation on a typical operational day and show how our solution dynamically adapts the RRH density, transmission power, and size of VBS-Clusters to meet such fluctuation. As shown in Fig. 6.1, we consider a network with 3 clusters where each cluster covers an area of 25 km² and has its own traffic and user density fluctuation. As shown in Fig. 6.14, clusters #1 and #2 (corresponding to the downtown and entertainment areas) have lower user density on early morning and late night, while cluster #3 (corresponding to the residential area) has higher user density at those times. Here, we will explore how “Elastic-Net” adapts the network

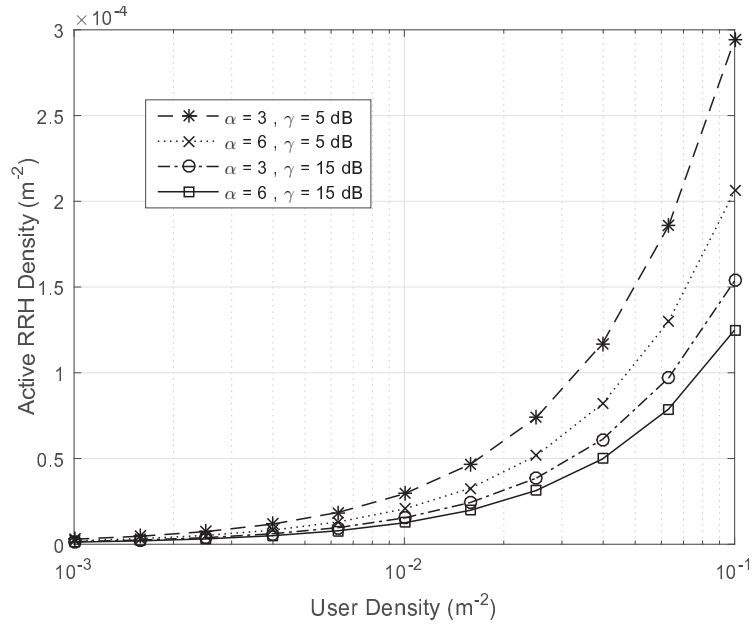


Figure 6.12: RRH activity factor as a function of user density.

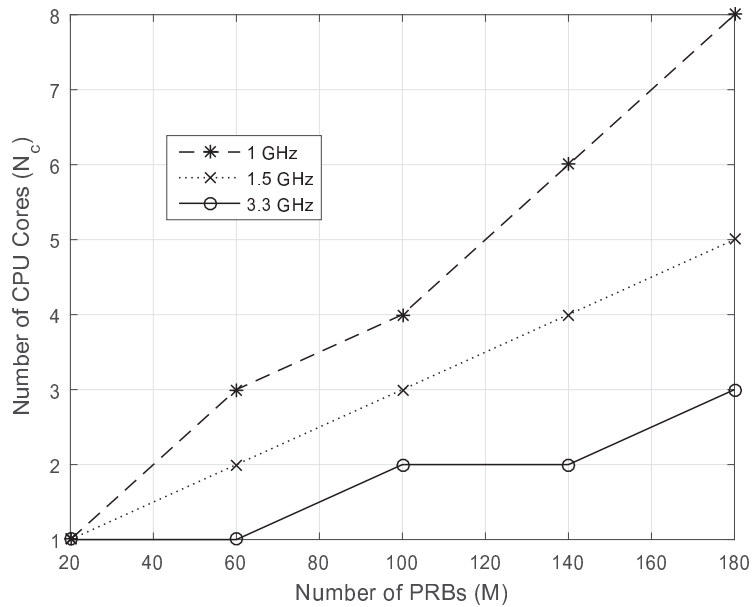


Figure 6.13: Minimum number of CPU cores for different number of PRBs ($\gamma = 10$ dB, and $\sigma^2 = \lambda_r^a \times 10^{-4}$).

parameters so to minimize the power consumption and maximize the resource utilization, while at the same time meeting the network constraints.

Figure 6.15 illustrates the minimum active RRH density adaptation required to serve the corresponding user density fluctuation in different clusters. As expected, the RRH density fluctuation

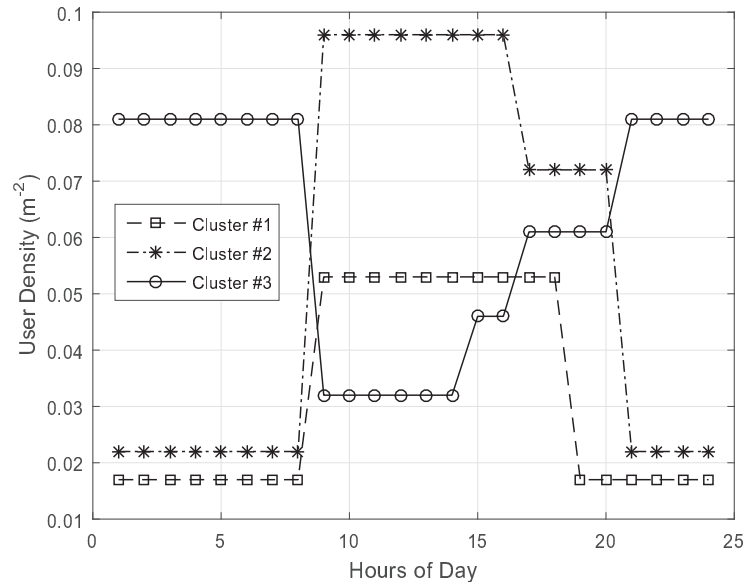


Figure 6.14: Traffic fluctuation on a typical operational day for three different clusters.

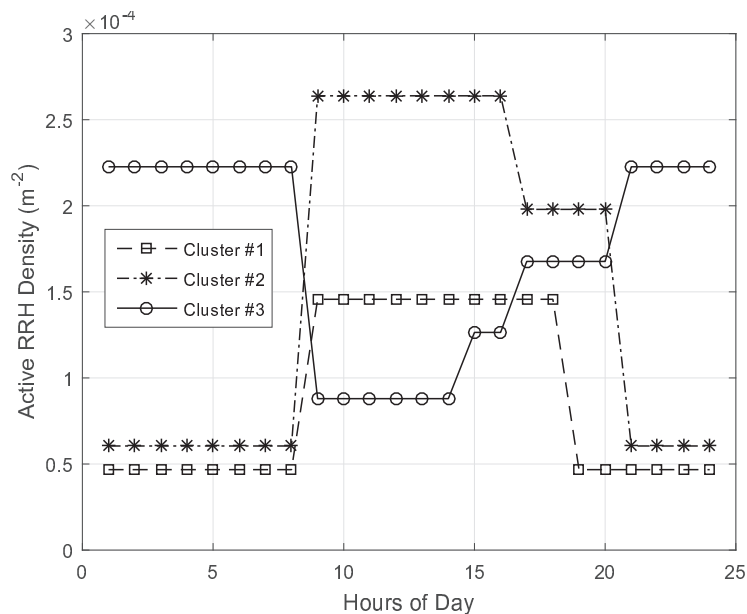


Figure 6.15: Fluctuation of active RRH density to meet the user fluctuation for different times of the day.

corresponds to the user density fluctuation. This means that for the high traffic demand times we need a higher number of active RRHs and smaller cells.

The time varying transmission power for different clusters is also shown in Fig. 6.16. It is clear that for the peak traffic times we need a lower transmission power than in low traffic times. This is because in the peak traffic times we have higher active RRH density and, consequently, the coverage

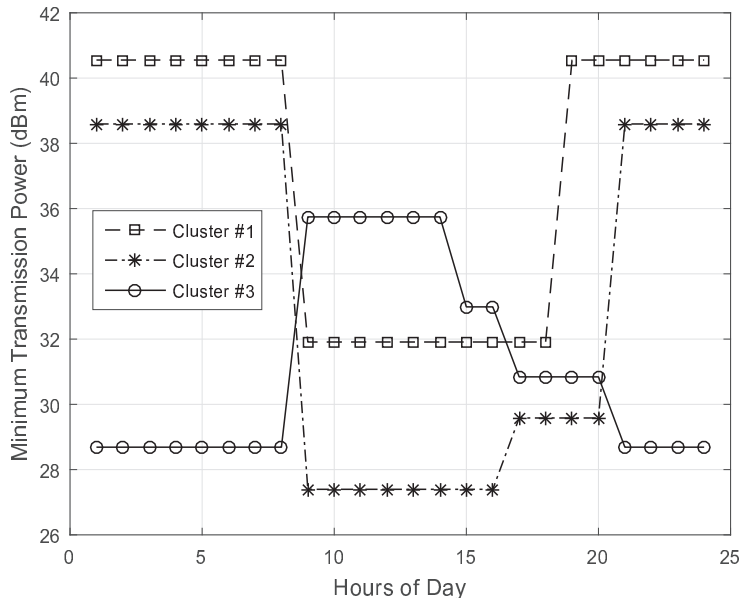


Figure 6.16: Fluctuation of minimum transmission power to reduce the power consumption while guaranteeing a predefined Quality of Service (QoS).

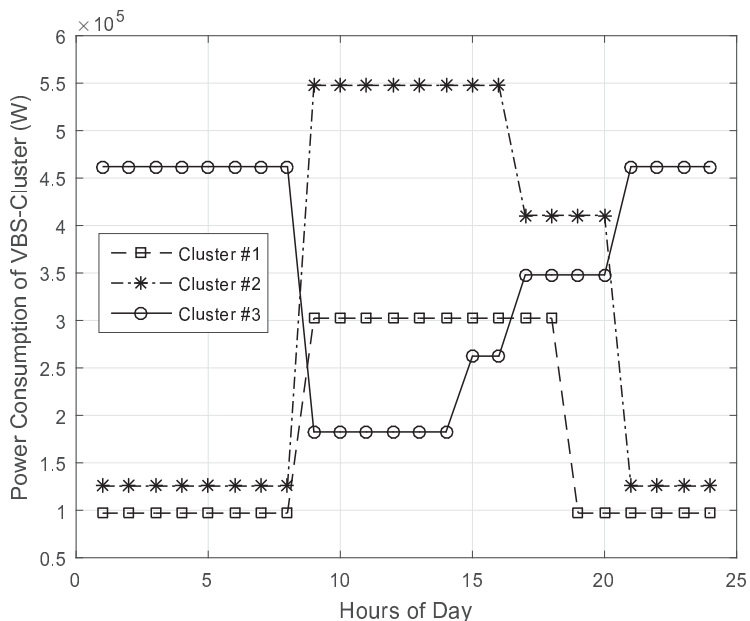


Figure 6.17: Power consumption of different VBS-Clusters (CPU speed = 3.3 GHz).

area of each RRH becomes smaller. For instance, the network decreases the transmission power of clusters #1 and #2 by 8.62 and 11.19 dBm, respectively, in the day time when the user density and traffic load is high. Figure 6.17 also shows the power consumption of VBS-Clusters in the VBS pool. In this simulation we used the power consumption model presented in Sect. 6.2.2 and

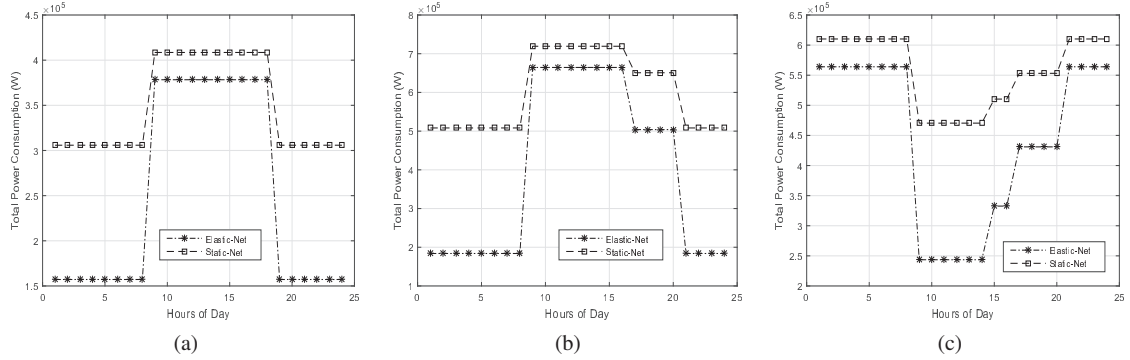


Figure 6.18: Comparison of power consumption between Elastic-Net (in C-RAN) and Static-Net (in D-RAN) for (a) Cluster #1, (b) Cluster #2, and (c) Cluster #3.

considered $P_{max} = 72$ W for each CPU core. As expected, since in the peak traffic times we need more CPU cores to provision the VBS-Clusters, we have a higher power consumption rather than in lower traffic times.

In Fig. 6.18, we also compare the traditional static provisioning against Elastic-Net. As shown in Figs. 6.18 (a), (b), and (c), depending on the traffic fluctuation there is a big difference between power consumption of Elastic-Net and Static-Net. For instance, in cluster # 1 and for low traffic times (7 PM - 8 AM) we have 48.59% decrease in power consumption by Elastic-Net. However, for the peak traffic times (8 AM - 7 PM), we have only 7.39% decrease in power consumption. This confirms our statements in Sect. 6.1 that the small cells is quite efficient when the capacity demand or user density is high and it becomes less so when the traffic demand is low.

6.6.3 Testbed Experiment Results

To show the benefits of our solution, we also designed an testbed experiment and considered two scenarios to compare the CPU power consumption of our solution under the C-RAN architecture against the traditional approach in D-RAN. In the first scenario, two traditional BSs on different VMs are considered in such a way that one is operated under heavy load while the other under light load. The heavy-loaded BS handles 6 concurrent calls and 100 text messages, whereas the light-loaded BS handles only a single call. Each BS is provisioned with 2 threads to process the data. In the second scenario, 2 VBSs on the same VM is considered under the same loads as described in the first scenario. In this case, since the processing resources are shared, we are able to adjust the BS provisioning. We provision the BS under heavy load with 3 threads and the BS under light load

with 1 thread. For the first scenario, the heavy and light load have an average CPU utilization of 77% and 10%, respectively, while for the second scenario the average CPU utilization is 57% and 19%.

Table 6.4 also shows that dynamic resource provisioning (proposed in Elastic-Net) decreases CPU power consumption for the same amount of traffic from 134.64 to 72.34 W. This 42.26% decrease is due to the fact that in the traditional D-RAN each BS needs to have its own dedicated processor while in C-RAN multiple VBSs can share computing resources and exploit multiplexing gain.

Table 6.4: Power usage, CPU utilization, and resource utilization for static (D-RAN) and dynamic provisioning (C-RAN).

Provisioning	Load	Power Usage	CPU Utilization	Resource Utilization
Static in D-RAN	Heavy	70.62 W	77.47%	1.23GB, 2 threads
	Light	64.02 W	10.13%	1.26GB, 2 threads
Elastic in C-RAN	Heavy	72.34 W	57.04%	1.13GB, 3 threads
	Light		18.58%	1.12GB, 1 threads

6.7 Discussion

We proposed and validated a novel demand-aware reconfigurable solution, named *Elastic-Net*, to minimize the power consumption of Cloud Radio Access Network (C-RAN). In the proposed solution, we introduced the idea of VBS-Cluster and partitioned the coverage region of the network into clusters based on traffic fluctuation. Then, in each cluster we optimized active RRH density, transmission power, and size of the VM based on the traffic demand and user density so that the network power consumption is minimized and the network constraints are met. We also characterized the computational requirements of a VBS through our programmable C-RAN testbed. For this purpose, we carried out different testbed experiments to investigate the computational requirements and utilization of a VBS. Simulation and testbed experiment results confirmed the validity of our analysis and showed the benefits of this novel solution. For instance, via the real-time testbed we showed that our idea of dynamic resource provisioning could reduce 42% of the CPU power consumption at the VBSs.

Chapter 7

Conclusions and Future Research Directions

Over the last few years, proliferation of personal mobile computing devices like tablets and smart-phones along with a plethora of data-intensive mobile applications has resulted in a tremendous increase in demand for ubiquitous and high data rate wireless communications. An estimated area capacity of 25 Gbps/km² is forecast for the 5G wireless cellular networks, which corresponds to a 100× boost over what the current 4G wireless standard is able to provide in terms of spectral efficiency. Additionally, the economy impact of power consumption is particularly dire in emerging markets and the next generation of cellular network must be not only spectral efficient but also energy efficient. Although several recent efforts have been done to reduce the power consumption of existing small cell networks, limited attention has been given to optimizing the overall network deployment. This means that the distributed nature of traditional cellular network does not allow for any further reduction in power consumption. Therefore, a novel design and architecture is necessary for the next generation of wireless cellular network to overcome the aforementioned challenges.

C-RAN is a new architecture for wireless cellular network where the processing resources of BSs are centralized in a BBU pool. The centralized characteristic of C-RAN allows for dynamic reconfiguration of computing and spectrum resources while keeping the cost of delivering services to the users low. Our goal was to leverage the characteristics of C-RAN architecture and design and develop techniques to increase the spectral and energy efficiency.

In order to achieve the aforementioned goal, we proposed four solutions, namely 1) Cloud-BSS, 2) DJP, 3) Cloud-CFFR, and 4) Elastic-Net. In Cloud-BSS, the performance of ICA algorithms is investigate under different topologies to cancel the intra-cluster interference. Since Cloud-BSS does not take any action to mitigate the inter-cluster interference, we proposed DJP to decrease both the intra- and inter-cluster interference. Moreover, in order to improve the performance of

Fractional Frequency Reuse (FFR), we proposed Cloud-CFFR which is able to reject the intra-cluster interference and decrease the inter-cluster interference. Finally, in order to increase the energy efficiency, we proposed Elastic-Net where the network parameters (i.e. active RRH density, transmission power, and VM size) are optimized and adapted based on the traffic fluctuation so that the power consumption is minimized while the resource utilization is maximized.

We have identified avenues for further research in the following areas:

Joint dynamic RRH selection and power minimization: Even though the Elastic-Net provides the active RRH density, the set of active RRHs should be found based on the positions of users. On the other words, we need to decide which RRH should be on/off so that the spectral efficiency and sum data-rate is maximized while the transmit power consumption of the active RRHs is minimized through coordinated beamforming.

Predictive models: Recently, there has been significant interest in studying how prediction can be used for proactive resource allocation and caching. In the proactive methods, the fluctuation in per-user capacity demand, user interest, and user mobility can be estimated. Then, provisioning of computational resources and cache placement can be done in advance for a limited horizon. This estimations are a result of knowledge of known patterns (e.g., day and night, weekdays and weekends, holidays, game schedules, etc.) or predictions based on advanced time series analysis of historical traffic traces from immediate as well as distant past.

Cooperative hierarchical caching: Our research group at the Rutgers Cyber-Physical Systems (CPS) Lab is working towards optimizing the content caching in C-RAN. In traditional content caching techniques, the storage capacity is only available at the edge of network beside the BSs. In C-RAN architecture, the cloud infrastructure at the BBU pool with strong computing resources and storage capacity now provides a central port for traffic offloading and content management to handle the growing Internet traffic from mobile users. So, the storage capacity in the cloud can improve the performance of cache placement techniques.

References

- [1] China Mobile Research Institute. C-RAN: The Road Towards Green RAN. *White Paper, ver 3*, 2014.
- [2] Cisco. Cisco visual networking index: Global mobile data traffic forecast update. *Cisco Public Information*, Feb. 2013.
- [3] Y. Lin, L. Shao, Z. Zhu, Q. Wang, and RK Sabhikhi. Wireless Network Cloud: Architecture and System Requirements. *IBM Journal of Research and Development*, 54(1):1–4, 2010.
- [4] V. Marojevic, I. Gomez, P.L. Gilabert, G. Montoro, and A. Gelonch. Resource management implications and strategies for sdr clouds. *Analog Integrated Circuits and Signal Processing*, 73(2):473–482, 2012.
- [5] A. Hajisami, H. Viswanathan, and D. Pompili. Cocktail Party in the Cloud: Blind Source Separation for Co-operative Cellular Communication in Cloud RAN. *IEEE International Conference on Mobile Ad hoc and Sensor Systems (MASS)*, pages 37–45, 2014.
- [6] A. Hajisami and D. Pompili. Dynamic joint processing: Achieving high spectral efficiency in uplink 5g cellular networks. *Computer Networks*, 126:44–56, 2017.
- [7] A. Hajisami and D. Pompili. DJP: dynamic joint processing for interference cancellation in cloud radio access networks. *IEEE Vehicular Technology Conference (VTC Fall)*, pages 1–5, 2015.
- [8] A. Hajisami and D. Pompili. Joint virtual edge-clustering and spectrum allocation scheme for uplink interference mitigation in c-ran. *Ad Hoc Networks*, 2018.
- [9] A. Hajisami and D. Pompili. Cloud-CFFR: coordinated fractional frequency reuse in cloud radio access network (C-RAN). *IEEE International Conference on Mobile Ad Hoc and Sensor Systems (MASS)*, pages 46–54, 2015.
- [10] T. X. Tran, A. Hajisami, P. Pandey, and D. Pompili. Collaborative mobile edge computing in 5g networks: New paradigms, scenarios, and challenges. *IEEE Communications Magazine*, 55(4):54–61, 2017.
- [11] D. Pompili, A. Hajisami, and T. X. Tran. Elastic resource utilization framework for high capacity and energy efficiency in cloud ran. *IEEE Communications Magazine*, 54(1):26–32, 2016.
- [12] Dario Pompili, Abolfazl Hajisami, and Hariharasudhan Viswanathan. Dynamic provisioning and allocation in Cloud Radio Access Networks (C-RANs). *Ad Hoc Networks*, 30:128–143, 2015.
- [13] A. Hajisami, T. X. Tran, and D. Pompili. Elastic-net: Boosting energy efficiency and resource utilization in 5g c-rans. In *IEEE 14th International Conference on Mobile Ad Hoc and Sensor Systems (MASS)*, pages 46–54. IEEE, 2017.

- [14] A. Hajisami, T. X. Tran, and D. Pompili. Dynamic provisioning for high energy efficiency and resource utilization in cloud rans. In *IEEE 12th International Conference on Mobile Ad Hoc and Sensor Systems (MASS)*, pages 471–472. IEEE, 2015.
- [15] D. Astély, E. Dahlman, A. Furuskar, Y. Jading, M. Lindstrom, and S. Parkvall. Lte: The evolution of mobile broadband. *IEEE Communications Magazine*, 47(4):44–51, Apr. 2009.
- [16] Ziaul Hasan, Hamidreza Boostanimehr, and Vijay K Bhargava. Green cellular networks: A survey, some research issues and challenges. *IEEE Communications Surveys & Tutorials*, 13(4):524–540, 2011.
- [17] C. Li, J. Zhang, and K. Letaief. Throughput and energy efficiency analysis of small cell networks with multi-antenna base stations. *IEEE Transactions on Wireless Communications*, 13(5):2505–2517, 2013.
- [18] J. T. Louhi. Energy efficiency of modern cellular base stations. *International Telecommunications Energy Conference (INTELEC)*, pages 475–476, 2007.
- [19] J. Kim, J. Cha, I. Kim, S. Y. Noh, C. S. Park, and B. Kim. Advanced design methods of doherty amplifier for wide bandwidth, high efficiency base station power amplifiers. *European Microwave Conference*, 2:4–7, 2005.
- [20] China Mobile Research Institute. C-RAN: The Road Towards Green RAN. In *C-RAN International Workshop*, October 2011.
- [21] C. Liu, K. Sundaresan, M. Jiang, S. Rangarajan, and G. K. Chang. The case for re-configurable backhaul in cloud-RAN based small cell networks. *Proc. of IEEE Intl. Conf. on Computer Communications (INFOCOM)*, pages 1124–1132, 2013.
- [22] J. Tang, W. P. Tay, and T. Q. S. Quek. Cross-layer resource allocation with elastic service scaling in cloud radio access network. *IEEE Transactions on Wireless Communications*, 48(9):5068–5081, 2015.
- [23] Z.B. Zhu, P. Gupta, Q. Wang, S. Kalyanaraman, Y. Lin, H. Franke, and S. Sarangi. Virtual Base Station Pool: Towards a Wireless Network Cloud for Radio Access Networks. In *Proc. of the ACM Intl. Conf. on Computing Frontiers (CF)*, May 2011.
- [24] Yuanming Shi, Jun Zhang, and K Letaief. Group sparse beamforming for green cloud-ran. *IEEE Transactions on Wireless Communications*, 2014.
- [25] M. Yousefvand, M. Hajimirsadeghi, and N. B. Mandayam. Impact of end-user behavior on user/network association in hetnets. In *IEEE International Conference on Communications (ICC)*. IEEE, 2018.
- [26] Sourjya Bhaumik, Shoban Preeth Chandrabose, Manjunath Kashyap Jataprolu, Gautam Kumar, Anand Muralidhar, Paul Polakos, Vikram Srinivasan, and Thomas Woo. Cloudiq: a framework for processing base stations in a data center. In *Proceedings of the 18th annual international conference on Mobile computing and networking*, pages 125–136. ACM, 2012.
- [27] K. Sundaresan, M. Y. Arslan, S. Singh, S. Rangarajan, and S. V. Krishnamurthy. Fluidnet: a flexible cloud-based radio access network for small cells. In *Proceedings of the 19th annual international conference on Mobile computing & networking*, pages 99–110. ACM, 2013.

- [28] V. N. Ha, L. B. Le, and N. Dao. Energy-efficient coordinated transmission for cloud-rans: Algorithm design and trade-off. *48th Annual Conference on Information Sciences and Systems (CISS)*, pages 1–6, 2014.
- [29] P. Patil and W. Yu. Hybrid compression and message-sharing strategy for the downlink cloud radio-access network. *Information Theory and Applications Workshop (ITA)*, pages 1–6, 2014.
- [30] B. Dai and W. Yu. Sparse beamforming and user-centric clustering for downlink cloud radio access network. *IEEE Access*, 2:1326–1339, 2014.
- [31] M. Hajimirsadeghi, G. Sridharan, W. Saad, and N. B. Mandayam. Inter-network dynamic spectrum allocation via a colonel blotto game. In *IEEE Conference on Information Science and Systems (CISS)*, pages 252–257, 2016.
- [32] M. Hajimirsadeghi, , and N. B. Mandayam. A dynamic colonel blotto game model for spectrum sharing in wireless networks. In *54th Annual Allerton Conference on Communication, Control, and Computing (Allerton)*. IEEE, 2017.
- [33] M. Peng, Y. Li, J. Jiang, J. Li, and C. Wang. Heterogeneous cloud radio access networks: A new perspective for enhancing spectral and energy efficiencies. *IEEE Wireless Communications*, 21(6):126–135, 2014.
- [34] C. L. I, C. Rowell, S. Han, Z. Xu, G. Li, and Z. Pan. Toward green and soft: a 5g perspective. *IEEE Communications Magazine*, 52(2):66–73, 2014.
- [35] S. Luo, R. Zhang, and T. J. Lim. Downlink and uplink energy minimization through user association and beamforming in c-ran. *IEEE Transactions on Wireless Communications*, 14(1):494–508, 2015.
- [36] T. X. Tran and D. Pompili. Joint task offloading and resource allocation for multi-server mobile-edge computing networks. *IEEE Transactions on Vehicular Technology, under revision*, 2017.
- [37] T. X. Tran, M. Hosseini, and D. Pompili. Mobile edge computing: Recent efforts and five key research directions. *IEEE COMSOC MMTTC Commun.-Frontiers*, 2017.
- [38] T. X. Tran, P. Pandey, A. Hajisami, and D. Pompili. Collaborative multi-bitrate video caching and processing in mobile-edge computing networks. In *13th Annual Conference on Wireless On-demand Network Systems and Services (WONS)*, pages 165–172. IEEE, 2017.
- [39] T. X. Tran and D. Pompili. Adaptive Bitrate Video Caching and Processing in Mobile-Edge Computing Networks. *IEEE Transactions on Mobile Computing, under revision*, March 2018.
- [40] T. X. Tran, A. Hajisami, and D. Pompili. Cooperative hierarchical caching in 5g cloud radio access networks. *IEEE Network*, 31(4):35–41, 2017.
- [41] T. X. Tran and D. Pompili. Octopus: A cooperative hierarchical caching strategy for cloud radio access networks. In *IEEE International Conference on Mobile Ad Hoc and Sensor Systems (MASS)*, pages 154–162, 2016.
- [42] T. X. Tran, F. Kazemi, E. Karimi, and D. Pompili. Mobee: Mobility-aware energy-efficient coded caching in cloud radio access networks. In *IEEE International Conference on Mobile Ad Hoc and Sensor Systems (MASS)*, pages 461–465, 2017.

- [43] P. Pandey, M. Hajimirsadeghi, and D. Pompili. Region of feasibility of interference alignment in underwater sensor networks. *IEEE journal of oceanic Engineering*, 39(1):189–202, 2014.
- [44] S. Vakiliinia, H. Elbizae, and B. Heidarpour. Keep pets and elephants away: Dynamic process location management in 5g zoo. In *IEEE 86th Vehicular Technology Conference (VTC-Fall)*, pages 1–7. IEEE, 2017.
- [45] M. Karimzadeh Kiskani, S. Vakiliinia, and M. Cheriet. Popularity based file categorization and coded caching in 5g networks. In *IEEE 28th Annual International Symposium on Personal, Indoor, and Mobile Radio Communications (PIMRC)*, pages 1–5. IEEE, 2017.
- [46] T. X. Tran, A. Younis, and D. Pompili. Understanding the computational requirements of virtualized baseband units using a programmable cloud radio access network testbed. In *IEEE International Conference on Autonomic Computing (ICAC)*, pages 221–226, 2017.
- [47] T. X. Tran and D. Pompili. Dynamic radio cooperation for downlink cloud-rans with computing resource sharing. In *IEEE International Conference on Mobile Ad Hoc and Sensor Systems (MASS)*, pages 118–126, 2015.
- [48] T. X. Tran and D. Pompili. Dynamic radio cooperation for user-centric cloud-RAN with computing resource sharing. *IEEE Transactions on Wireless Communications*, 16(4):2379–2393, 2017.
- [49] M. Hajimirsadeghi, N. B. Mandayam, and A. Reznik. Joint caching and pricing strategies for information centric networks. In *IEEE Global Communications Conference (GLOBECOM)*, pages 1–6. IEEE, 2015.
- [50] M. Hajimirsadeghi, N. B. Mandayam, and A. Reznik. Joint caching and pricing strategies for popular content in information centric networks. *IEEE Journal on Selected Areas in Communications*, 35(3):654–667, 2017.
- [51] M. Qian, W. Hardjawana, J. Shi, and B. Vucetic. Baseband processing units virtualization for cloud radio access networks. *IEEE Wireless Communications Letters*, 4(2):189–192, 2015.
- [52] M. Peng, K. Zhang, J. Jiang, J. Wang, and W. Wang. Energy-efficient resource assignment and power allocation in heterogeneous cloud radio access networks. *IEEE Transactions on Vehicular Technology*, 64(11):5275–5287, 2015.
- [53] T. X. Tran, A. Hajisami, and D. Pompili. Quaro: A queue-aware robust coordinated transmission strategy for downlink c-rans. In *13th Annual IEEE International Conference on Sensing, Communication, and Networking (SECON)*, pages 1–9. IEEE, 2016.
- [54] A. Hyvärinen and E. Oja. Independent component analysis: Algorithms and applications. *Neural networks*, 13(4):411–430, 2000.
- [55] J. Cardoso and A. Souloumiac. Blind beamforming for non-gaussian signals. *IEE Proceedings F-Radar and Signal Processing*, 140(6):362–370, 1993.
- [56] X. Li and T. Adali. Complex independent component analysis by entropy bound minimization. *IEEE Transactions on Circuits and Systems I: Regular Papers*, 57(7):1417–1430, 2010.
- [57] E. Bingham and A. Hyvärinen. A fast fixed-point algorithm for independent component analysis of complex valued signals. *Intl. Journal of Neural Systems*, 10(01):1–8, 2000.

- [58] R.S. Varga. On diagonal dominance arguments for bounding. *Linear Algebra and its Applications*, 14(3):211–217, 1976.
- [59] T. Camp, J. Boleng, and V. Davies. A survey of mobility models for ad hoc network research. *Wireless communications and mobile computing*, 2(5):483–502, Aug. 2002.
- [60] K. Itoh, S. Watanabe, J. Shih, and T. Sato. Performance of handoff algorithm based on distance and rssi measurements. *IEEE Transactions on Vehicular Technology*, 51(6):1460–1468, Nov. 2002.
- [61] Daewon Lee, Hanbyul Seo, Bruno Clerckx, Eric Hardouin, David Mazzaresse, Satoshi Nagata, and Krishna Sayana. Coordinated multipoint transmission and reception in lte-advanced: deployment scenarios and operational challenges. *IEEE Communications Magazine*, 50(2):148–155, 2012.
- [62] M. Simko, D. Wu, Ch. Mehlführer, J. Eilert, and D. Liu. Implementation aspects of channel estimation for 3gpp lte terminals. In *European Wireless Conf. on Sustainable Wireless Technologies (European Wireless)*, pages 1–5, 2011.
- [63] A. Abavisani, M. Soleimani, and V. Tabatabavakili. A novel algorithm for blind adaptive recognition between 8-psk and $\pi/4$ -shifted qpsk modulated signals for software defined radio applications. In *4th International Conference on Cognitive Radio Oriented Wireless Networks and Communications*, pages 1–6. IEEE, 2009.
- [64] M. Yousefvand, N. Ansari, and S. Khorsandi. Maximizing network capacity of cognitive radio networks by capacity-aware spectrum allocation. *IEEE Transactions on Wireless Communications*, 14(9):5058–5067, 2015.
- [65] M. Yousefvand, S. Khorsandi, and A. Mohammadi. Interference-constraint spectrum allocation model for cognitive radio networks. In *6th IEEE International Conference Intelligent Systems (IS)*, pages 357–362. IEEE, 2012.
- [66] T. D. Novlan, R. K. Ganti, A. Ghosh, and J. G. Andrews. Analytical evaluation of fractional frequency reuse for ofdma cellular networks. *IEEE Transactions on Wireless Communications*, 10(12):4294–4305, 2011.
- [67] Naveed UL Hassan and Mohamad Assaad. Optimal fractional frequency reuse (ffr) and resource allocation in multiuser ofdma system. In *International Conference on Information and Communication Technologies (ICICT)*, pages 88–92. IEEE, 2009.
- [68] C. Wang, E. K. Au, R. D. Murch, W. H. Mow, R. S. Cheng, and V. Lau. On the performance of the mimo zero-forcing receiver in the presence of channel estimation error. *IEEE Transactions on Wireless Communications*, 6(3):805–810, 2007.
- [69] F. Héliot, M.A. Imran, and R. Tafazolli. Energy efficiency analysis of idealized coordinated multi-point communication system. In *Vehicular Technology Conference*, pages 1–5. IEEE, 2011.
- [70] A. R. Dhaini, P. H. Ho, G. Shen, and B. Shihada. Energy efficiency in tdma-based next-generation passive optical access networks. *IEEE/ACM Transactions on Networking (TON)*, 22(3):850–863, 2014.

- [71] N. Saquib, E. Hossain, and D. I. Kim. Fractional frequency reuse for interference management in lte-advanced hetnets. *IEEE Wireless Communications*, 20(2):113–122, 2013.
- [72] Wenhua Jiao, Pin Jiang, and Yuanyuan Ma. Fast handover scheme for real-time applications in mobile wimax. *IEEE International Conference on Communications (ICC)*, pages 6038–6042, 2007.
- [73] M. Assaad. Optimal fractional frequency reuse (ffr) in multicellular ofdma system. *IEEE Vehicular Technology Conference*, pages 1–5, 2008.
- [74] F. R. P. Cavalcanti. *Resource Allocation and MIMO for 4G and Beyond*. Springer, 2014.
- [75] Gunther Auer, Vito Giannini, Claude Desset, Istvan Godor, Per Skillermark, Magnus Olsson, Muhammad Ali Imran, Dario Sabella, Manuel J Gonzalez, Oliver Blume, et al. How much energy is needed to run a wireless network? *IEEE Wireless Communications*, 18(5):40–49, 2011.
- [76] A. Beloglazov, J. Abawajy, and R. Buyya. Energy-aware resource allocation heuristics for efficient management of data centers for cloud computing. *Future Generation Computer Systems*, 28(5):755–768, 2012.
- [77] O. Arnold, F. Richter, G. Fettweis, and O. Blume. Power consumption modeling of different base station types in heterogeneous cellular networks. *Future Network and Mobile Summit*, pages 1–8, 2010.
- [78] K. Lin, J. Xu, I. M. Baytas, S. Ji, and J. Zhou. Multi-task feature interaction learning. In *22nd ACM SIGKDD International Conference on Knowledge Discovery and Data Mining*, pages 1735–1744. ACM, 2016.
- [79] H. S. Dhillon, R. K. Ganti, F. Baccelli, and J. G. Andrews. Modeling and analysis of k-tier downlink heterogeneous cellular networks. *IEEE Journal on Selected Areas in Communications*, 30(3):550–560, 2012.
- [80] J. G. Andrews, F. Baccelli, and R. K. Ganti. A tractable approach to coverage and rate in cellular networks. *IEEE Transactions on Communications*, 59(11):3122–3134, 2011.
- [81] EURECOM. Open air interface. Available: <http://www.openairinterface.org/>, October 2014.
- [82] I. Alyafawi, E. Schiller, T. Braun, D. Dimitrova, A. Gomes, and N. Nikaen. Critical issues of centralized and cloudified lte-fdd radio access networks. *IEEE International Conference on Communications (ICC)*, pages 5523–5528, 2015.
- [83] E. Dahlman, S. Parkvall, and J. Skold. *4G: LTE/LTE-advanced for mobile broadband*. Academic press, 2013.
- [84] K. S. Trivedi, R. A. Wagner, and T. M. Sigmon. Optimal selection of cpu speed, device capacities, and file assignments. *Journal of the ACM (JACM)*, 27(3):457–473, 1980.
- [85] P. Chanclou, A. Pizzinat, F. Le Clech, T. Reedeker, Y. Lagadec, F. Saliou, B. Le Guyader, L. Guillo, Q. Deniel, and S. Gosselin. Optical fiber solution for mobile fronthaul to achieve cloud radio access network. In *Future Network and Mobile Summit*, pages 1–11. IEEE, 2013.